Kinetic Monte-Carlo Modelling of Charge and Exciton Dynamics in Phosphorescent Organic Light-Emitting Diodes

Thesis submitted by

Stephen Sanderson BEng(Hons) BSc

in April 2021

for the degree of Doctor of Philosophy

in the College of Science & Engineering

James Cook University

JAMES COOK UNIVERSITY

AUSTRALIA

Statement of Contribution of Others

I gratefully acknowledge the contributions detailed below:

Funding support was provided by an Australian Government Research Training Program scholarship.

Editorial assistance was provided for the overall thesis by Prof. Ronald White and Dr. Bronson Philippa of James Cook University. Chapters 4 & 5 are based on published journal articles, and Chapter 6 is based on a submitted journal article, and editorial assistance for these chapters was provided by the listed co-authors.

Contributions to co-authored publications that form the basis of Chapters 4-6 are as follows. In all cases, I performed the simulations, analysed the results, prepared the figures, and wrote the text. In the case of Chapter 6, the molecular dynamics simulations were performed using code adapted from source files provided by Prof. Alan Mark *et al.* from the University of Queensland.

Contributions to algorithms as described in Chapter 3 are as follows. I wrote the simulation and analysis code, and implemented the algorithms described, with some advice on algorithm details provided by Dr. Bronson Philippa and Prof. Ronald White. The derivation of the analytical solution for the blocking benchmark was originally performed by Dr. Bronson Philippa. The strategies employed in Chapter 7 for faster solution deposition simulations of thicker films were originally conceived by Prof. Alan Mark, and were developed and implemented by me.

Abstract

Organic light-emitting diodes (OLEDs) are a key component of modern electronics, and have been successfully commercialised in a number of fields. However, there is still room for improvement in the efficiency of both the device itself, and the manufacturing process, and these improvements can only be made with a clear picture of the underlying physics. In this work, computer modelling techniques are employed to gain insights into OLED operation by simulating charge transport and exciton dynamics. In particular, a kinetic Monte-Carlo (KMC) transport model is developed, and this is coupled with molecular dynamics deposition modelling for accurate morphology representation. These techniques are applied to investigate charge and exciton dynamics in phosphorescent OLEDs, in which an emissive guest is blended with a host.

The effects of the guest:host blend ratio on charge transport were examined, and it was found that due to charge trapping on the guest, charge transport is predominantly guest-based, meaning that excitons also tend to form within close proximity of guest molecules. Additionally, we reveal that this guest-based transport leads to a minimum mobility at relatively low guest concentrations, as closely packed clusters of guest molecules tend to act as a single macro-trap, rather than individual trapping sites. This highlights the important effects of guest aggregation on the efficiency of charge transport.

We next examine the effects on charge transport due to differences in energy level alignment between the guest and host. It is shown that small changes in energy level alignment can have significant effects on the mobility balance. In the case of a faster and slower carrier, it is shown that the mobility at the balance point is primarily dictated by that of the slower carrier.

To understand the role of exciton dynamics, we again analyse the effects of the guest:host blend ratio in combination with various exciton densities to gain a detailed picture of the relative loss processes. We pay particular attention to concentration quenching of triplet excitons induced by guest-guest intermolecular interactions, a process independent of the triplet density that has not previously been considered in KMC models. In addition, we analyse the differences in results due to how morphology is considered in the KMC model. We compare between results using the simple approximation of molecular sites aligned to the nodes of a cubic lattice, and those obtained using morphology that was generated by simulating the vacuum deposition process in atomic detail with molecular dynamics techniques. We find that for guest-based processes at low guest concentrations where aggregation of the guest is limited, the cubic lattice approximation is in surprisingly good agreement with the more realistic morphology. However, some differences are observed between host-based processes due to the differences in packing structure that are not captured by the cubic lattice.

Finally, a method was developed for more efficient simulation of the solution deposition process in the presence of substrate and vacuum interfaces while maintaining atomic detail, in order to increase the feasible layer thickness. Using this technique for morphology generation, KMC simulations were performed to compare vacuum- and solution-deposited films. Our results suggested that despite some differences in host

orientation in the as-deposited films leading to minor differences in mobility, overall device operation in layers that have not degraded is relatively insensitive to the deposition technique for the blend studied (within the limits of the KMC model). Furthermore, only small differences in transport properties were observed for experimentally realistic levels of trapped solvent. It was therefore proposed that a plausible explanation of the experimentally observed faster degradation in the solution-deposited film is that it is a direct result of the differences in molecular packing, rather than a secondary effect caused by differences in charge transport or exciton dynamics.

Acknowledgements

I would like to thank my supervisors, Prof. Ron White, Dr. Bronson Philippa, Prof. Paul Burn, and Prof. Alan Mark for their invaluable advice, support and encouragement throughout the course of this project – it certainly would not have been possible without them. I'd also like to thank Dr. George Vamvounis for the insight he provided into the experimentalist's perspective and relevant real-world considerations. Finally, I'd like to thank Dr. Thomas Lee, Dr. Martin Stroet, and Audrey Sanzogni for their assistance in configuring and debugging molecular dynamics simulations, as well as A/Prof. David Huang for his insights into quantum chemistry, and Dr. Paul Shaw for his elucidating comments regarding exciton dynamics.

List of Publications

This thesis contains content that was published in the following journal articles:

[1] Stephen Sanderson, Bronson Philippa, George Vamvounis, Paul L. Burn, and Ronald D. White. Understanding charge transport in Ir(ppy)3:CBP OLED films. *The Journal of Chemical Physics*, **150**, 094110 (2019). doi:10.1063/1.5083639

[2] Stephen Sanderson, Bronson Philippa, George Vamvounis, Paul L. Burn, and Ronald D. White. Elucidating the effects of guest-host energy level alignment on charge transport in phosphorescent OLEDs. *Applied Physics Letters*, **115**, 263301 (2019). doi:10.1063/1.5131680

[3] Siddhartha Saggar, Stephen Sanderson, Desta Gedefaw, Xun Pan, Bronson Philippa, Mats R. Andersson, Shih-Chun Lo, and Ebinazar B. Namdas. Toward Faster Organic Photodiodes: Tuning of Blend Composition Ratio. *Advanced Functional Materials*, 2010661 (2021). doi:10.1002/adfm.202010661

In addition, the following article has been accepted for publication, but is not yet published at the time of writing:

[4] Stephen Sanderson, George Vamvounis, Alan E. Mark, Paul L. Burn, Ronald D. White, and Bronson Philippa. Unraveling Exciton Processes in Ir(ppy)3:CBP OLED Films Upon Photoexcitation. *The Journal of Chemical Physics*, 164101 (2021). doi:10.1063/5.0044177

Contents

List of Figures

1 Introduction

Semiconductors are a core element of modern electronics, enabling complex logic, solid state lighting, solar energy production, digital photography, and many more possibilities. Traditional semiconductors are made from inorganic materials such as silicon, and have provided increasingly high-performing devices as manufacturing technologies are improved. However, an alternative that is seeing increased adoption in many areas is that of organic semiconductors.

Organic semiconductors are semiconductors built from organic, carbon-based molecules. While they tend to have less raw performance than their inorganic counterparts, organic semiconductors can be manufactured cheaply and efficiently through techniques such as ink-jet printing [5, 6], and their freedom in chemical tunability allows for optimisation towards desirable application-specific properties [7–9]. This has lead to their adoption in a number of commercial products [10–12]. Organic light-emitting diodes are particularly successful, and have become increasingly popular for use in displays due to their energy efficiency and high contrast, as well as their ability to mechanically deform and allow for flexible screens.

However, despite their successful commercialisation, opportunity still exists for improvement in organic light-emitting diodes, and in organic semiconductors in general [13]. In particular, their poor performance when compared to inorganic semiconductors can be attributed in part to their charge transport characteristics. While silicon semiconductors can be highly conductive due to their crystallinity, the disordered nature of most organic semiconductor materials leads to charge trapping, which inhibits the achievement of comparable conductivity [14]. Furthermore, while solution deposition techniques for organic semiconductors (such as ink-jet printing) can be highly cost effective, they tend to produce devices with lower performance when compared to

those manufactured with more expensive processes such as vacuum deposition [15–17]. A thorough understanding of charge transport in organic devices, and how it is affected by morphology (the way in which molecules are arranged), is therefore crucial to improving performance. This represents the fundamental goal of this work.

This thesis aims to gain insight into organic semiconductor transport using computational modelling techniques. In particular, a kinetic Monte-Carlo model is developed to analyse charge transport and exciton dynamics, and how they are affected by various system properties, with a focus on organic light-emitting diodes. These properties include the effects of morphology, and to that end, molecular dynamics simulations are employed to simulate the vacuum and solution deposition processes in atomic detail.

This document is structured as follows. Chapter 2 presents a literature review, with a focus on organic light-emitting diodes, their performance characteristics, and relevant modeling techniques. Chapter 3 provides a detailed overview of the kinetic Monte-Carlo framework developed in this work, and the computational techniques used to implement and optimise it. Chapter 4 applies the model to a high performing guest-host emissive layer blend commonly used in organic light-emitting diodes to gain insight into how charge trapping on emissive guest molecules affects the overall charge transport characteristics. Further to this, Chapter 5 investigates a similar, prototypical device in which the electron and hole trapping depths are varied to determine how this parameter can be used to optimise device performance. Chapter 6 introduces excitons (bound electron-hole pairs capable of light emission) to the model, and investigates how the concentration of the emissive guest molecules, as well as the density of excitons, affects device efficiency. It also provides a comparison of results between realistic morphology generated with molecular dynamics simulations and the common simplifying approximation of cubic lattice morphology. Chapter 7 further utilises molecular dynamics for morphology generation, and combines the charge and exciton transport modelling techniques from the previous chapters in order to simulate full device operation and compare charge and exciton dynamics in devices with vacuum- and solution-deposited morphologies. Finally, Chapter 8 provides concluding remarks, and makes recommendations for future work.

2 Organic Semiconductors

The following chapter presents a literature review. It begins with an overview of charge and exciton dynamics in organic semiconductors, with a focus on organic light-emitting diodes. Transport modelling techniques are then discussed with emphasis on the techniques that were utilised in this work, as well as relevant optimisation methods. Finally, a brief introduction to the modelling of structures within organic semiconductors is provided with a focus on classical atomistic molecular dynamics.

2.1 Fundamentals of OLEDs

Light-emitting diodes (LEDs) are a core semiconductor technology that has become ubiquitous in everyday life. While original LEDs made use of inorganic silicon-based semiconductors, in 1987 Tang and van Slyke reported the first practical organic LED (OLED) which instead used electroluminescent carbon-based molecules [18]. Since then, OLEDs have seen significant development, and have been successfully commercialised in applications such as displays and solid state lighting [10–12]. Indeed, modern OLEDs provide a number of advantages over their inorganic counterparts, including colour tunability, mechanical flexibility, and cheap, energy efficient manufacturing [7–9]. While liquid crystal displays (LCDs), the main competitor to OLEDs, typically rely on a backlight with a thin film in front responsible for pixel colour, OLED displays are able to make use of individual OLEDs for each pixel, enabling them to be switched independently. This allows them to offer darker blacks, better contrast, faster response times, better power efficiency, and cheaper manufacturing compared to LCDs [12, 19, 20].

The following sections provide details of the physics behind OLEDs, along with an outline of relevant manufacturing processes and performance metrics.

2.1.1 Manufacturing Techniques

To fabricate OLEDs, there are two methods that are commonly employed; vacuum deposition, and solution deposition. Vacuum deposition is the standard process for small molecule-based OLEDs [11, 15]. It involves evaporating layers of material onto a substrate under vacuum, and utilises masks to separate sections of the device (individual pixels, for example). It can therefore give fine-grained control over device structure, and is capable of producing high quality devices [15]. However, the maximum possible device size is somewhat limited for this process, making it difficult to produce large-area displays [11, 15]. The process is also more complex than solution deposition, and produces relatively low yields, making it the more expensive of the two options [11].

Solution deposition can be performed through a number of processes including ink-jet printing, spin-coating, and blade-coating, but essentially involves depositing layers of semiconductor material dissolved in solution, which are then able to dry in place [11, 17]. These processes are capable of producing large area displays with high resolution, and allow for cheap, scalable manufacturing [15, 21]. However, solution deposition inherently requires that the deposited molecules are soluble, and this consequently introduces some limitations. While polymer-based OLEDs are easily produced through solution deposition, their efficiency and lifetime do not compare favourably with small molecule OLEDs [15, 17]. On the other hand, films of small molecules deposited via solution deposition tend to be of poorer quality compared to their vacuum deposited counterparts [15–17]. Understanding and improving upon the limitations of solution deposition therefore presents a promising route to realising more efficient production of OLEDs, and we will return to this topic in Chapter 7.

2.1.2 Charge Transport

Semiconductors are materials which have an electrical conductivity between that of a conductor and that of an insulator. Traditional inorganic semiconductors are typically crystalline in nature, and charge transport is described in terms of conduction and valence bands [22]. Electron and hole wavefunctions are delocalised in these devices, and operation is typically modelled based on scattering caused by impurities [22]. On the other hand, the disordered nature of most organic semiconductor materials leads to localised wavefunctions, and charge transport is better described as thermally activated hops between discrete electronic states [23,24]. These discrete states typically correspond to the charged states of small molecules or polymer fragments, and hence instead of conduction and valence bands, charge transport in organic semiconductors is discussed in terms of a molecule's electron affinity (EA) and ionisation potential (IP). These quantities are related to (but not necessarily equal to) the lowest unoccupied molecular orbital (LUMO) and highest occupied molecular orbital (HOMO) of the neutral molecule [24, 25].

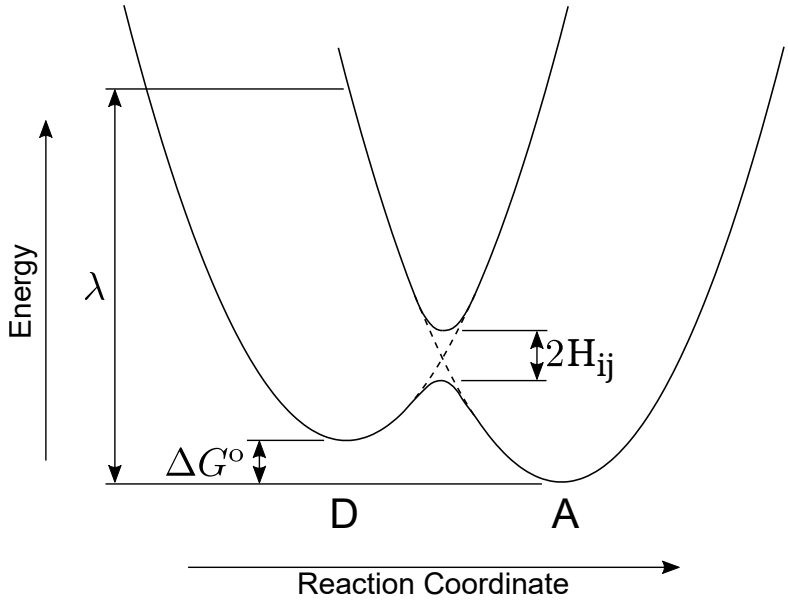

Figure 2.1: Adiabatic (solid lines) and diabatic (dashed lines) potential energy surfaces for a transfer between a donor state (D) and an acceptor state (A), corresponding to localised electronic states on neighbouring molecules.

More precisely, charge hopping in organic semiconductors from a donor state, A, to an acceptor state, B, can be described as a transition between local minima along the adiabatic potential energy surface [24, 26–28], as shown in Figure 2.1. In this figure, the transition is described by three variables. Firstly, the difference in the Gibbs free energy of the localised states, ΔG^{o}, accounts for factors such as the local electric field, variance in the EA or IP, and changes in entropy (although entropy is often neglected for simplicity [29]). The reorganisation energy, λ, is the energy required to reorganise the system into its final state without the charge transfer actually occurring. This quantity is comprised of two components; the inner-sphere reorganisation energy which accounts for deformation of the donor and acceptor molecules, and the outer-sphere reorganisation energy which accounts for changes in the surrounding environment [30, 31]. Finally, the electronic coupling, H_{ij}, accounts for overlap in the donor and acceptor electronic wavefunctions, and is equivalent to the off-diagonal term of the Hamiltonian that describes the system. The combination of a charge and its related deformation to the environment is known as a polaron, and so charge transport in organic semiconductors is often discussed in terms of polaron transport [31].

Under this description, it can clearly be seen that the disordered nature of molecular packing in organic semiconductors can lead to significant degrees of both energetic and spatial disorder of the localised electronic states [23, 32]. This disorder results in so-called trap states, which are states that are difficult for a polaron to hop away from. Charges prefer to occupy lower energy states, and so trap states typically have a Gibbs free energy that is relatively low compared to the surrounding accessible states. Escaping a trap often requires additional thermal energy, and so unlike inorganic semiconductors which perform better at lower temperatures, organic semiconductors generally show increased mobility as temperature increases, at least until the elevated

temperature causes other undesirable side-effects [33]. The disordered nature of organic semiconductors resulting in trap states is a major contributing factor to their relatively poor charge transport characteristics when compared to their inorganic counterparts [14].

2.1.3 Excitons

Excitons are bound electron-hole pairs, and are a key component in the operation of many semiconducting devices. They can be formed either through photoexcitation, or an electron and hole meeting within a device [34]. The former process is used in photovoltaic cells, in which incident photons excite a neutral molecule or monomer, and the resultant excitons are separated into free charges that are then extracted at the electrodes to produce current. In contrast, LEDs use injected charges to form excitons which are able to radiatively decay to the ground state, thus emitting a photon.

In silicon semiconductors, delocalised electronic states combined with high dielectric permittivity lead to highly delocalised excitons, known as Wannier-Mott excitons [35]. On the other hand, organic semiconductors tend to have a relatively low dielectric permittivity, leading to localised, Frenkel excitons that are much more tightly bound than their delocalised counterparts [35,36]. This tight Coulombic binding makes dissociation of excitons into free charges (necessary for the function of photovoltaic devices) difficult under an electric field alone, and thus a number of strategies have been developed to overcome this limitation, such as the introduction of molecular interfaces, and chemical tuning to increase the dielectric permittivity [37–39]. On the other hand, Frenkel excitons are less likely to interact with each other compared to Wannier-Mott excitons at the same concentration. This can be beneficial to device performance, since exciton interactions typically result in at least one of the excitons being quenched, thus returning the excited molecular fragment to the neutral ground state. As this thesis focuses on organic semiconductors, we will henceforth only consider Frenkel excitons, and will refer to them simply as excitons.

As excitons consist of two spin-$\frac{1}{2}$ particles, there are four possible exciton spin states. As outlined below, one of these states is the spin-0 singlet state, while the other three are triplet states with some net spin [40].

$$\text{Singlet: } |{\downarrow\Uparrow}\rangle - |{\uparrow\Downarrow}\rangle$$

$$\text{Triplet: } \begin{cases} |{\uparrow\Uparrow}\rangle \\ |{\downarrow\Uparrow}\rangle + |{\uparrow\Downarrow}\rangle \\ |{\downarrow\Downarrow}\rangle \end{cases}$$

Since photons are spin-neutral, and spin is a conserved quantity, in general only singlet excitons are formed through photoexcitation, and only a singlet exciton can emit a photon [34]. On the other hand, excitons formed from free charges typically have a 25% chance of being a singlet, or a 75% chance of being a triplet based on spin statistics

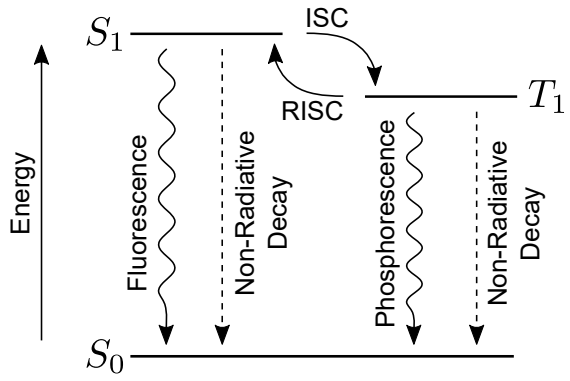

Figure 2.2: Jablonski diagram of exciton state transitions. ISC and RISC are intersystem crossing and reverse intersystem crossing respectively, in which an exciton crosses from one spin state to the other. Note the omission of higher energy singlet and triplet states, which tend to be short-lived and quickly relax to either the ground state (S_0) or the first excited state (S_1 or T_1).

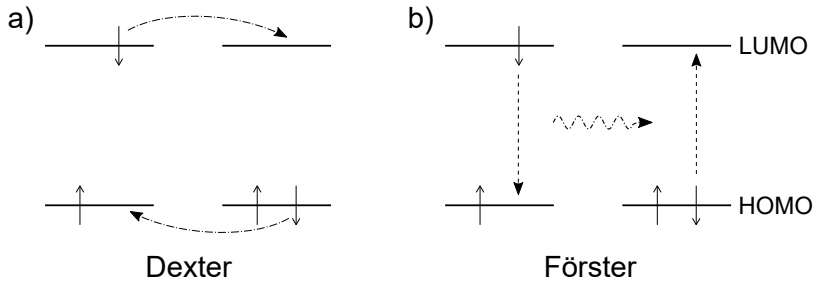

Figure 2.3: Illustration of (a) Dexter transfer and (b) Förster transfer.

[34]. An important exception, however, is the case of molecules with strong spin-orbit coupling. Spin-orbit coupling is a relativistic interaction between a particle's spin and its motion within the molecular orbital, and therefore strong spin-orbit coupling enables intersystem crossing (ISC), in which an exciton crosses from the singlet to the triplet state through an exchange of spin [34, 41, 42]. Strong spin-orbit coupling additionally allows for both photoexcitation and radiative decay of triplet excitons, and can be achieved through the inclusion of heavy metal atoms such as iridium or platinum in a molecule [41], a strategy that is commonly used in modern phosphorescent OLEDs [12]. Alternatively, when the singlet and triplet energies are close, triplets can undergo reverse intersystem crossing (RISC) in which they transition to the singlet state via thermal activation, without the need for strong spin-orbit coupling, and this strategy is also commonly used to produce thermally activated delayed fluorescence (TADF) OLEDs [42–46]. A summary of possible exciton state transitions is shown in Figure 2.2.

Once formed, excitons are able to diffuse via two different mechanisms, as illustrated in Figure 2.3. The first is the Dexter exchange mechanism, in which electrons are exchanged between neighbouring molecular sites, so that the exciton moves from one site to the other [34, 47]. As this process involves a direct exchange of particles, spin is conserved, and so it is accessible to both singlet and triplet excitons. The other

diffusion process available to excitons is Förster resonant energy transfer (FRET), in which dipole-dipole coupling between two molecules enables a non-radiative transfer of energy [34, 48, 49]. The transfer rate is dependent on the transition dipole alignment, and the overlap between the emission and absorption spectra of the source and destination molecules [34, 48]. This process is typically only efficient for singlets, as the energy transferred has no net spin [50]. However, strong spin-orbit coupling can overcome this limitation and enable efficient FRET of triplets [51].

Through the course of device operation, interactions can occur between excitons and other nearby excitons or polarons. These interactions are spin-dependent, and can be described in simplified form as [52–56]

$$\begin{aligned} &\text{Singlet-Singlet Annihilation:} && S_1 + S_1 \rightarrow S_0 + S_1, \\ &\text{Singlet-Triplet Annihilation:} && S_1 + T_1 \rightarrow S_0 + T_1, \\ &\text{Triplet-Triplet Annihilation:} && T_1 + T_1 \rightarrow S_0 + \eta T_1 + (1-\eta) S_1, \\ &\text{Exciton-Polaron Quenching:} && p + E_1 \rightarrow p + S_0, \end{aligned} \tag{2.1}$$

where S_1 and T_1 are the first singlet and triplet excited states, S_0 is the ground state, p is a polaron, E_1 is either a singlet or triplet exciton, and η is the probability that triplet-triplet annihilation results in a triplet. As these interactions all result in exciton loss, minimising their probability is essential for high performing OLEDs, as well as other electronic devices such as solar cells and photodetectors.

2.1.4 OLED Performance and Device Structure

While original OLEDs used a simple monolayer or bilayer structure [18, 57], the vast majority of modern OLEDs utilise a number of stacked layers in order to increase efficiency [46, 57–60]. An example of this is shown in Figure 2.4. The electron and hole transport layers serve the purpose of delivering charges to the emissive layer (also known as the active layer), as well as inhibiting opposite charges from leaving the emissive layer. Ideal transport layers also act as exciton blocking layers, ensuring that excitons are confined to the active layer where they are able to emit light. Additionally, good transport layers allow for efficient charge injection from the electrodes to increase efficiency, or alternatively, separate injection layers are sometimes used between the electrode and the transport layer [57].

To quantify the benefits of strategies such as layering and chemical tuning, OLED performance can be characterised in a number of ways. While properties such as colour, lifetime, and current-voltage characteristics are important for practical devices, this thesis focuses on modelling properties of the emissive layer, rather than entire devices, and therefore we will primarily consider quantum efficiency and charge mobility. Quantum efficiency in OLEDs can be characterised in terms of the internal quantum efficiency (IQE) or external quantum efficiency (EQE). IQE is defined as the percentage of injected electron-hole pairs that are able to produce a photon [12, 43, 61]. Similarly, EQE is defined as the percentage of injected charge pairs able to produce

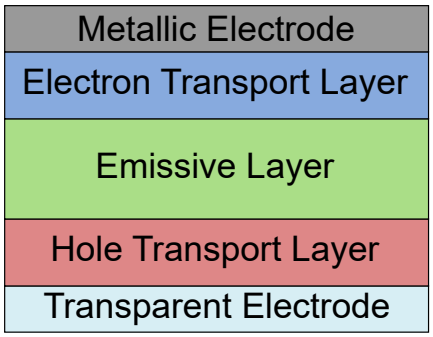

Figure 2.4: Example OLED layer stack.

a photon that is emitted from the device, thereby differing from the IQE by an out-coupling factor which accounts for optical properties of the device and the direction of light emission [12, 43, 61, 62].

Light emission in OLEDs can be classed as fluorescent (singlet emission) or phosphorescent (triplet emission) [34,63]. The first practical OLEDs made use of fluorescent emission at the interface between a hole transporting layer and an electron transporting layer [18]. However, these simple fluorescent devices were naturally limited to an IQE of 25% due to exciton spin statistics yielding a 1:3 singlet to triplet ratio. To overcome this limit, phosphorescent and thermally activated delayed fluorescence devices were developed, which both have a theoretical IQE of 100% [61,64]. In TADF OLEDs, emitters are designed to have a small energy difference between the S_1 and T_1 exciton states, thus allowing thermally activated RISC from the triplet state to the singlet state, and therefore the potential for 100% fluorescent emission [42, 64]. Similarly, phosphorescent OLEDs make use of molecules with strong spin-orbit coupling to convert singlet excitons to the triplet state and allow for triplet emission [34]. In both cases, efficiency at high currents (and therefore the achievement of high brightness) is limited by exciton-exciton quenching [7]. A strategy to counteracted this is through the use of a guest-host blend as the emissive layer, in which the emissive guest is blended with a host that has exciton energy levels higher than that of the guest, so that excitons are effectively contained on the guest and their diffusion is limited [63]. However, some questions remain about the details of exciton dynamics in such a system, which we will address further in Chapter 6.

This exciton confinement strategy is commonly used in phosphorescent OLEDs, and is often also employed for TADF OLEDs, although recent work has shown that high efficiency can also be achieved with an emissive layer composed purely of the TADF emitter [46]. A potential advantage of TADF is that it provides a relatively inexpensive alternative to phosphorescent OLEDs by eliminating the requirement of rare metals [45]. However, it remains a challenge to produce high performance TADF-based OLEDs from solution-processable materials [45], which are of interest for coating large areas for applications such as lighting. Hence, in this thesis, we focus on guest-host phosphorescent OLEDs.

In a high-performing guest-host blend, electron and hole mobilities are ideally balanced to give a broad recombination zone, and thereby avoid areas of high exciton density where exciton-exciton quenching would be more likely [8, 43, 63, 65–67]. However, guest emitters tend to also act as charge traps, and even small guest concentrations can have a large effect on charge transport [68, 69]. Hence, the morphology of the emissive blend is of crucial importance for achieving high efficiency devices with good charge transport characteristics, as is the relative difference in EA and IP between the guest and host, and we will explore these concepts further in Chapters 4 and 5 in the context of phosphorescent OLEDs.

2.2 Computational Modelling

Computational modelling plays a key role in understanding the underlying physics of OLEDs and organic semiconductors in general, particularly when it comes to properties that are difficult to observe experimentally [70–72]. It can be used on various length scales, from calculations of molecule properties, to modelling molecular geometry, to simulating the operation of an entire device, and provides a way to efficiently reduce the parameter space of optimal device characteristics [70, 73–76]. However, larger scale modelling is inherently more computationally demanding, and therefore broader approximations must be made to maintain feasibility. The following sections provide a brief overview of modelling techniques for device structure, along with an in depth review of transport modelling, focusing in particular on the kinetic Monte-Carlo (KMC) technique.

2.2.1 Transport

When modelling charge transport in organic semiconductors, there are two common approaches. The first is the drift-diffusion model, in which differential equations are solved for the device current. For example, the electron current in a 1D device can be represented by [76]

$$J_n = -q\mu n E + \mu k_{\mathrm{B}} T \frac{dn}{dx}, \tag{2.2}$$

where J_n is the electron current density, q is the unit charge, n is the charge number density as a function of the position (x), μ is the mobility, E is the electric field, k_{B} is Boltzmann's constant, and T is the temperature. Note that the electric field here includes the contribution of Coulomb interactions, and is therefore a function of both space and time. This method treats charges in an averaged manner, and therefore interactions are included as concentration-dependent rates rather than being treated explicitly [76]. This allows for very efficient modelling of device-scale systems, but typically requires a large number of input parameters that must be either measured via experiment, or simulated with other more detailed methods [77].

The other commonly used method for simulating charge transport is kinetic Monte-Carlo modelling, which has the advantage of enabling investigation of the relation

between transport events and explicit morphology [32, 78–81]. KMC models consider charges and excitons explicitly, and simulate their motion and interactions based on random walks in order to solve the master equation governing their behaviour [23, 32, 77]. At a given snapshot in time, a rate is assigned for every possible event, including hops between localised states, interactions with nearby particles, and exciton decay events. From N total possible events, a single event, n, is then chosen based on a random number, such that

$$\sum_{i=0}^{n-1} \nu_i \leq \xi_1 \sum_{i=0}^{N-1} \nu_i < \sum_{i=0}^{n} \nu_i, \tag{2.3}$$

where ν_i is the rate associated with event i, and ξ_1 is a uniform random number on the interval $(0, 1]$ [23, 82]. Note the use of 0-based indexing for the sake of clearer algorithm explanations in later sections. The simulation time is then advanced by a random interval

$$\Delta t = \frac{-\ln(\xi_2)}{\sum_{i=0}^{N-1} \nu_i}, \tag{2.4}$$

where ξ_2 is a separate uniform random number on the same interval [23, 82]. While this method can theoretically capture interesting aspects of the system in great detail, for example by using quantum chemical calculations to evaluate event rates with high accuracy at each step, it is limited practically by the processing power available, and the level of detail offered by a full quantum mechanical treatment is only currently feasible in small systems [32, 83]. As such, event rates are typically only calculated within a short range, so that statistically improbable events are excluded [83–85]. Additionally, rather than updating rates after every Monte-Carlo (MC) move using expensive quantum chemical calculations, classical approximations are commonly used instead, such as the Miller-Abrahams [23, 86] and Marcus [26, 86] formalisms, which we will discuss further in Chapter 3. Even with classical rate calculations, however, KMC modelling becomes extremely computationally expensive for large systems, and so it is typically limited to the microscopic to mesoscopic scale [24, 84]. Importantly though, it provides a key link in multi-scale modelling pipelines, enabling the possibility of *ab initio* simulations of device properties [24, 73, 87, 88]. These simulations begin by calculating molecular structures and interaction parameters using quantum-chemical techniques such as density functional theory. Those parameters can then be used in molecular dynamics simulations to obtain realistic device morphology, at which point (typically under the assumption that charge transport is significantly faster than molecular motion) further calculations can provide site energies and coupling parameters required for KMC rate calculations. Finally, bulk system properties obtained via KMC modelling of small-scale systems can be used as input to drift-diffusion models, allowing simulation and prediction of full-scale device properties.

Even without *ab initio* parameter calculation, detailed KMC simulations informed by experimental results can be performed that are able to capture properties and rela-

tionships which are otherwise difficult to observe. For example, Heiber *et al.* recently used KMC modelling to capture the time dependence of charge mobility in organic photodetectors, showing that it is strongly influenced by morphology, especially under high electric fields where charges can become trapped in "dead end" pathways [89]. As we wish to explore the influence of morphology on various device properties, capture of structure-property relationships such as this is crucial, and so the kinetic Monte-Carlo approach was used in this work. The following sections present an overview of recent and notable KMC results, and a review of common optimisation techniques.

Notable Kinetic Monte-Carlo Results

Kinetic Monte-Carlo modelling was first used to investigate organic semiconductor charge transport by H. Bässler in 1993 [23]. This model showed the relationship between charge mobility and positional and energetic disorder of the hopping sites, as well as how high degrees of energetic disorder lead to dispersive charge transport. Bässler also pioneered the use of the Gaussian disorder model (GDM) in KMC simulations for assigning site energies, in which the energy of each site is randomly chosen from a Gaussian distribution with standard deviation σ, and this method is still commonly used in recent work [32]. It was further shown that in the absence of an electric field, a charge initially randomly placed within the energetic density of states will relax, on average, to an energy of $\frac{\sigma^2}{k_\mathrm{B}T}$ below the mean energy (typically the EA or IP) [23].

Soon after, in 1998, Novikov *et al.* introduced the correlated disorder model (CDM), in which site energies were spatially correlated, rather than being uncorrelated in space as in the GDM [90]. Randomly oriented dipoles were placed on each molecular site, and the electrostatic interactions between the dipoles were used to calculate site energies [90]. This produced an energy distribution that was Gaussian in nature, but with some degree of spatial correlation, and resulted in a simulated field-dependent mobility following the Poole-Frenkel form [91] ($\mu \propto \exp\left(\gamma\sqrt{E}\right)$, where γ is a constant) over a wider range of electric fields than had been previously observed under the GDM. However, despite its success, the CDM has not been found to be universally applicable, particularly to small molecule organic semiconductors. While it produces better results than the GDM for some molecules, others have been shown to better agree with the Gaussian disorder model [92]. More recently, quantum chemical calculations have been employed to explicitly calculate site energies in a parameter-free manner, resulting in good experimental agreement of mobility field dependence in both the case of molecules that are known to have energetic disorder that is typically correlated in space, and molecules with typically uncorrelated disorder [93]. However, this method is significantly more complex and computationally intensive, requiring multiple iterations of expensive density functional theory (DFT) calculations.

Since the early work of Bässler [23], KMC modelling has been used extensively to investigate various properties of organic semiconductors, including temperature- and thickness-dependence of current-voltage characteristics [7, 94, 95], correlation between morphology characteristics and device efficiency [95–97], effects of carrier density on

mobility [98], and the relative contribution of exciton transfer mechanisms to exciton-exciton annihilation processes [99]. In addition, *ab initio* calculations coupled with KMC simulations have recently been used to predict triplet-triplet annihilation rates [88] and efficiency roll-off [87] in phosphorescent OLED blends in a parameter-free manner, showing good agreement with experimental results. KMC modelling has also recently been used in the field of organic photovoltaics to highlight the roles of entropy and charge delocalisation in the separation of excitons at the interface between two phases [83, 100]. The group of Kassel *et al.* showed that proper consideration of entropy is crucial to explaining the experimentally observed efficiency of exciton separation [100], and have additionally proposed a delocalised KMC scheme in which polaron states are calculated in a manner that accounts for partial delocalisation of a charge across nearby molecules, rather than simply assuming that it is localised to a single molecule [83].

Kinetic Monte-Carlo Optimisation

The computational complexity of KMC simulations requires the use of various approximations (such as classical hopping rates and cut-off radii) in order to simulate relatively large systems (on the scale of tens to hundreds of nanometers). However, even when significant simplifying approximations are used, and especially when they are not appropriate, computational optimisation can allow for improvements in simulation time, and enable modelling of larger and/or more complex systems within shorter time-frames. There are a number of optimisation techniques for Monte-Carlo simulations, of which this section presents a selective review with a focus on those relevant to KMC charge and exciton simulations.

The core algorithm behind KMC simulations involves repeatedly calculating the probability of all events, and then choosing one of them to perform. Event rate calculation inherently lends itself well to parallelisation, since the they are typically independent of each other and can therefore be calculated simultaneously [101]. In large systems, there could be tens or hundreds of thousands of possible events at a given time, so efficient parallelisation of rate calculations presents the opportunity for significant speed-up. In particular, KMC simulations are well-suited to parallelisation on graphics processing units (GPUs), which are capable of handling thousands of parallel execution threads through the use of single instruction multiple data (SIMD) architecture [102]. Under SIMD architecture, a given set of parallel threads (32 in the case of typical GPUs) execute the same instructions simultaneously on different data. This aligns well with Monte-Carlo rate calculation, in which the same rate equation is evaluated for all neighbours of all relevant particles. The down-side to SIMD architecture is that it is inefficient in the case that threads sharing an instruction set have diverging logic, but this is generally easy to avoid in the context of KMC modelling.

KMC models can also be further parallelised using domain decomposition techniques, in which the simulation box is divided into smaller sections. Parallel KMC simulations are performed on each of these sections, and information is exchanged

across boundaries after some time interval [103]. It is necessary to maintain time synchronisation, and this can be achieved (among other methods) by the introduction of null events, so that the sum of all event rates (including the null event) is the same in each domain. Hence, the simulation time can be advanced based on this value, while N simultaneous (and possibly null) events are executed in the N different domains [103]. However, there is a trade-off between accuracy and computational overhead depending on the frequency of communication between domains, particularly in the case of charge transport where long-range Coulomb interactions can play an important role, or at high carrier densities where conflicts at the domain boundary become more likely.

Besides parallelisation, another common method for optimising KMC simulations is to reduce the number of required event rate calculations per step. One way to achieve this is to only update selected rates after an event. For example, updating the rates of a particle only after it has made a hop can provide significant speed-up [32]. However, this can introduce error due to changes in the local environment between when a rate was calculated and when the event actually occurred [32]. A more accurate method (with more computational overhead) is to update the rates of all particles within some cut-off radius of the particle that last moved, but this method can still introduce some error due to long-range Coulomb interactions. An alternative approach is to utilise coarse-graining in order to reduce the occurrence of hops between states that make up a collective local minima. In this method, an aggregation technique such as the watershed algorithm is used to identify groups of states that make up a local minima, in which hops within the group are relatively likely compared to hops that leave the group [24]. These states are then collected into a single macro-state, and transport is modelled as hops between macro-states. Repeated hops between states within a local minima can cause appreciable slow-down in standard KMC simulations, and this method is quite effective at avoiding that, but to do so it sacrifices explicit treatment of particle-particle interactions, and instead considers them based on probability distributions of particles across the components making up the macro-states.

The remainder of the optimisation methods we will cover here relate to the handling of electrostatic interactions between charges. A naive approach of re-solving for the electrostatic potential at every source and possible destination site of every charged particle scales poorly as $O(N^2)$, where N is the number of particles. However, this can be drastically improved through carefully constructed algorithms. To start with, one can take advantage of the fact that for a given time step, only one charge moves at a time, and therefore the solution for the electrostatic potential in the system can simply be updated by subtracting the component due to the charge in its previous location, and adding back its contribution from the new location [104, 105]. This method can be parallelised very efficiently under a SIMD architecture, since updating the potential at a given location does not require inter-thread communication or diverging logic. As it relies on a global solution including the influence of all charges in the system, this update method introduces a self-interaction error in its naive form,

but this is easily corrected when calculating hopping rates by using correction factors which can be pre-calculated for speed. Li and Brédas introduced two methods for this, termed the "exact" and "exclusion" methods [106]. The "exclusion" method works by simply ignoring the contribution of the hopping charge to the overall electrostatic potential, whereas the "exact" method adds a correction to give the difference between the charge's energy at the destination site and its current site. This distinction is subtle, and in the case of a simple system with a homogeneous dielectric constant and without periodic or metallic boundary conditions, the two methods are essentially identical. However, in the common case that these conditions are not satisfied, and therefore image charges must be considered, the "exact" method accounts for the movement of the image charges, while the "exclusion" method simply ignores them. With regard to implementation, the "exclusion" method only requires the influence of the hopping charge in its current location to calculate the correction factor, whereas the "exact" method also requires the influence of the charge on the proposed destination site. As such, initial calculation of the correction factors for the "exact" method is slightly more time consuming, but once they are calculated, use of the correction factors in both cases simply requires a memory lookup and addition operation.

Another consideration when handling Coulomb interactions is the treatment of image charges. In KMC simulations, it is common to make the assumption of periodic boundary conditions to limit the system to a computationally feasible size [23,106,107]. This method assumes that a charge crossing a periodic boundary on one side of the simulation box re-enters from the opposite boundary, and so the modelled system represents one small section of the overall device that is repeated infinitely in the periodic directions (see Figure 2.5). When modelling OLEDs, simulations are typically performed on sandwich-structure devices, in which layers of organic semiconductor material are sandwiched between two parallel planar electrodes, giving metallic boundaries in one direction and periodic boundaries in the other two [108, 109]. For both periodic and metallic boundaries, correct treatment of Coulomb interactions requires the consideration of image charges, leaving the question of how many of the infinite periodic images should be included. A simple method is to introduce a cut-off radius, beyond which Coulomb interactions are ignored [32,103]. However, this causes discontinuities at the edge of the cut-off radius which can introduce error, particularly when the cut-off radius is relatively short [32]. Coulomb interactions in periodic systems also converge slowly [110, 111], and hence methods such as the Ewald sum are commonly employed. The Ewald sum approximates the potential due to infinitely periodic Coulomb interactions with high accuracy, while enabling fast convergence by splitting the potential into a short-range component that converges quickly in real space, and a long-range component that converges quickly in Fourier space [77, 112, 113]. This allows the use of computationally feasible cut-off radii without the introduction of discontinuities, and the Ewald sum is used in many applications beyond just KMC modelling [110, 111, 114]. However, one limitation of the Ewald sum method, along with other image charge-based methods, is the inability to easily handle dielectric

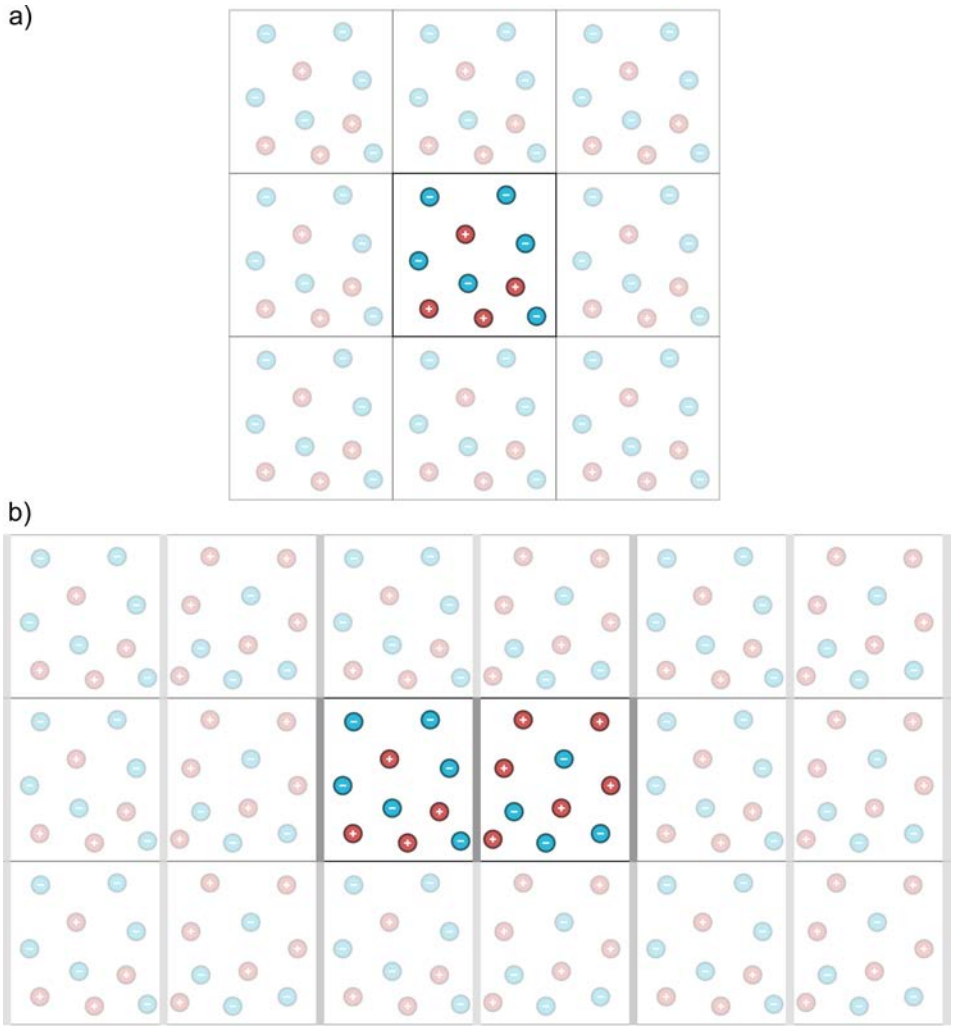

Figure 2.5: Examples of periodic boundaries in a 2D system showing one image in each direction (a) without and (b) with metallic boundaries in one direction. Note that in the case of a metallic boundary, the system is reflected around that boundary to form the periodic unit cell, with the signs of charges inverted in the reflected half.

interfaces, and we will discuss this further in Chapter 3.

2.2.2 Structure

Molecular packing structure in organic semiconductors is known to have significant effects on device operation [115–118]. In early KMC transport models, hopping sites were assumed to be fixed on a cubic lattice for the sake of simplicity, and the simulated layer was generally treated as homogeneous [23, 119]. While more accurate methods are now feasible, the lattice approximation is still often used in recent works [37, 103, 108]. A more realistic way of modelling molecular packing structure, however, is through the use of molecular dynamics (MD) simulations, which can further be classified as atomistic or coarse-grained MD [32]. In classical atomistic MD, forces on individual atoms due to both bonded and non-bonded interactions are calculated using a parameterised classical forcefield, and as such, the length

scale is typically limited by the number of interacting atoms to tens of nanometers [114, 118, 120, 121]. Alternatively, coarse-grained MD simulations group molecular fragments into single entities with parameterised interactions, thus enabling larger scale simulations at the cost of atomistic detail. While computationally expensive, these methods can unveil information about morphology that is difficult to observe experimentally [70]. For example Lee *et al.* recently showed that the phosphorescent emitter bis(2-phenylpyridine)(acetylacetonate)iridium(III) [$Ir(ppy)_2(acac)$] in vacuum deposited OLED blends tends to have preferential alignment of transition dipole vectors parallel to the substrate, resulting in better out-coupling efficiency when compared to the similar *fac*-tris(2-phenylpyridine)iridium(III) ($Ir(ppy)_3$) which has isotropic emission [120]. Finally, an alternative approach is that of a metropolis Monte-Carlo model, in which molecules (potentially treated with atomistic detail) are allowed to evolve in space through a Monte-Carlo process informed by a parameterised forcefield [122,123]. Random trial moves are proposed, and moves that reduce the total energy are accepted, while moves that increase energy are conditionally accepted based on a Boltzmann factor. Such simulations are able to produce a good representation of a film's steady-state molecular structure at lower computational cost than classical MD techniques by limiting the number of molecules that are allowed to move after a new molecule is deposited, and by disregarding the dimension of time. However, depending on the properties of interest, this loss of detail is not always acceptable.

With regard to the method of performing classical atomistic MD simulations, the simple approach is to place molecules into a fully periodic simulation box, and allow the system to equilibrate while adjusting the length of the periodic dimensions until the correct density is reached [124–128]. However, it was recently shown that morphology more reflective of reality can be obtained by explicitly including interfaces between the organic layer, the substrate, and the vacuum [118,120,121]. This was shown in the case of vacuum deposition by Tonnelé *et al.*, who simulated the vacuum deposition process in atomic detail by incrementally dropping randomly oriented molecules onto a graphene substrate in order to build a phosphorescent OLED active layer [118]. More recently, Lee *et al.* performed simulations of the solution deposition process in a similar manner, allowing solvent molecules to boil off naturally at the solution-vacuum interface, after which they were removed from the system [121]. This showed that inclusion of the substrate and vacuum interfaces resulted in nucleation and growth of the film, in contrast to previous methods involving randomly deleting solvent molecules within a fully periodic system which inevitably lead to spinoidal decomposition (spontaneous phase separation) [121, 126–128]. In addition, the results of Lee *et al.* suggest it is plausible that some solvent remains trapped in the layer on experimentally relevant timescales, which could potentially offer some explanation towards the difference in performance between vacuum and solution deposited devices - a topic we will return to in Chapter 7. We note that since a metropolis Monte-Carlo method is inappropriate for simulating the solution deposition process, atomistic MD simulations will be used in this work.

2.3 Summary

In summary, computational modelling plays a key role in elucidating structure-property relationships in organic semiconductors, allowing for detailed analysis of processes that are otherwise difficult to observe. Kinetic Monte-Carlo modelling is particularly powerful, allowing explicit consideration of particles and their interactions, which can be directly linked to the underlying morphology. This is especially useful when combined with molecular dynamics structure modelling, providing a pathway from molecular properties to bulk device characteristics.

3

Computational Methods for Monte-Carlo Modelling

In this work, kinetic Monte-Carlo modelling will be used to gain insight into the operation of organic light-emitting diodes, with a focus on the effects of emissive layer morphology on the performance characteristics of phosphorescent OLEDs. The KMC model will be developed from scratch to allow for customised input/output and fine-grained control over event handling, as well as implementation of GPU acceleration and other optimisation techniques as part of the core framework. Where feasible, the active layer morphology will be determined using molecular dynamics simulations of the vacuum and solution deposition processes in atomic detail. This will be achieved using the `GROMACS` package [129], following the methods developed by Tonnelé *et al.* and Lee *et al.* [118, 121].

This chapter provides details of the KMC algorithms and optimisation techniques implemented throughout the development process. We begin with an overview of the KMC framework, along with details of event rate calculations and handling of electrostatic interactions. In Section 3.3, optimisation of the event selection algorithm is discussed, and a novel method is presented. Section 3.4 then gives an overview of the methods used to measure device properties, followed finally by Section 3.5, which discusses benchmarking techniques and results. Section 3.5.1 additionally describes results that form part of the article:

[3] Siddhartha Saggar, Stephen Sanderson, Desta Gedefaw, Xun Pan, Bronson Philippa, Mats R. Andersson, Shih-Chun Lo, and Ebinazar B. Namdas. Toward Faster Organic Photodiodes: Tuning of Blend Composition Ratio. *Advanced Functional Materials*, 2010661 (2021). doi:10.1002/adfm.202010661

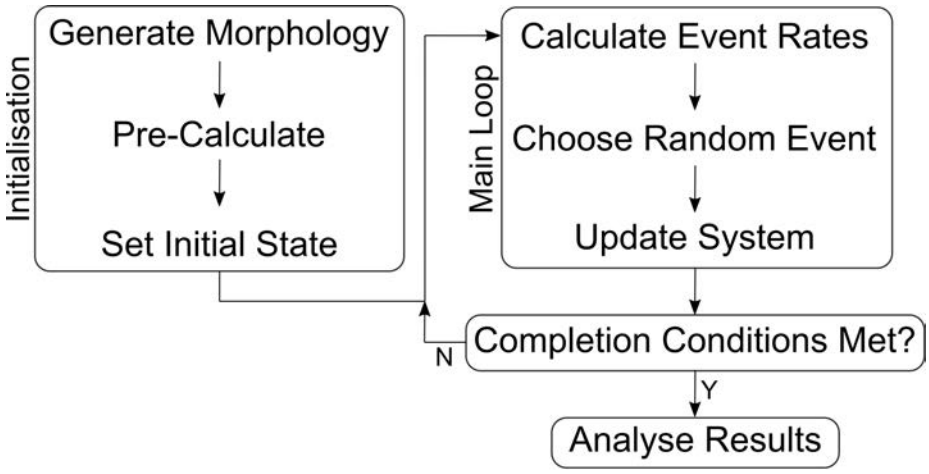

Figure 3.1: Outline of the kinetic Monte-Carlo simulation framework.

3.1 Kinetic Monte-Carlo Framework

The basic operation of the KMC model is outlined in Figure 3.1, and can be described in three main steps that are performed repeatedly until some completion condition is reached (e.g. a specified amount of time has elapsed, or there is nothing left in the system). Firstly, a list of possible events is built, including charge and exciton hops between molecular sites, injection or removal of charges, and decay of excitons. Rates are obtained for each event such that the probability of an event occurring is given by [23, 82]

$$P(n) = \frac{\nu_n}{\nu_{\text{tot}}}, \tag{3.1}$$

where ν_n is the rate of the event, and ν_{tot} is the sum of all event rates. Note that in the case of domain decomposition, where events are performed simultaneously in different physical areas of the system, ν_{tot} would be the sum of all event rates within a given domain, and null events would be used so that ν_{tot} is equal for each domain [103]. However, domain decomposition was not implemented in this work due to the high degree of complexity it adds relative to the expected performance gain.

Once event rates are calculated, a single event is chosen based on a uniform random number. In this work, to ensure good quality random number generation, the random numbers were sampled using the permuted congruential generator (PCG) algorithm as implemented in the `pcg-cpp` library [130]. Details of how this process was optimised are provided in Section 3.3.

Finally, the chosen event is performed, and the system time is updated by a random increment [23, 82]

$$\Delta t = \frac{-\ln(\xi)}{\nu_{\text{tot}}}, \tag{3.2}$$

where ξ is a uniform random number on the interval $(0, 1]$. Note that the time step scales by the sum of all event rates, so although only one event is allowed to occur at a time, the presence of more possible events reduces the time step, thereby preserving correct rates in the long time limit [82]. If the event resulted in the addition, removal,

or movement of a charge, the electrostatic environment was updated as described later in Section 3.2.3. Each event was logged to a trajectory file for future analysis in the form of the simulation time, the event type identifier, and any extra information about the event such as which particle underwent the event, and which site it moved to if it moved. This allowed for in-depth analysis with minimal file sizes, as each event required at most 5 bytes of data.

3.2 Rate Calculation

To ensure accuracy, event rates were updated for every particle after every Monte-Carlo move. The following sections provide details of the rate formulae. In all cases, the majority component of the rate was pre-calculated for speed, and only the energy difference component for charge-hops was re-evaluated, since that is the only part that changes between Monte-Carlo steps.

3.2.1 Charge Hopping

The two most commonly used methods for calculating charge hopping rates in organic semiconductors are the Miller-Abrahams and Marcus formalisms. Miller-Abrahams rates are the simpler of the two, and give a transfer rate from site i to site j of [23]

$$\nu_{ij}^{(\mathrm{MA})} = \nu_0^{(\mathrm{MA})} \exp\left(-2\gamma\left|\mathbf{r}_{ij}\right|\right) \begin{cases} \exp\left(\frac{-\Delta\mathcal{E}_{ij}}{k_\mathrm{B}T}\right), & \Delta\mathcal{E}_{ij} > 0, \\ 1, & \Delta\mathcal{E}_{ij} \leq 0, \end{cases} \tag{3.3}$$

where $\Delta\mathcal{E}_{i,j} = \mathcal{E}_j - \mathcal{E}_i$ is the difference in energy between the initial and final states, $\mathbf{r}_{ij}$ is the displacement vector of the hop, γ is the inverse localisation radius of the charged state, and $\nu_0^{(\mathrm{MA})}$ is the attempt to hop frequency. For hops between different types of molecules, $\nu_0^{(\mathrm{MA})}$ is taken as the geometric mean of the attempt to hop frequencies of those two molecules, $\sqrt{\nu_0^{(i)}\nu_0^{(j)}}$ [7, 131].

The Marcus transfer rate is given by [26, 27]

$$\nu_{ij}^{(\mathrm{MH})} = \frac{2\pi}{\hbar} \frac{H_{ij}^2}{\sqrt{4\pi\lambda_{ij}k_\mathrm{B}T}} \exp\left(-\frac{\left(\Delta\mathcal{E}_{ij}+\lambda\right)^2}{4\lambda_{ij}k_\mathrm{B}T}\right), \tag{3.4}$$

where, as shown previously in Figure 2.1, H_{ij} is the electronic coupling, and λ_{ij} is the reorganisation energy. Both of these formalisms are approximations towards a full quantum description, and both have been shown to give reasonable results for small molecule organic semiconductors [86]. While capability for both types of rate calculation was built into the developed KMC software, Miller-Abrahams rates were used in this work as they were generally simpler to parameterise.

The energy of site i has two components; the intrinsic site energy, which includes the EA/IP and any energetic disorder contributions, and the electrostatic potential, which includes any applied electric field, as well as Coulomb interactions between charges. In this work, IP and EA values were assumed to be equal to the HOMO and

LUMO levels respectively, with values taken from literature. Energetic disorder was included using the Gaussian disorder model. Coulomb interactions were calculated as described in the forthcoming Section 3.2.3. Capability for handling a global electric field that is independent of electrodes was also included in the model, and this was implemented simply as

$$\Delta\mathcal{E}_{ij}^{(E)} = \mathbf{E} \cdot \mathbf{r}_{ij}, \tag{3.5}$$

where $\mathbf{E}$ is the vector representing the applied field. Hence, the total energy difference for a charge hop is given by

$$\Delta\mathcal{E}_{ij} = q\Big(\mathcal{E}_j - \mathcal{E}_i + \Delta\mathcal{E}_{ij}^{(E)} + \phi_j - \phi_i\Big), \tag{3.6}$$

where q is the charge of the particle, $\mathcal{E}_i$ is equal to the EA (IP) plus an energetic disorder component randomly sampled from a Gaussian distribution of width σ, and ϕ_i is the electrostatic potential at site i due to the applied bias and all Coulomb interactions.

3.2.2 Charge Injection

Charge injection was modelled as a perpendicular hop from the electrode to the destination site, the rate for which was again calculated using the Miller-Abrahams equation (Eqn. 3.3) [119, 132]. In this case, the energy difference for injection to site i is given by [133, 134]

$$\Delta\mathcal{E}_{\text{injection}} = q_{\text{e(h)}}\left(\phi_i - \phi_{\text{electrode}}\right) + \frac{q_{\text{e(h)}}^2}{16\pi\varepsilon\left|\mathbf{r}_{\perp}^{(i)}\right|} + \mathcal{E}_i - \mathcal{E}_f, \tag{3.7}$$

where $\phi_{\text{electrode}}$ is the potential applied to the injecting electrode, $\mathbf{r}_{\perp}^{(i)}$ is the perpendicular distance to site i, ε is the dielectric permittivity, and $\mathcal{E}_f$ is the Fermi level of the electrode. These rates were calculated for all molecular sites within a short distance of the electrode plane. Charge removal at the electrode was considered for these same sites, and the removal rates were evaluated in an identical manner, using $\Delta\mathcal{E}_{\text{removal}} = -\Delta\mathcal{E}_{\text{injection}}$ with the influence of the candidate charge on the electrostatic potential excluded.

Note, the energy penalty for injection includes a term that captures the energy required to separate the charge from its image seen across the electrode [133, 134]. The equation above makes the assumption that only the primary image across the injecting electrode contributes to this injection energy, but the situation becomes more complex with the introduction of periodic boundaries and an opposite electrode due to the increased number of images, and is particularly difficult in the presence of dielectric interfaces or electrode structures other than parallel planes. However, it has been shown that in general, the energy to place a charge in a system is equal to half the sum of the energy due to all of its image charges [134]. As will be discussed in the following section, the energy for a charge on each site was pre-calculated, and these pre-calculated values could also be utilized to compute the injection penalty. This

method allows for fast computation in a way that is independent of the surrounding system, and could therefore be expanded to more complex system structures such as those seen in field effect transistors. However, we note that in simulations where the exact details of charge injection are not important, such as when ideal contacts are assumed, the simple solution presented in Eqn. 3.7 is a sufficient approximation.

In the case of Ohmic contacts (the ideal injection case), it was assumed that $\mathcal{E}_i$ was equal to the Fermi level. To maintain the required Ohmic contact condition of zero field at the electrode interface [135], injection rates for electrons (holes) were scaled by a pre-factor of

$$\alpha_{\mathrm{e(h)}} = \max\left(\beta\frac{Q}{q_{\mathrm{e(h)}}}, 0\right), \tag{3.8}$$

where Q is the surface charge on the electrode, and β is a scaling factor related to the fraction of the periodic electrode surface able to contribute to the injection event. In this work, a β value of 0.03 was used to ensure that injection was sufficiently fast to maintain an average steady state electric field of 0 at the electrode surface. Note, however, that results are quite insensitive to this value, with no difference observed for tested β values between 0.01 and 0.5. The surface charge was calculated using Gauss's law,

$$Q = \varepsilon \oiint_S -\nabla\phi \cdot d\mathbf{A}. \tag{3.9}$$

The method for evaluation of the surface integral was dependent on the electrostatics solving method used, and will be described in the relevant parts of Section 3.2.3.

3.2.3 Electrostatics

Under the assumption that the hopping process is much faster than the waiting time between hops, electronic interactions between charges are governed by the electrostatics equation,

$$\varepsilon(\mathbf{r})\nabla^2\phi(\mathbf{r}) + \nabla\varepsilon(\mathbf{r}) \cdot \nabla\phi(\mathbf{r}) = -\rho(\mathbf{r}), \tag{3.10}$$

as derived from Maxwell's equations, where $\phi(\mathbf{r})$ is the electrostatic potential at position $\mathbf{r}$, ε is the dielectric permittivity, and ρ is the charge density. In the case of homogeneous permittivity, this simplifies to Poisson's equation,

$$\nabla^2\phi(\mathbf{r}) = -\frac{\rho(\mathbf{r})}{\varepsilon}. \tag{3.11}$$

Taking advantage of the superposition principle, the solution for the electrostatic potential was split into a contribution due to the applied voltage, and one due to Coulomb interactions. The applied voltage contribution was solved only once per morphology for a bias of 1 V. This solution was then stored, and simply multiplied by the actual applied bias at run time – an operation that can be performed quickly in parallel on the GPU for each hopping site. Similarly, updating for a change of ΔV at the electrode simply requires that the 1 V solution be multiplied by ΔV and added to the current solution. Note that to allow potential handling of more than two electrodes,

these templates were treated in a general way, with one template per electrode. Each template represents the solution for when its corresponding electrode has a potential of 1 V, and all other electrodes are grounded. Therefore, the change in the overall electrostatics solution due to a change in voltage at a given electrode can be obtained quickly using only the template for that electrode.

For Coulomb interactions, the electrostatics equation was solved using two different methods (described in detail in the following sections), with electrodes fixed at 0 V. Initially, an iterative finite difference method was used to allow for the possibility of including spatially varying dielectric permittivity, and this method is described in detail in Section 3.2.3. However, this method has limited accuracy in the case of spatial disorder, as is present in realistic morphology generated with molecular dynamics. An attempt was made to expand it to an iterative finite element method based on a tetrahedral mesh, but this was ultimately deemed too computationally expensive for the required system sizes. Note that iterative methods were used here because the matrix equation that describes the discretised system is too large to solve directly. Ultimately, to handle realistic morphologies where molecular sites are not aligned to a grid, the electrostatics problem was handled using a damped interaction method based on the Ewald sum, as described in Section 3.2.3. This was at the cost of being able to handle spatially varying permittivity, since inclusion of complex dielectric interfaces is extremely difficult in image charge methods. Additionally, charge injection energies were calculated using the method presented in Eqn. 3.7 for simplicity, since the simulations planned under this electrostatics method did not require detailed contact modelling.

In addition to electrode templates, pre-calculation was also utilised for handling Coulomb interactions to enable fast correction of self-interaction error as described by the "exact" method of Li and Brédas [106], and to speed up the iterative solver by using a predictor-corrector scheme. For a given morphology, the electrostatics problem was solved for a single charge in the system, once for each hopping site, and the potential at that site and each of its possible hopping targets was stored. Note that while appealing for fast updates, storing the entire solution would quickly become intractable even in moderately sized systems due to the massive memory requirements.

Finite Difference

With sites aligned to a cubic lattice, it is a simple step to approximate the derivatives $\nabla\phi$ and $\nabla\varepsilon$ using a first order central difference scheme. For example, for site x, y, z, the 2nd derivative of the potential is given by

$$\nabla^2\phi_{x,y,z} = \frac{\phi_{x-1,y,z} + \phi_{x,y-1,z} + \phi_{x,y,z-1} - 6\phi_{x,y,z} + \phi_{x+1,y,z} + \phi_{x,y+1,z} + \phi_{x,y,z+1}}{a^2}, \tag{3.12}$$

where a is the lattice spacing. Substituting this into Poisson's equation (Eqn. 3.11) gives the simple expression for an iterative update to ϕ,

$$\phi_{x,y,z}^{(n+1)} = \frac{1}{6}\left(\phi_{x-1,y,z}^{(n)} + \phi_{x,y-1,z}^{(n)} + \phi_{x,y,z-1}^{(n)} + \phi_{x+1,y,z}^{(n)} + \phi_{x,y+1,z}^{(n)} + \phi_{x,y,z+1}^{(n)} + a^2\frac{\rho_{x,y,z}}{\varepsilon}\right), \tag{3.13}$$

where $\phi_{x,y,z}^{(n)}$ is the current potential at site x, y, z, and $\phi_{x,y,z}^{(n+1)}$ is the updated potential. However, this simple method tends to have relatively slow convergence. Convergence can be sped up using the successive over-relaxation method [136, 137], in which $\phi_{x,y,z}^{(n+1)}$ is taken as a weighted average of the current value, $\phi_{x,y,z}^{(n)}$, and the proposed updated value. Hence, $\phi_{x,y,z}^{(n+1)}$ is given by

$$\phi_{x,y,z}^{(n+1)} = (1-\omega)\phi_{x,y,z}^{(n)} + \frac{\omega}{6}\left(\phi_{x-1,y,z}^{(n)} + \phi_{x,y-1,z}^{(n)} + \phi_{x,y,z-1}^{(n)} + \right.$$
$$\left. \phi_{x+1,y,z}^{(n)} + \phi_{x,y+1,z}^{(n)} + \phi_{x,y,z+1}^{(n)} + a^2\frac{\rho_{x,y,z}}{\varepsilon}\right), \tag{3.14}$$

where ω is the weighting parameter, and the condition $0 < \omega < 2$ is required for the solution to converge. The value of ω that gives the fastest convergence is problem-specific, and was found in this case to be approximately 0.9. Each iteration was performed on the GPU, so that the update to the potential at each site could be calculated in parallel. To avoid memory conflicts, a checkerboard pattern was used, such that half the site energies were updated simultaneously, while their nearest neighbours remained constant, and then the other half were updated to complete the iteration step [138].

To further speed up convergence, a predictor-corrector scheme was used that takes advantage of the single charge templates already being pre-calculated for self-interaction error correction. When a charge moved, its influence within the template range was subtracted from the current electrostatics solution, and added back in the new location so that the iterative solver begins from a solution state that is closer to the correct overall solution. Similarly, if a charge was injected or removed, its short-range influence was simply added or subtracted as required before solving iteratively as normal.

When calculating the induced electrode charge under this scheme (Eqn. 3.9), the surface integral was solved by summing the contribution of square elements with size $a \times a$. The electric field component of these elements was calculated using the first order finite difference

$$E_{x,y} = -\frac{\phi_{x,y,z\pm1} - \phi_{\text{electrode},z}}{a}, \tag{3.15}$$

where index $z+1$ is used for electrodes with a normal vector in the positive z direction, and $z-1$ for those with a normal vector in the negative direction. So, for example, the surface charge of an electrode with a normal vector in the positive z direction is given by

$$Q = \varepsilon a \sum_{x,y} \left(\phi_{\text{electrode},z} - \phi_{x,y,z+1}\right). \tag{3.16}$$

Ewald Sum

In the case of point charges, Poisson's equation for a periodic system can be solved using the method of images. The potential energy of a charge q_j due to another charge q_i is given by Coulomb's law,

$$\phi_{ij} = \sum_{\mathbf{p}} \frac{q_i q_j}{4\pi\varepsilon \left|\mathbf{r}_j - (\mathbf{r}_i + \mathbf{p})\right|}, \tag{3.17}$$

where $\mathbf{r}_i$ is the position of charge i, and the sum over $\mathbf{p}$ represents the inclusion of all periodic images of q_i. Hence, the total electrostatic potential energy in the system is given by

$$U = \frac{1}{2}\sum_{i,j}^{N}\sum_{\mathbf{p}} \frac{q_i q_j}{4\pi\varepsilon \left|\mathbf{r}_j - (\mathbf{r}_i + \mathbf{p})\right|}, \tag{3.18}$$

where N is the total number of charges. However, convergence of this sum is slow, and the introduction of a simple cut-off radius results in discontinuities that can cause error for charges near that interface. To overcome these problems, the Ewald sum is commonly used [104, 113, 123, 139]. It allows fast convergence of electrostatic interactions by decomposing the contribution of a point charge to the electrostatic landscape into a short-range component that converges quickly in real space, and a long-range component that converges quickly in Fourier space. Under this scheme, the expression for the total electrostatic energy in the system is given by [111, 112]

$$U = \frac{1}{4\pi\varepsilon_0}\left(\frac{1}{2}\sum_{i,j}^{N}\sum_{\mathbf{p}} q_i q_j \frac{\operatorname{erfc}\left(\alpha\left|\mathbf{r}_j - \mathbf{r}_i + \mathbf{p}\right|\right)}{\left|\mathbf{r}_j - \mathbf{r}_i + \mathbf{p}\right|} + \right.$$
$$\left. \frac{1}{2\pi V}\sum_{i,j}^{N} q_i q_j \sum_{\mathbf{k}\neq 0} \frac{\exp\left(-(\pi\mathbf{k}/\alpha)^2 + 2\pi \mathrm{i}\mathbf{k}\cdot(\mathbf{r}_i + \mathbf{p} - \mathbf{r}_j)\right)}{\mathbf{k}^2} + \frac{-\alpha}{\sqrt{\pi}}\sum_{i}^{N} q_i^2 \right), \tag{3.19}$$

where V is the volume of the periodic system, $\mathbf{k}$ represents a Fourier space basis vector, erfc is the complementary error function, and α is a convergence parameter. Note that the final term is a self-correction for the Fourier space term. While this expression is only convergent for a system with a net charge of zero in the periodic volume, this condition is automatically satisfied in the case of a metallic boundary, as the system can first be reflected around one boundary and the result treated as the periodic unit cell.

In this work, the electrostatic potential was evaluated on the GPU to allow parallel computation of the potential at all possible hopping sites. To avoid race conditions related to adding the influence of multiple charges to one site, the potential was evaluated for all sites in the system after each charge injection/hop/removal event. By keeping track of the current solution, only the influence of that one charge needs to be re-evaluated, which is simple to parallelize without requiring inter-thread communication or synchronization. To allow fast updates, a damped interaction scheme was

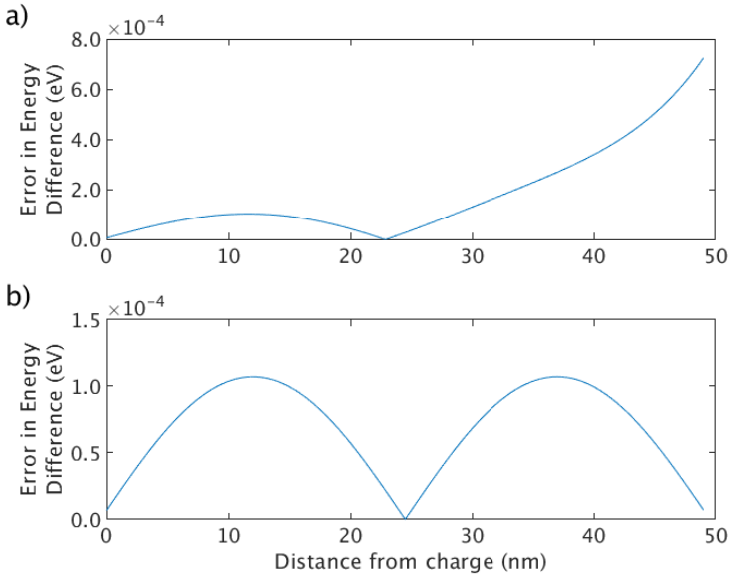

Figure 3.2: Absolute error in $\Delta\mathcal{E}_{ij}$ for a hop 1 nm towards or away from another charge as a function of the distance from that charge, with $\alpha = 0.03$ nm^{-1}, a relative permittivity of 2 (as is common in organic semiconductors), a 50 nm periodic boundary, and (a) one or (b) two periodic image(s) in each direction. For comparison, note that the iterative finite difference scheme described above was deemed to have converged when the maximum change due to an iteration was less than 5×10^{-5} eV.

used inspired by the Ewald sum method [123, 140]. With an α value of 0.03 nm^{-1}, it was found that the Fourier space component of the Ewald sum had only a minimal influence on the energy difference of a charge's hop, as shown in Figure 3.2 for the common case of 50 nm periodic boundaries. In the context of other approximations made for KMC modelling of OLEDs, and considering that typical energetic disorder gives a standard deviation of the site energy on the order of 100 meV [78], this amount of error was deemed acceptable given the performance increase it presented, and hence the Fourier space sum and related correction term were neglected in this work to allow for faster electrostatics evaluation. Hence, the potential energy of a charge q_j due to another charge q_i and its images was approximated as

$$\phi_{ij} = \sum_{\mathbf{p}} \frac{q_i q_j \mathrm{erfc}\left(\alpha \left|\mathbf{r}_j - (\mathbf{r}_i + \mathbf{p})\right|\right)}{4\pi\varepsilon \left|\mathbf{r}_j - (\mathbf{r}_i + \mathbf{p})\right|}, \tag{3.20}$$

noting that the self-energy, ϕ_{ii}, can be similarly calculated simply by excluding the $\mathbf{p} = 0$ case. This resulted in a scheme similar to that of the standard cut-off method, but without the introduction of significant discontinuities. Note that a cut-off radius was not specifically included here, but was instead enforced by the number of periodic images considered, and through the decay of the complementary error function.

When calculating the induced electrode charge (Eqn. 3.9) under this image charge scheme, the surface integral was evaluated using first-order Gaussian quadrature. The periodic electrode was divided into triangles with a maximum side length less than 1 nm, and the electric field at the center of each triangle was evaluated. This was done

using a first-order finite difference by solving for the electrostatic potential at a short perpendicular distance, δ, from that point (0.05 nm in this work). Hence, the induced electrode charge is given by the sum over all electrode triangles

$$Q = \varepsilon \sum_i A_i E_i, \tag{3.21}$$

where A_i is the area of triangle i. E_i is the electric field at the center of that triangle as given by $E_i = (\phi_{\text{electrode}} - \phi_i)/\delta$, where ϕ_i is the potential at the point close to the triangle's center. Note that triangles were chosen initially with a finite element electrostatics solver in mind to allow the possibility of rough electrodes approximated using a triangular mesh, and this idea may be revisited in the future if a sufficiently fast finite element solver is developed.

3.2.4 Exciton Dynamics

Excitons were assumed to form when an electron hops to the site of a hole, or *vice versa*, and such hops were assumed to always be energetically favourable for the sake of evaluating the Miller-Abrahams rate (that is, the Boltzmann factor was 1). Upon formation, excitons were allowed to diffuse through the system via both Dexter and Förster transfer events. Dexter transfer rates are typically modelled in terms of the Miller-Abrahams equation [7, 95, 108, 131, 141] (Eqn. 3.3), with the distinction that excitons are charge-neutral, and so the energy difference between sites for singlets (triplets) is given simply by the S_1 (T_1) energy difference (including the contribution of energetic disorder), and was assumed not to depend on the electrostatic potential. Note it was additionally assumed (as is common) that exciton transport occurs only via the first excited state, since higher energy states are typically very short-lived [41].

Förster transfer rates were calculated using the equation [32, 48, 51, 95, 142–144]

$$\nu_{ij}^{(\mathrm{F})} = \frac{1}{\tau}\left(\frac{R_0}{|\mathbf{r}_{ij}|}\right)^6 \begin{cases} \exp\left(\frac{-\Delta\mathcal{E}_{ij}}{k_\mathrm{B}T}\right), & \Delta\mathcal{E}_{ij} > 0, \\ 1, & \Delta\mathcal{E}_{ij} \leq 0, \end{cases} \tag{3.22}$$

where τ is the exciton lifetime, and R_0 is the Förster radius given by

$$R_0 = \sqrt[6]{\frac{9000c^4 \ln\left(10\chi^2\eta_{\mathrm{PL}}\right)}{128\pi^5 n^4 N_A} \int \frac{1}{\nu^4} f_\mathrm{D}(\nu)\, \varepsilon_A(\nu)\, d\nu}. \tag{3.23}$$

Here, c is the speed of light, n is the refractive index, N_A is Avogadro's number, η_{PL} is the photoluminescent quantum efficiency (the ratio of photons absorbed to photons emitted), χ^2 is the transition dipole alignment factor (typically assumed to be 2/3 for randomly oriented molecules), and $\int \frac{1}{\nu^4} f_\mathrm{D}(\nu)\, \varepsilon_A(\nu)\, d\nu$ is the overlap integral between the emission spectrum of the donor molecule, $f_\mathrm{D}(\nu)$, and the absorption spectrum of the acceptor molecule $\varepsilon_A(\nu)$ [145].

In addition to transfer events, excitons were also allowed to decay both radiatively and non-radiatively with a molecule-dependent rate. The radiative decay rate is given

by

$$\nu_{\text{Radiative}} = \frac{\eta_{\text{PL}}}{\tau}, \tag{3.24}$$

and similarly, the non-radiative decay rate is given by

$$\nu_{\text{Non-Radiative}} = \frac{1 - \eta_{\text{PL}}}{\tau}. \tag{3.25}$$

For simplicity, exciton-exciton and exciton-polaron interactions were assumed to occur when an exciton transfers to the site of another exciton or polaron, or when a polaron transfers to the site of an exciton. These interactions were handled according to Eqn. 2.1. While in theory, the presence of an exciton or polaron would have some effect on the transfer rates to that molecule (for example, the energy level or absorption spectrum may be altered), accurately quantifying these effects and dynamically taking them into account as the system evolves is a computationally difficult task, and hence the method utilised here provides a good first approximation that is efficient to implement under the KMC framework.

3.3 Event Selection

As shown previously in Equation 3.1, the probability of an event being chosen is given by its rate divided by the sum of all N event rates. Therefore, the chosen event, n, satisfies the condition

$$\sum_{i=0}^{n-1} \nu_i < \xi \sum_{i=0}^{N-1} \nu_i \leq \sum_{i=0}^{n} \nu_i, \tag{3.26}$$

where ξ is a random number on the interval $(0, 1]$. Thus, in addition to the sum of all event rates, selection of an event also requires the cumulative sum. As the latter inherently calculates the former, we will focus on optimising this cumulative sum.

When using GPU acceleration, one bottleneck is the overhead added by copy and move operations between system memory and GPU memory [146], so avoiding this bottleneck is generally beneficial to performance. As event rates in this work were calculated in parallel on the GPU, the results are stored in GPU memory. Rather than copy potentially tens of thousands of event rates to system memory, a more favourable solution is to calculate the cumulative sum directly on the GPU. While the cumulative sum (also known as a "scan") is not inherently conducive to parallelisation, GPU-based algorithms have been developed in order to make the best use of the available parallelism [147]. A brief overview of the work-efficient parallel scan algorithm follows.

We first consider a small array of N elements for the sake of demonstration. Initially, an up-sweep phase is performed with $N/2$ parallel threads, as illustrated in Figure 3.3. Each thread sums two neighbouring elements, storing the result in place of the second element. This is then repeated for those resultant sums, a total of $\log_2 N$ times, so that every second element of the original array has been modified, but the remaining elements (every first element) still hold their original values. As shown in

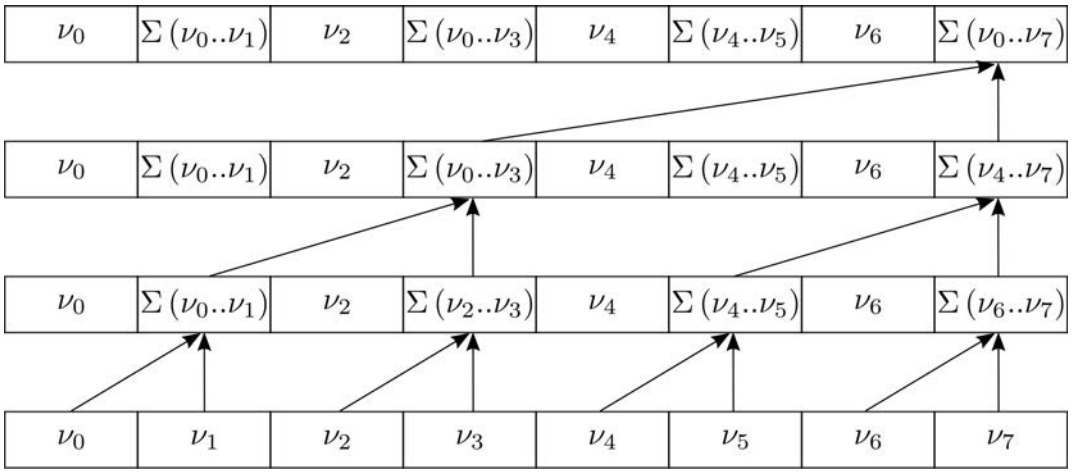

Figure 3.3: Parallel scan algorithm up-sweep phase.

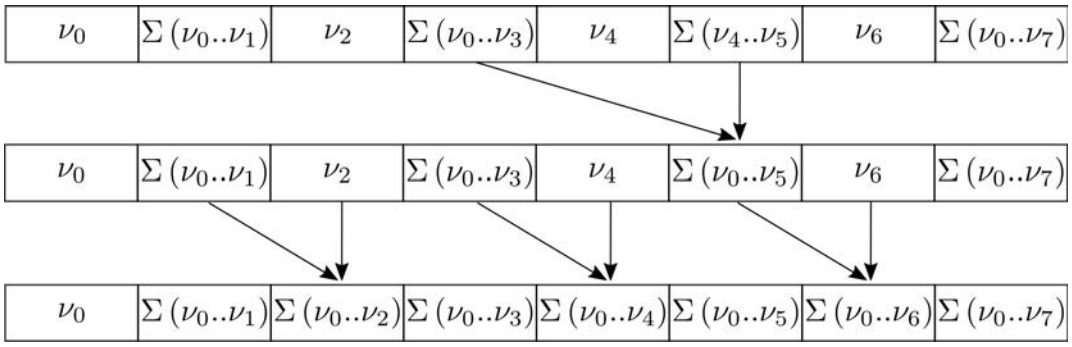

Figure 3.4: Parallel scan algorithm down-sweep phase.

Figure 3.4, a down-sweep phase is then used to update all elements such that each element of the array now contains the sum of all values from the original array up to that element. As this algorithm requires synchronisation between the parallel threads, the array size is limited. However, arrays of arbitrary size can be handled by breaking them into blocks, as shown in Figure 3.5. The cumulative sum of each block is found and stored, and then the total sums of each block are placed in an auxiliary array. The cumulative sum of that array is then found, and the resultant values are added back to their corresponding blocks so that the blocks (in sequence) now contain the cumulative sum of the entire array. For extremely large arrays, this process can be used recursively.

While the described parallel scan algorithm has been extensively optimised for GPU acceleration, we note that it is a general algorithm that must output a single, contiguous cumulative sum. However, this limitation is not strictly required for event selection. Instead, with a smart search algorithm, the down-sweep phase of the parallel scan can be skipped entirely, and instead the selected event can be determined from the result of the up-sweep phase – a method that is novel to the author's knowledge.

Upon performing the up-sweep phase as described above, which simultaneously calculates the sum $\nu_{\text{tot}} = \sum_{i=0}^{N-1} \nu_i$, the indices in a block between which the random number $\chi = \xi\nu_{\text{tot}}$ falls can be determined as follows. For a block size N_B, with 0-

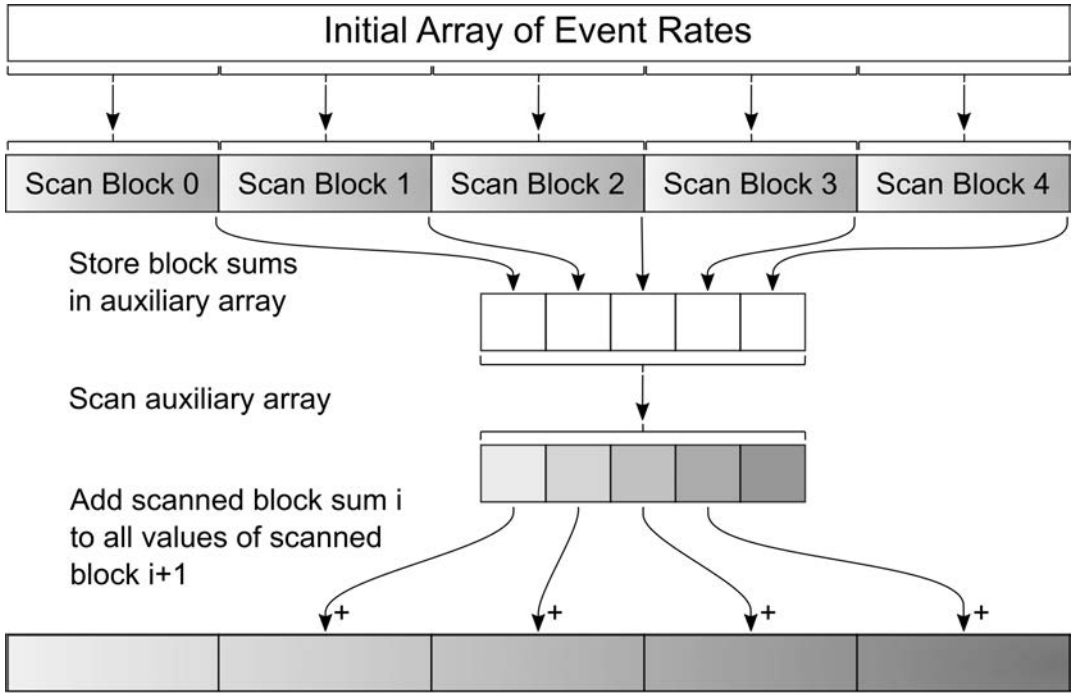

Figure 3.5: Parallel scan algorithm for large arrays [147].

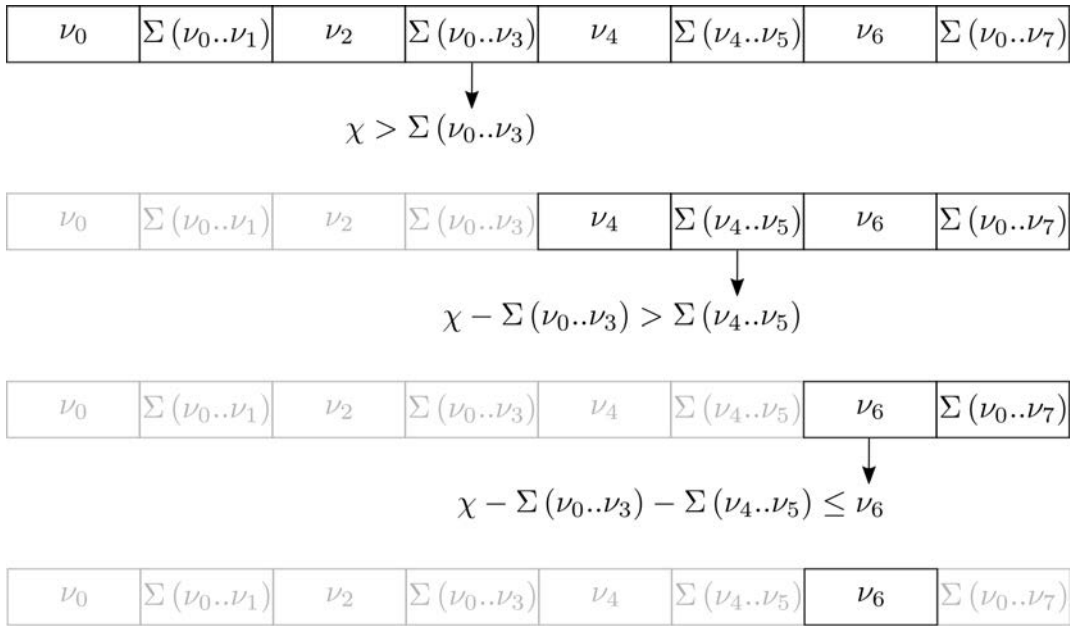

Figure 3.6: Example of searching the up-swept array for the case of $\chi = 0.3\nu_6 + \sum_{i=0}^{5} \nu_i$.

based indexing, determine whether χ is greater than the value at index $N_B/2 - 1$. If so, the index is offset by $N_B/2$, and the value at $N_B/2 - 1$ is subtracted from χ. In either case, the block half containing the selected index is then treated as a block in itself, and this process is repeated a total of $\log_2 N_B$ times until the chosen event is narrowed down to a single index. An example of this process is shown in Figure 3.6.

This algorithm scales to arrays of arbitrary size using a similar method to the standard parallel scan algorithm. The sum of each block is used to construct an auxiliary array as before, upon which the up-sweep phase is performed. The up-swept auxiliary array is then searched using the method described, yielding the index of the block that contains the selected event, and so the global index of the start of that block can be obtained by multiplying the index of the block by N_B. That block can then be searched by carrying forward the adjusted χ value from the auxiliary array search, and this process can be performed recursively as before for extremely large arrays.

3.4 Calculating Device Properties

While some device properties such as IQE are measurable simply by counting charges and events, others such as device current and charge mobility require more detailed sampling and calculations, and these are outlined below.

3.4.1 Current

In a KMC model where directions parallel to the electrodes are treated as infinitely periodic, device current is more conveniently measured as current density. As can be derived from Maxwell's equations, the device current is made up of two components: the conduction current, which reflects the charge flux through the electrode, and the displacement current due to change in the electric field at the electrode's surface. The conduction current density can be measured simply as

$$J_C = \frac{q}{A\Delta t}(p_{\text{inj}} - n_{\text{inj}} - p_{\text{rem}} + n_{\text{rem}}), \tag{3.27}$$

where p_{inj} (n_{inj}) is the number of injected holes (electrons) within the time period Δt, p_{rem} (n_{rem}) is the number of removed holes (electrons), and A is the surface area of the electrode. The displacement current is given by

$$J_D = \frac{\Delta Q}{A\Delta t}, \tag{3.28}$$

where ΔQ is the change in the induced charge on the electrode, taken as $Q(t + \Delta t) - Q(t)$, with Q calculated as described previously. Hence, the total current density is the sum of these two quantities,

$$J = J_C + J_D. \tag{3.29}$$

3.4.2 Mobility

Mobility is defined in terms of a charge's drift velocity under an electric field through

$$\begin{aligned} \mu_e &= \frac{v_d}{E}, \\ \mu_h &= \frac{-v_d}{E}, \end{aligned} \tag{3.30}$$

where μ_e and μ_h are the electron and hole mobility, respectively, and v_d is the average drift velocity of those charges in the direction of the field. Under a KMC scheme, this can be evaluated simply by taking the net displacement of all charges in the system within a given time interval. Alternatively, assuming an Einstein relation for the diffusion coefficient, mobility can also be evaluated based on the current density, J, and the number density of charges, n, by re-arranging the drift-diffusion equation

$$J = -e\mu nE - \mu k_{\mathrm{B}} T \frac{dn}{dx}, \tag{3.31}$$

where x is the direction of the electric field.

3.5 Benchmarking

Beyond the use of unit tests for core algorithms (e.g. event selection), the KMC model was systematically benchmarked against a number of known results to ensure accuracy.

Firstly, to ensure that energetic disorder was treated correctly, energetic relaxation simulations were performed and the results were compared to those of Bässler [23]. In these simulations, non-interacting charges were placed randomly in the system and allowed to thermalise. As shown by Bässler, the energetic density of states of the non-interacting charges is expected to be Gaussian in nature, with a steady-state mean of $\frac{-\sigma^2}{k_{\mathrm{B}}T}$, where σ is the standard deviation of the site energies (which are sampled using the Gaussian disorder model) and T is the temperature. Results from this benchmark are shown in Figure 3.7.

Next, to check that electric field and Coulomb interactions were properly handled, a blocking benchmark was used in which the steady-state charge density was compared against an analytical solution. Charges of a single polarity were injected from an Ohmic contact into the system under the influence of an electric field, and allowed to be removed at that same electrode. Charge removal at the opposite electrode was blocked, so that after some time the device current is zero, and the charge distribution reaches a steady state that can be found analytically by solving the drift-diffusion equation. In the case of holes injected in the x direction, the steady state is given by

$$J = 0 = ep(x)\mu_h E(x) - \mu_h k_{\mathrm{B}} T \frac{dp(x)}{dx}, \tag{3.32}$$

where $p(x)$ is the density of holes and e is the unit charge. The relationship between the electric field and the charge density is given by Gauss's law as discussed earlier,

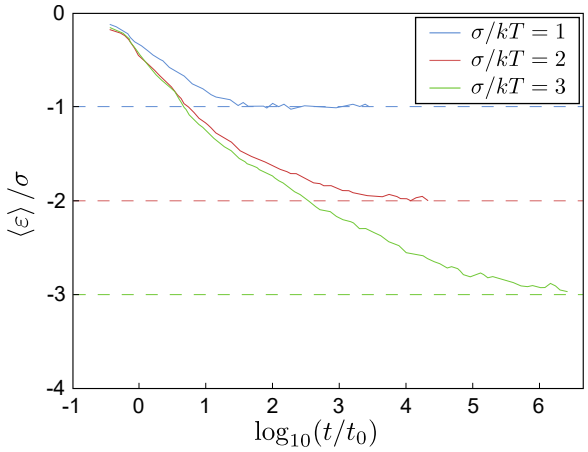

Figure 3.7: Relaxation benchmark results. Dashed lines show the expected steady-state energy. Note, time was scaled by $t_0 = (6\nu_0 \exp(-2\gamma a))^{-1}$ for clear comparison with the results of Bässler [23], where ν_0 and γ are the attempt to hop frequency and delocalisation radius from the Miller-Abrahams equation (Eqn. 3.3), and a is the lattice spacing.

and in this 1D case results in the expression

$$p(x) = \frac{\varepsilon}{e}\frac{dE}{dx}, \tag{3.33}$$

noting that $\rho(x) = ep(x)$. Hence the differential equation for the electric field is

$$0 = E(x)\frac{dE}{dx} - \frac{k_\mathrm{B}T}{e}\frac{d^2E}{dx^2}, \tag{3.34}$$

which yields the solution

$$E(x) = a\tan\left(ab + \frac{aex}{2k_\mathrm{B}T}\right), \tag{3.35}$$

where a and b are integration constants dependent on the boundary conditions. For an Ohmic contact at $x = L$, the electric field at that boundary must be 0, and therefore

$$\begin{aligned} E(L) = 0 &= a\tan\left(ab + \frac{aeL}{2k_\mathrm{B}T}\right), \\ 0 &= ab + \frac{aeL}{2k_\mathrm{B}T}, \\ b &= -\frac{eL}{2k_BT}. \end{aligned} \tag{3.36}$$

Hence the electric field is of the form

$$E(x) = a\tan\left(\frac{ae}{2k_\mathrm{B}T}(x - L)\right). \tag{3.37}$$

To avoid unphysical discontinuities, this equation is further constrained such that

$$\left|\frac{ae}{2k_{\mathrm{B}}T}(x-L)\right| < \frac{\pi}{2}, \tag{3.38}$$

which simplifies to

$$|a|\,|x-L| < \frac{\pi k_{\mathrm{B}}T}{e}. \tag{3.39}$$

As the left side of this equation is largest when $x = 0$, it therefore yields the constraint

$$|a| < \frac{\pi k_{\mathrm{B}}T}{eL}. \tag{3.40}$$

The other boundary condition on the system is the applied voltage

$$V = -\int_0^L E(x)dx, \tag{3.41}$$

which, after substituting the expression for $E(x)$, gives

$$V = \frac{k_{\mathrm{B}}T}{e}\log\left(1+\tan^2\left(\frac{aeL}{2k_{\mathrm{B}}T}\right)\right). \tag{3.42}$$

This can be solved for a to give

$$a = \frac{2k_{\mathrm{B}}T}{eL}\tan^{-1}\sqrt{\exp\left(\frac{eV}{k_{\mathrm{B}}T}\right)-1}. \tag{3.43}$$

Substituting $E(x)$ back into Gauss's law (Eqn. 3.33) gives the expression for the charge density

$$p(x) = \frac{a^2\varepsilon}{2k_{\mathrm{B}}T}\left(\tan^2\left(\frac{ae}{2k_B T}(L-x)\right)+1\right), \tag{3.44}$$

and hence the resultant steady state charge density from a KMC simulation under the same conditions can be compared to this solution to ensure correct handling of electrostatics, as well as charge injection and removal. Results for this benchmark are shown in Figure 3.8. Note that as the benchmark was performed using a cubic lattice of hopping sites (and not a continuum as assumed by the analytical solution), some difference is expected close to the electrode.

The final component of the model to benchmark is exciton diffusion and decay. An exciton decay rate of $\frac{1}{\tau}$ is expected to yield an average lifetime of τ, and this was verified simply by simulating a number of non-interacting excitons and measuring their lifetime. With correct lifetimes, exciton diffusion can then be benchmarked by comparing to experimental results. A number of articles give parameters for both Dexter and Förster transfer rates based on experimentally measured diffusion lengths [51,141,142,148], and therefore a correct KMC model simulating exciton diffusion under those parameters is expected to yield an average diffusion length close to the experimentally observed value.

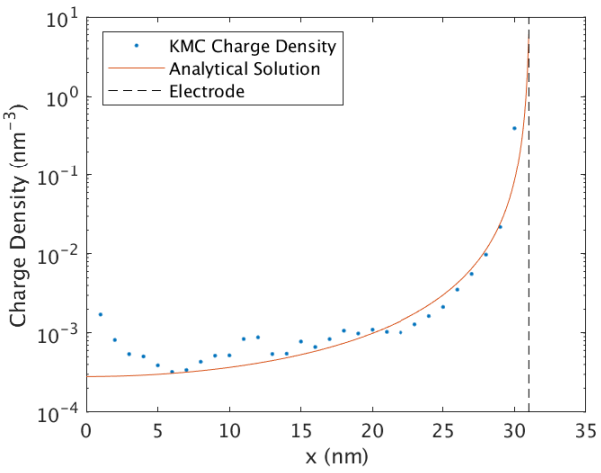

Figure 3.8: Blocking benchmark results for a $30 \times 30 \times 30$ cubic lattice of sites, with a 1 nm lattice spacing at $T = 11605$ K. Note the high temperature was used to enable relatively high charge densities for easy comparison. The results shown were obtained using the damped electrostatics scheme as described in Section 3.2.3, and identical results were also obtained using the finite difference electrostatics method.

3.5.1 Energetic Relaxation

We note at this point that although this work focuses on OLEDs, the described model is applicable to a range of organic semiconductor devices. For example, as part of a collaborative work, it was applied to organic photodetectors, and these results formed part of an article that has been published in *Advanced Functional Materials* (details provided at the beginning of this chapter). The focus of the article was on an improved organic photodetector blend that exhibited faster response time, and KMC modelling was required to explain differences observed between the mobility predicted by the photodetector response and the measured mobility under steady-state conditions.

At steady state, charge mobility is dependent on the electric field and the energetic disorder. However, in general, for a charge that has not relaxed in energy, its hops are more likely to be energetically favourable (and therefore have a higher rate), particularly in the direction of the electric field. This has the effect that a charge's mobility relaxes along with its energy over time, and this can have significant consequences for devices such photodetectors where photogenerated charges may not be energetically relaxed when they first enter the system [89, 149]. Indeed, as results from the model show in Figure 3.9, it is likely that the average mobility is significantly higher than the steady-state value for a photodetector with energetic disorder typical of common organic semiconductors, since response times on the order of microseconds are typical [150]. Furthermore, it has been shown by Heiber *et al.* that mobility relaxation can be additionally affected by the morphology of the film, with "dead end" pathways potentially leading to a *decrease* in mobility at higher electric fields due to that field trapping charges against a "dead end" [89].

The data in Figure 3.9 was generated using KMC simulations of a $50 \times 50 \times 50$ cubic lattice of sites, with a lattice spacing (a) of 1 nm, and periodic boundaries in

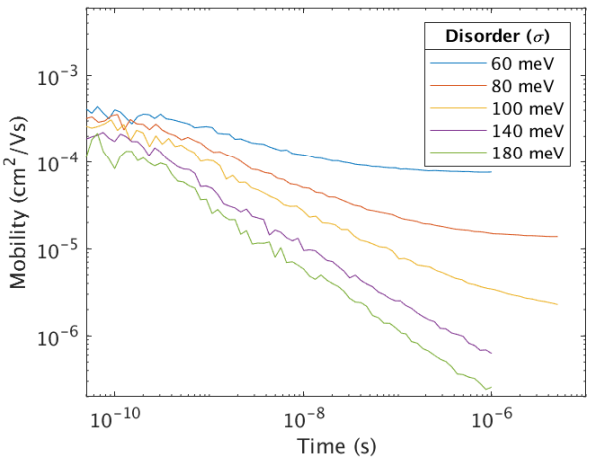

Figure 3.9: Mobility relaxation for various levels of energetic disorder at 300 K.

all directions. 100 holes were placed randomly in the system to give a typically low carrier density of 8×10^{17} cm^{-3}, and allowed to evolve in time under an electric field of 7.7×10^6 V/m; a value in the range typical of organic photodetectors [150]. Site energies were assigned using the Gaussian disorder model, with various standard deviations between 60 meV and 180 meV (values typical of organic semiconductors [32, 149]). Site-exclusion was enforced, such that a hop to an occupied site was forbidden, and Coulomb interactions were handled using the damped electrostatics scheme (see Section 3.2.3) with a relative permittivity of 3 [150]. Hopping events were allowed within a 3 nm radius, and rates were calculated using the Miller-Abrahams equation (Eqn. 3.3). The inverse localisation radius (γ) was chosen such that $2\gamma a = 10$ [23], and the attempt to hop frequency (ν_0) was taken as 1×10^{14} s^{-1} to give steady state mobility values that were in the realm of the organic photodetector blends presented in the article [3]. Mobility at a given time was determined based on the time-averaged drift velocity since the previous time point (see Eqn. 3.30). To obtain relatively noise-free data at low time values, at least 3000 repeat simulations were performed per disorder value, up to 5000 repeats for high values of energetic disorder, and the time-dependent mobility was averaged over those repeat runs.

In addition, the effects of electric field strength on mobility relaxation were also analysed, and these results are shown in Figure 3.10. As would be expected based on the Poole-Frenkel relation (that is, $\mu \propto \exp\left(c\sqrt{E}\right)$ where c is a constant [90]), an increase in electric field leads to a higher steady-state mobility, and this is accompanied by a higher steady-state energy. As the electric field increases, a larger fraction of potential hops in the direction of the field become ones which are downwards in energy, thereby increasing the likelihood of those hops occurring, and allowing access to energy levels higher in the density of states. The faster charge transport has the added effect of allowing for faster thermalisation of charges, as can be seen by the shorter times required to reach steady-state. It should be noted, however, that these results are for a homogeneous, fully periodic system and, as demonstrated by Heiber *et al.* [89], are not necessarily indicative of more complex morphologies.

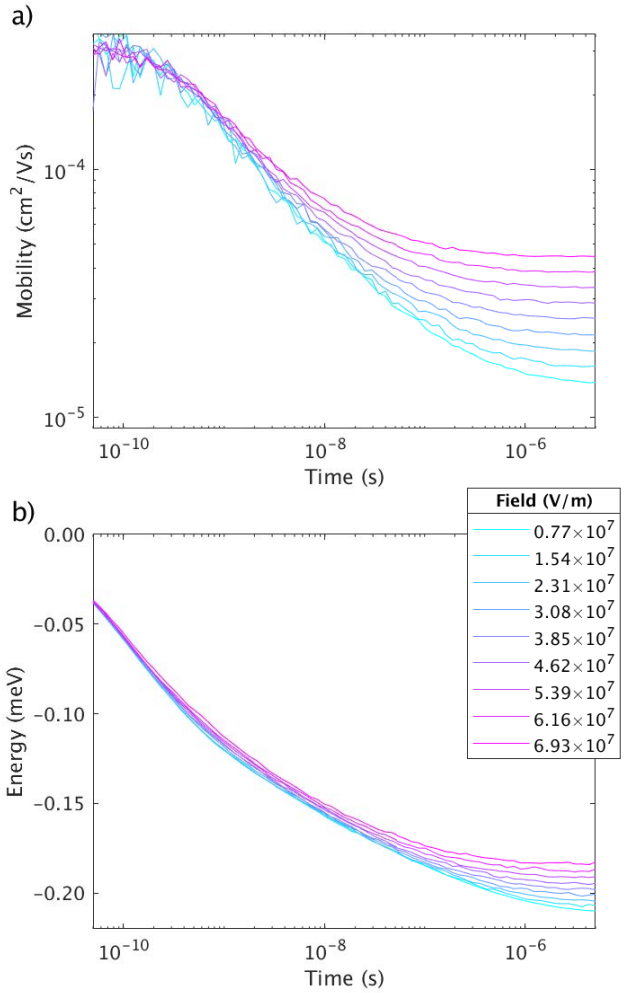

Figure 3.10: (a) Mobility and (b) energy relaxation for various electric field strengths in a system with Gaussian energetic disorder of width 80 meV. Note, the energy values are those of the intrinsic site energies, and do not include electrostatic contributions.

Summary

To summarise, a KMC model was developed that is capable of handling both charge transport and exciton dynamics, along with interactions between those particles. It was implemented such that GPU computation formed the core of the framework, thereby allowing massive parallelism while reducing the need for expensive memory copy operations. Towards this end, an event selection algorithm was developed that circumvents the need for a full computation of the cumulative event rate sum. The model was systematically benchmarked against known results and found to be in good agreement, showing that it is capable of producing reliable results. The following chapters present results obtained using this model throughout its various stages of development.

4

Charge Transport in Guest-Host OLEDs

This chapter contains material that was published in the journal article:

[1] Stephen Sanderson, Bronson Philippa, George Vamvounis, Paul L. Burn, and Ronald D. White. Understanding charge transport in Ir(ppy)3:CBP OLED films. *The Journal of Chemical Physics*, **150**, 094110 (2019). doi:10.1063/1.5083639

The capacitance measurement mentioned in this chapter was performed by the group of Prof. Paul Burn. The molecular dynamics deposition and annealing data was supplied by Dr. Thomas Lee and Prof. Alan Mark. All other work described in this chapter is my own, including the analysis of the MD deposition and annealing data.

4.1 Introduction

Currently, many of the most efficient phosphorescent organic light-emitting diodes (OLEDs) make use of a guest-host emissive layer structure, in which an emissive guest is blended in a host matrix to reduce the likelihood of exciton-exciton quenching interactions, and it has been demonstrated that such devices can approach an internal quantum efficiency (IQE) of 100% [50, 57, 61, 151]. To achieve high efficiency, typical guest-host blends have a low guest concentration (<20 wt%), and it is generally assumed that the guest is homogeneously distributed throughout the blend [58, 66, 118, 151, 152]. Average guest homogeneity in a blend film has been observed using neutron reflectometry measurements. For example, a blend of *fac*-tris(2-phenylpyridine)iridium(III) ($Ir(ppy)_3$) in 4,4'-bis(*N*-carbazolyl)biphenyl (CBP)

was shown to have an even concentration of the complex in the film normal to the substrate [153]. However, the resolution of the neutron reflectometry experiment is insufficient to conclude that the iridium complexes are fully dispersed and non-interacting in the blend. In fact, it was recently shown using molecular dynamics simulations that $Ir(ppy)_3$ guest molecules in a CBP host tend to have a number of neighbors that are metal complexes at concentrations as low as 5 wt%, and provide percolation paths throughout the blend at slightly higher concentrations [118]. Understanding how the guest distribution impacts on charge mobility is a key element in optimizing the efficiency of $Ir(ppy)_3$:CBP OLEDs, as well as other devices that contain guest-host blended active layers.

In this chapter, the effects of guest concentration on charge transport are investigated. In particular, the mobility dependence on guest concentration for an $Ir(ppy)_3$:CBP blend is explored under the assumption of a random guest distribution. This is then compared to the spatial distribution of charges relative to the guest molecules to gain insight into how the formation of guest clusters and percolative networks counteracts the impact of charge trapping on the guest molecules.

Section 4.2 outlines the methods used to generate the morphologies and simulate charge transport. The results are then presented in Section 4.3, and a summary is given in Section 4.4.

4.2 Simulation Methodology

Under the assumption that guest molecules are randomly distributed throughout the host, a cubic lattice morphology was generated by randomly assigning the desired percentage of sites as guest sites. Since each site is assumed to represent one molecule, the percentage of guest sites required to give the desired wt% was calculated based on the corresponding molar ratio. This calculated percentage was then used as the probability that an individual site is assigned as a guest.

A lattice spacing (a) of 0.8935 nm was implemented to achieve a molecular density similar to the blend film formed by molecular dynamics (MD) deposition and annealing simulations of 6 wt% $Ir(ppy)_3$ in CBP. As is common for many organic semiconductor transport models, site energies were chosen from a Gaussian distribution [23, 119, 154] with a standard deviation of 162 meV [155]. The system structure was one of parallel planar electrodes, with periodic boundaries in the orthogonal directions, and an overall system size of 71.5 nm×53.6 nm×53.6 nm to avoid finite size effects in the periodic directions [156]. Sample generated morphologies are shown in Figure 4.1.

As described in Section 3.2.1, charge transport was modelled using the Miller-Abrahams equation (Eqn. 3.3) to calculate hopping rate, with hops up to a distance of $3a$ in each direction considered as candidates to ensure that all probable hops were possible [23]. The inverse localisation radius (γ) calculated such that $2\gamma a = 10$ [23]. Coulomb interactions between charges were included using an iterative finite difference solution to Poisson's equation, as described in Section 3.2.3. A tolerance of 1×10^{-7}

Property	Value
Electron hop rate (ν_0^{e})	1.0×10^{12} s^{-1}
Hole hop rate (ν_0^{h})	2.0×10^{14} s^{-1}
CBP HOMO	-5.7 eV [158]
CBP LUMO	-2.6 eV [158]
$\mathrm{Ir(ppy)_3}$ HOMO	-5.3 eV [158]
$\mathrm{Ir(ppy)_3}$ LUMO	-2.9 eV [158]
Energetic Disorder	162 meV [155]
Relative permittivity (ε_{r})	2
Inverse localization radius (γ)	5.596 nm^{-1}
Lattice spacing (a)	0.8935 nm
Temperature (T)	298 K

Table 4.1: Simulation input values.
Hopping rates were chosen to give a mobility similar to that of neat CBP. Permittivity was determined from capacitance measurements. Inverse localization radius was calculated such that $2\gamma a = 10$ [23]. Lattice spacing was calculated to achieve a molecular density similar to that seen in MD deposition and annealing models of 6 wt% $\mathrm{Ir(ppy)_3}$:CBP.

V was used for solving the electrode contribution at unit voltage, and a tolerance of 1×10^{-5} was used for the contribution due to charges. The self-interaction error for charge hopping was suppressed using the 'exact' method of Li and Brédas [106], where the change in Coulomb energy for a hop from site i to site j is adjusted by adding the potential at site j due to a single charge on that site in an otherwise empty system, and subtracting the potential at the same site due to a single charge on site i. The electrostatic landscape was updated after every charge move.

Since the effects of realistic electrode injection were beyond the scope of this study, Ohmic contacts were assumed, and were implemented as described in Section 3.2.2. Similarly, exact exciton behaviour was also beyond the scope of this study, and therefore excitons were removed immediately upon formation (when an electron hopped to the site of a hole, or vice-versa).

A full list of system property and simulation values is presented in Table 4.1. The hopping rate values were chosen to give an electron mobility close to 3×10^{-4} $\mathrm{cm}^2/\mathrm{Vs}$ and a hole mobility close to 2×10^{-3} $\mathrm{cm}^2/\mathrm{Vs}$ [157]. For simplicity, the electron and hole mobilities of $\mathrm{Ir(ppy)_3}$ were assumed to be the same as those of CBP. The permittivity of CBP was determined from capacitance measurements.

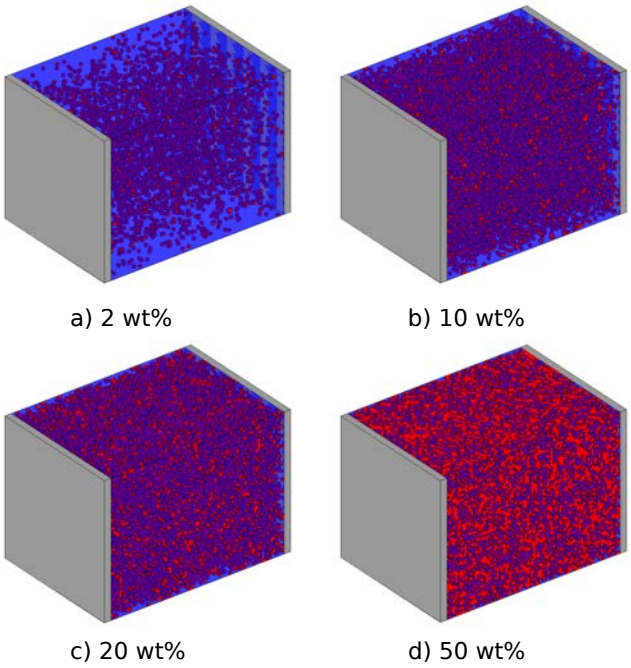

Figure 4.1: Example $Ir(ppy)_3$:CBP morphologies for various guest concentrations. Guest sites are designated red.

4.3 Results

Simulations were performed at various guest concentrations up to 50 wt% under biases of 5, 7, and 10 V; the range of potentials at which $Ir(ppy)_3$:CBP OLEDs are known to emit light with increasing luminance [159, 160]. At least three different morphology realizations were used for each concentration, and error bars were calculated as the standard deviation between morphologies. All simulation measurements were obtained based on time-averaging at steady state, which was identified through constancy in the charge concentration and device current. Mobilities were then calculated based on the drift-diffusion equation

$$J = -e\mu nE - \mu k_{\mathrm{B}} T \frac{dn}{dx}, \tag{4.1}$$

where J is the current density, E is the electric field, and n is the number density as a function of the direction of travel, x. The field dependence of the mobilities for the various blends were all found to follow a Poole-Frenkel form [90].

Results from these mobility measurements at various concentrations are shown in Figure 4.2, where a clear minima can be observed in the vicinity of the blend containing 10 wt% $Ir(ppy)_3$. This is most distinct at low voltages, with the curve flattening out significantly under higher bias (i.e., higher fields).

As shown in Figure 4.3, the HOMO and LUMO levels of $Ir(ppy)_3$ are within those of CBP, so the guest molecules act as traps for both electrons and holes. The average portion of time spent by a charge on a guest molecule is illustrated in Figure 4.4, which shows that charges are spending a large percentage of their time on the guest molecules, even at low concentrations. It also shows that electrons spend a lower fraction of time

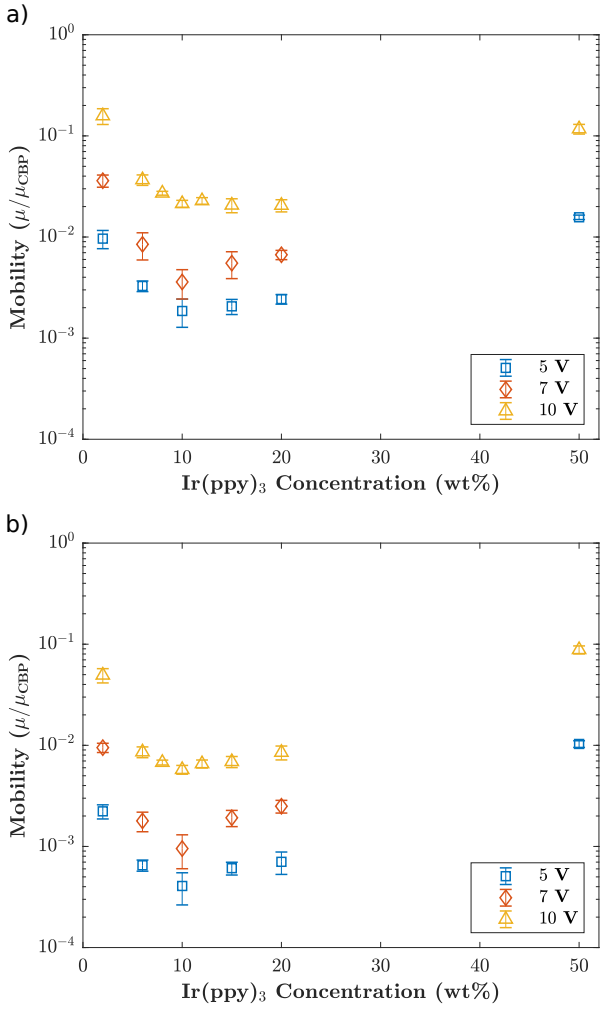

Figure 4.2: Mobility as a function of Ir(ppy)$_3$ concentration for (a) electrons and (b) holes under biases of 5, 7 and 10 V. The electron (hole) mobility was scaled by the mobility of electrons (holes) measured in a simulation of a pure CBP film under a 10 V bias.

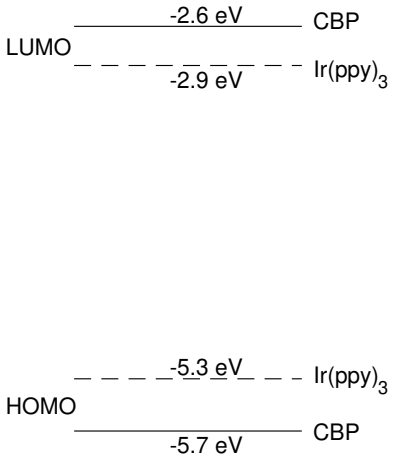

Figure 4.3: Energy levels of CBP (solid lines) and Ir(ppy)$_3$ (dashed lines).

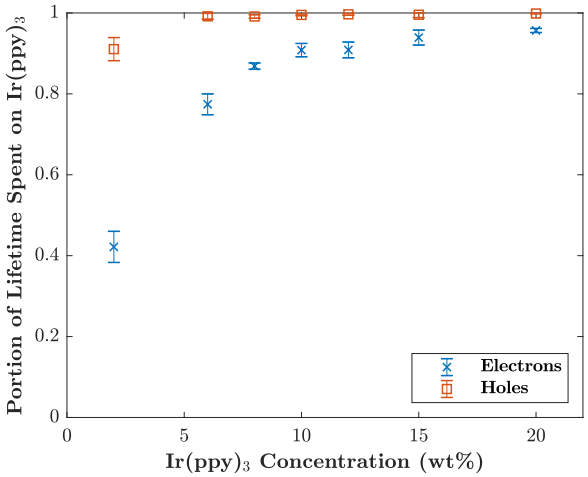

Figure 4.4: Occupation probability of a charge being on an $Ir(ppy)_3$ site as a function of $Ir(ppy)_3$ concentration, taken from the central region of the device to avoid the impact of the electrodes. The difference in probability for electrons and holes seen here is due to the lower trapping depth of electrons on an $Ir(ppy)_3$ molecule compared to that of holes. The displayed data was obtained with a bias of 10 V, but was found to be relatively independent of bias.

on the guest sites compared to holes, which may be due to the smaller difference between the LUMO levels compared to that between the HOMO levels. The results strongly suggest that the view that electron and hole transport and recombination occurs primarily on the host, followed by energy transfer to the guest, is not correct, but rather substantial numbers of charges reside and recombine on the guest.

As the voltage is increased, the trap depth when hopping in the direction of the electric field is effectively reduced, allowing faster escape of charges and reducing the depth of the minima seen in Figure 4.2. As indicated by the difference between the electron and hole mobility graphs, a flatter curve is seen for the electrons due to the shallower trapping depth on guest sites. However, a trapping depth that is too small may result in a larger portion of excitons forming on the host molecules, therefore reducing the probability that they diffuse to a guest molecule where they can undergo radiative triplet decay.

In a very low concentration system (<2 wt%), guest molecules are typically isolated and so each $Ir(ppy)_3$ molecule can act as a trap, thereby reducing mobility. However, as the concentration increases, the guest molecules can begin to form clusters, providing small pathways along which charges can travel, effectively reducing the overall number of traps in the system compared to the number of guest molecules. A further increase in concentration results in the formation of percolation pathways, which allow charges to travel across significant portions of the device via guest-to-guest hopping. Since the mobility in the guest and host was equal in this system, the minimum mobility at 10 wt% is therefore reflective of the point at which the maximum number of traps are present.

To understand guest-to-guest hopping, we define a “cluster” as a group of guest

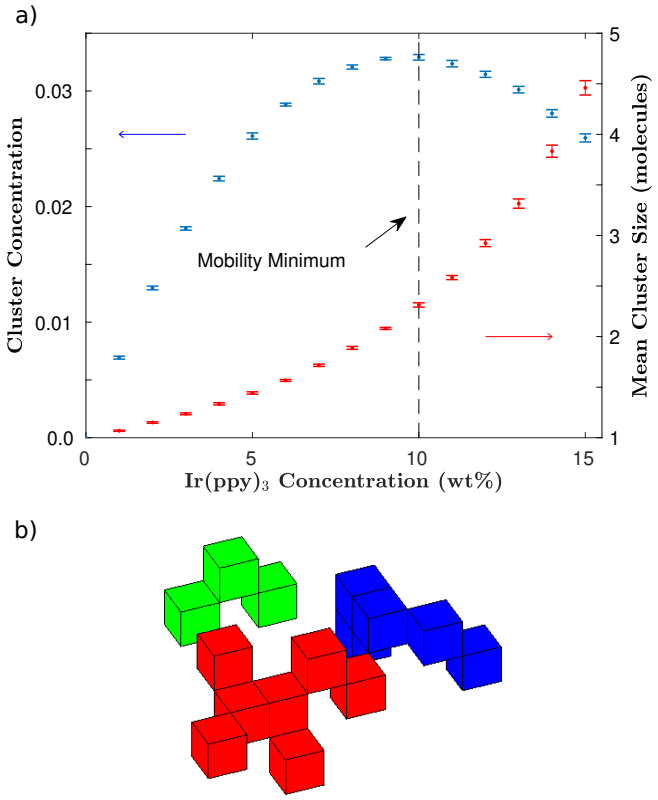

Figure 4.5: (a) Average concentration and size of guest clusters as a function of guest concentration, where a cluster is defined as a group of guest sites connected by at most second nearest neighbor hops. 10 Morphology realizations were used for each concentration.
(b) Example of 3 separate clusters.

molecules that are connected by at most second nearest neighbor hops. This level of connectedness was chosen based on the observation that >99.9% of hops were within a distance of at most the second nearest neighbor. Figure 4.5 shows an analysis of the number of clusters of guest molecules in comparison with the location of the mobility minima observed in Figure 4.2. These results show a striking relationship where the mobility minimum occurs at the same concentration as where the number of clusters is maximized. This suggests that de-trapping from guest clusters is the rate limiting step in the bulk charge transport for guest concentrations used in the highest efficiency OLEDs. It is expected that this mobility minima will shift slightly toward lower guest concentration under a more realistic morphology where clustering is more prevalent [118].

Although exact exciton dynamics were not studied here, formation events were tracked based on when an electron hopped to a site containing a hole or vice versa. Figure 4.6 shows the distribution of exciton formation events in relation to their distance to the nearest $Ir(ppy)_3$ molecule. It can be seen that even at 2 wt%, a significant portion of singlet and triplet excitons form directly on the guest molecules. Singlet excitons on $Ir(ppy)_3$ molecules are able to rapidly cross into the triplet state, from which they can radiatively recombine due to strong spin-orbit coupling. However, ex-

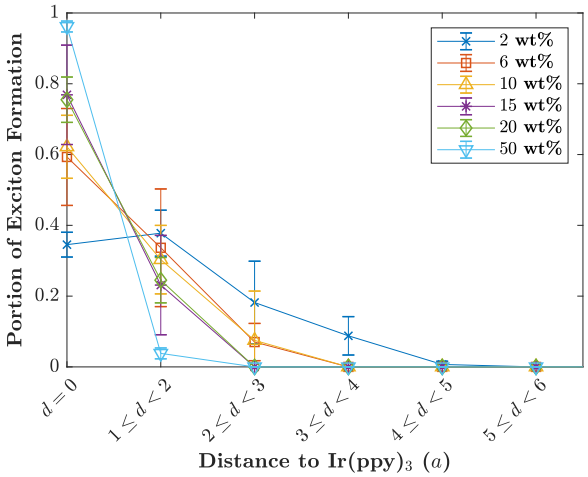

Figure 4.6: Portion of excitons that form at a distance d to the nearest $Ir(ppy)_3$ molecule, where d is measured in lattice units ($a = 0.8935$ nm).

citons that form in the host must first be transferred to a guest molecule before they can contribute to phosphorescence. Energy transfer from the host to the guest can occur either through Förster or Dexter mechanisms, although Förster transfer between CBP and $Ir(ppy)_3$ has a relatively low probability due to the small overlap of the CBP emission and $Ir(ppy)_3$ absorption spectra, and the low optical density of $Ir(ppy)_3$ at the guest concentrations used [118]. Due to the short-range nature of Dexter energy transfer, excitons are likely only able to contribute to phosphorescence if the $Ir(ppy)_3$ guest is within the exciton diffusion length when the exciton is formed on a host CBP.

It has been experimentally observed that the optimum concentration of $Ir(ppy)_3$ in CBP for OLEDs is approximately 6 wt% [159]. At this concentration, approximately 60% of the excitons are formed on the guest molecules, with the remainder forming within 3 lattice units (~ 2.7 nm), which is sufficiently close to enable Dexter energy transfer from the host to the guest [161]. These results highlight the importance of charge trapping directly on the guest for high efficiency $Ir(ppy)_3$:CBP OLEDs. It is likely that these results are applicable to other guest-host systems with similar transport characteristics and concentrations. Given the exponential increase in cluster size shown in Figure 4.5, it is apparent that the optimal concentration must be balanced between one that is high enough for any excitons on formed on the host to be sufficiently close to guest molecules, while being low enough to minimize triplet-triplet and triplet-charge quenching between connected guest molecules.

4.4 Summary

Kinetic Monte-Carlo simulations were used to study charge transport in $Ir(ppy)_3$:CBP OLEDs. Varying the concentration of guest molecules revealed a distinct mobility minimum at approximately 10 wt% $Ir(ppy)_3$, which was due to the formation of connected

clusters that created effective guest molecule-based trap sites. The depth of the minima was shown to arise from the difference between the host and guest HOMO levels for holes, or LUMO levels for electrons, as well as the electric field. Furthermore, these results indicate that a large portion of excitons are formed directly on the $Ir(ppy)_3$ molecules, even at low concentrations, with almost 100% of exciton formation events being within 3 lattice units of the nearest guest molecule at a concentration as low as 6 wt% $Ir(ppy)_3$. Under the more realistic morphology observed by Tonnelé *et al.* [118], the mobility minimum is expected to shift slightly towards lower guest concentrations due to the increased clustering of the guest molecules. Note, however, that since the publication of this chapter, the same trend in mobility was observed by Gao *et al.* in a similar small molecule guest-host phosphorescent OLED blend [69].

5

Effects of Guest-Host Energy Level Alignment on Charge Transport

This chapter contains material that was published in the journal article:

[2] Stephen Sanderson, Bronson Philippa, George Vamvounis, Paul L. Burn, and Ronald D. White. Elucidating the effects of guest-host energy level alignment on charge transport in phosphorescent OLEDs. *Applied Physics Letters*, **115**, 263301 (2019). doi:10.1063/1.5131680

The simulation work described in this chapter is my own. The presented interpretation and analysis of the results was initially performed by me with advice from the listed coauthors, and refined with their further input.

5.1 Introduction

The correct choice of guest and host molecules in the light-emitting layer is essential for developing high performance phosphorescent OLEDs. To achieve high efficiency, the guest and host must be correctly paired, and have optoelectronic properties compatible with the surrounding transport layers [60, 162–164]. The general guidelines for this are to choose a host with a triplet energy sufficiently higher than that of the guest to promote host to guest exciton transfer (and avoid back transfer), and for the blend to have high and balanced charge mobility to achieve a wide recombination zone and reduced efficiency roll-off at high current density [8, 41, 43, 63, 65–67, 165, 166]. In addition, the host should also have energy levels that are well matched to the charge transport layers for a low driving voltage, and good thermal and morphological stability for prolonged device lifetime [63, 66, 67, 165, 166].

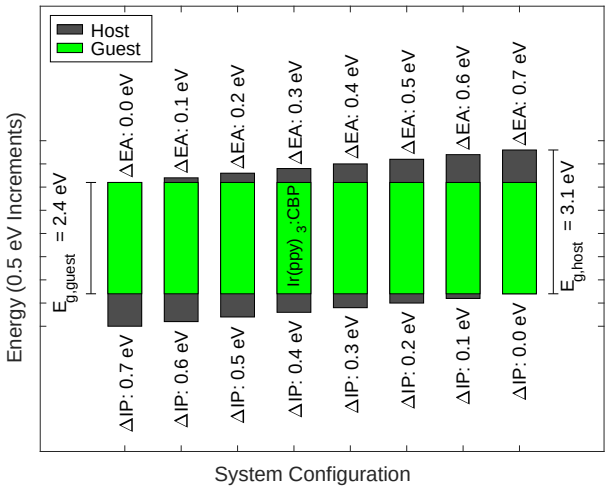

Figure 5.1: Energy level configurations with electron affinity difference (ΔEA), ionization potential difference (ΔIP), and energy gaps (E_g) labelled. The indicated configuration is equivalent to an $Ir(ppy)_3$:CBP blend, and was used for data normalisation where appropriate. A guest concentration of 4.5 mol% (equivalent to 6 wt.% $Ir(ppy)_3$in CBP) was used in all cases.

Despite these general guidelines, there is still some uncertainty involved in choosing the optimal guest-host pairing. In particular, while host materials are generally chosen with an electron affinity (EA) and ionization potential (IP) smaller and larger than that of the guest respectively [166,167], and the exact differences ($\Delta EA = EA_{host} - EA_{guest}$ and $\Delta IP = IP_{guest} - IP_{host}$) have been shown to be important for efficient recombination processes [168], the impact of ΔEA and ΔIP on charge transport in the guest-host blend remains somewhat unclear [68].

In this chapter, kinetic Monte-Carlo (KMC) simulations are utilised to investigate the effects of ΔEA and ΔIP on charge transport in a light-emitting layer blend. Eight different ΔEA and ΔIP combinations were investigated with the variations in guest-host energy level alignment shown in Figure 5.1. It should be noted that the energy gaps (taken as $E_g = EA - IP$) of the guest and host were held constant in all cases. The blend used as the standard for the analysis was parameterized to be equivalent to a 6 wt% blend of *fac*-tris(2-phenylpyridine)iridium(III) ($Ir(ppy)_3$) in 4,4'-bis(*N*-carbazolyl)biphenyl (CBP) - a green-emitting active layer with relatively high performance. In addition to the energy gaps, all the other system parameters were held constant while the host energy levels were adjusted to observe the resulting effects on charge transport. We note that it has been demonstrated experimentally that the energy levels of carbazole derivative hosts can be modified while maintaining a similar energy gap [164]. However, the impact this has on charge transport in the active layer has not been reported.

5.2 Model Structure

Charge transport was simulated in a simple diode geometry with the active layer sandwiched directly between the two electrodes, and with a constant 7 V bias applied. As in the previous chapter, charge hopping rates were calculated using the Miller-Abrahams formalism and electrostatic interactions were handled with the finite difference method described in Section 3.2.3. The site energy for electrons (holes) on both host and guest sites was sampled from a Gaussian distribution [23] centered around the EA (IP) of the site, with a standard deviation of 162 meV - the energetic disorder of CBP [155]. This produces an overall density of states (DoS) that is a linear combination (weighted by the guest:host molar ratio) of two Gaussian distributions with equal widths, and with mean values aligned to the EA (IP) of the guest and host.

As described previously, an electron hop to the site of a hole (or vice versa) was assumed to be always energetically favourable, and to result in an exciton which was immediately removed from the system for simplicity. The base electron and hole hopping rates were calculated to give simulated neat mobility values of approximately 3×10^{-4} cm^2/Vs and 2×10^{-3} cm^2/Vs, respectively, which are equivalent to those reported for neat CBP films [157]. In this analysis, we set the guest and host to have similar electron and hole mobilities, and a constant energetic disorder was assumed. Thus, ν_0 was treated as constant throughout the device. Using this approach, the rates of equidistant hops downwards in energy appear identical, regardless of the source and destination molecules (i.e., independent of whether the source or destination molecule was a host or guest). Charge hops were considered up to a distance of 3 lattice units (~2.7 nm) in each direction [23], resulting in a 7x7x7 lattice unit cube of potential hop destinations centered around the charge.

In all systems, the electrode Fermi level was assumed to be equal to the EA (IP) of the host when considering electrons (holes), so that equivalent contact conditions were maintained despite the varying energy levels. Injection rates were calculated as described previously to approximate Ohmic contacts.

The film morphology was generated by randomly assigning sites as either a guest or host with a probability defined by the desired concentration. A guest concentration of 4.5 mol% was used in all cases, which corresponds to 6 wt% Ir(ppy)$_3$ in CBP (the optimal ratio for that blend [159]). A lattice constant (a) of 0.8935 nm was used (see Chapter 4), and the systems were kept at a constant length of 71.5 nm between electrodes. Periodic boundaries were assumed in the directions parallel to the electrodes, with the periodic dimensions both being equal to 53.6 nm to avoid finite size effects [156]. Three different film morphology realizations were generated in total, and results for each system configuration were taken as the average over these three realizations, with error bars corresponding to the standard deviation. Measurements of individual realizations were taken as the time-averaged value at steady state, with the steady state being identified by constant current and carrier density.

A starting point of ΔEA = 0.3 eV and ΔIP = 0.4 eV was used, corresponding to

Property	Value	Ref.
Electron hop rate (ν_0^e)	1×10^{12} s^{-1}	note 1
Hole hop rate (ν_0^h)	2×10^{14} s^{-1}	note 1
Energetic disorder (σ)	162 meV	[155]
Relative permittivity (ε_r)	2	note 1
Lattice constant (a)	0.8935 nm	note 1
Normalized Inverse Localization Radius ($2\gamma a$)	10	[23]
Temperature (T)	298 K	
Applied voltage (V)	7 V	
Device thickness (L_x)	71.5 nm	

Table 5.1: Fixed simulation parameters. [1)]See Chapter 4.

the energy offsets between the experimentally measured EAs and IPs of CBP (EA: -2.6 eV, IP: -5.7 eV) and Ir(ppy)$_3$ (EA: -2.9 eV, IP: -5.3 eV) [158]. From there, the host energy levels were varied while maintaining a constant energy gap ($E_g = 3.1$ eV) to cover the range of possibilities from $EA_{host} = EA_{guest}$ to $IP_{host} = IP_{guest}$. Values outside of this range were not considered as they are expected to reduce the likelihood of exciton formation by charge trapping on the guest, and are unlikely to provide good device characteristics. A list of relevant fixed system parameters is provided in Table 5.1.

The steady state current density was calculated from the time-averaged device current at steady state, where the device current is the sum of the conduction current density (j_C) and displacement current density (j_D) as described in Section 3.4.1.

5.3 Results

Figure 5.2 shows the steady state current for each ΔEA/ΔIP combination, normalized to that of the simulated values of the configuration equivalent to an Ir(ppy)$_3$:CBP blend used in a device. Interestingly, there is an increase in the current density of almost 2 orders of magnitude under deep trapping of the electrons on the guest (when ΔEA is at a maximum), while the same conditions for holes produce little to no increase. To understand this behavior the charge mobility was plotted as a function of energy level alignment. Figure 5.3 shows clearly that holes have a significantly higher peak mobility than electrons, as would be expected based on their relative hopping rates, and hence reduced guest-trapping of holes has a greater effect on current density than reduced electron guest-trapping. It was also observed that under deep electron trapping on the

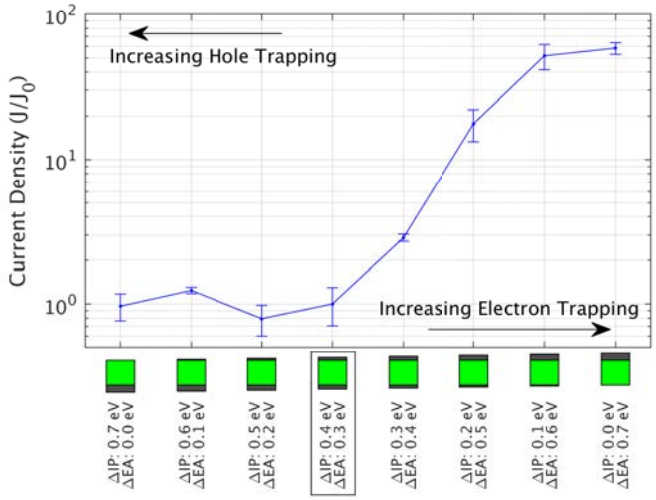

Figure 5.2: Simulated steady state injection current density scaled to J_0 - the simulated current density of 6 wt.% $Ir(ppy)_3$:CBP (outlined). The current density shows high sensitivity to energy level alignment, and significant enhancement in the case of shallow trapping of the faster carrier.

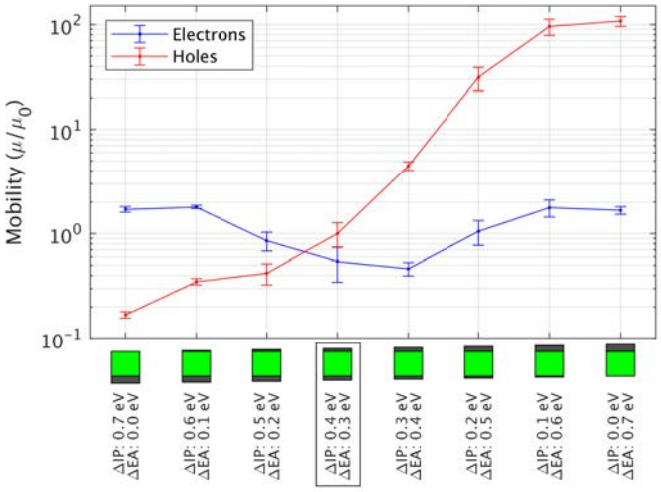

Figure 5.3: Electron and hole mobilities scaled to μ_0 - the mobility of holes in 6 wt% $Ir(ppy)_3$:CBP (outlined). Note the behaviour of the electron mobility, which has similar values under shallow and deep trapping configurations.

guest, the electron mobility rises again to near its peak value rather than being further suppressed as was the case for holes.

To investigate the origin of this electron mobility increase under deep trapping on the guest, the fraction of the lifetime a carrier spent on a guest molecule was analysed under each configuration (see Figure 5.4). It is immediately apparent that under deep trapping conditions on the guest, electrons spend a smaller fraction of their lifetime on the guest compared to holes. An explanation for the shorter electron lifetime on the guest is that the electrons recombine with holes before they can fully thermalise.

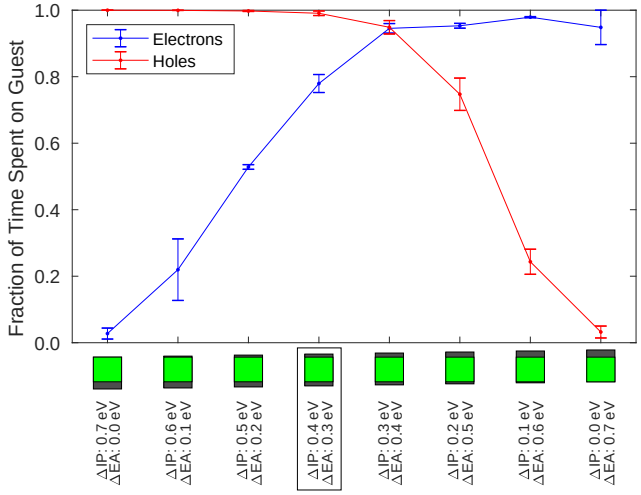

Figure 5.4: Fraction of charge lifetime spent on a guest molecule. The reduced electron fraction under deep electron trapping on the guest indicates that electrons (the slower carrier) are likely to recombine before they can fully thermalise.

That is, when the electrons are deeply trapped on the guest, the holes are relatively free to move and are able to quickly find and recombine with an electron. Hence the observed electron mobility is related to the non-trapped and rapidly removed electrons, resulting in a mobility closer to that of the neat host.

To verify this explanation, the average energy level of electrons and holes in each system was plotted, and compared to the energetic DoS. Figure 5.5 shows that electrons are indeed less thermalised than holes under the same trapping conditions, supporting the idea that the higher than expected electron mobility is due to relatively fast recombination with holes, and hence removal of trapped electrons from the system. It is interesting to observe that hole thermalisation also decreases with increased trapping on the guest, likely for the same reason as electrons. Additionally, it was noted that the crossing point of the two curves aligns very well with the crossing point of the mobility curves, further indicating the relationship between mobility balance and charge thermalisation.

5.4 Summary

In summary, while the guest:host ratio plays an important role in controlling charge transport and photophysical properties of the light-emitting layer, the results from the KMC simulations show that charge carrier mobility balance is also highly sensitive to the guest-host energy level alignment for a given guest concentration. Importantly we show that even if the neat film electron and hole mobilities are moderately imbalanced, a device with balanced mobility and optimized photoluminescence quantum yield (PLQY) could still be constructed if the guest-host energy level alignment is properly selected (or engineered). Under optimized energy level alignment to give

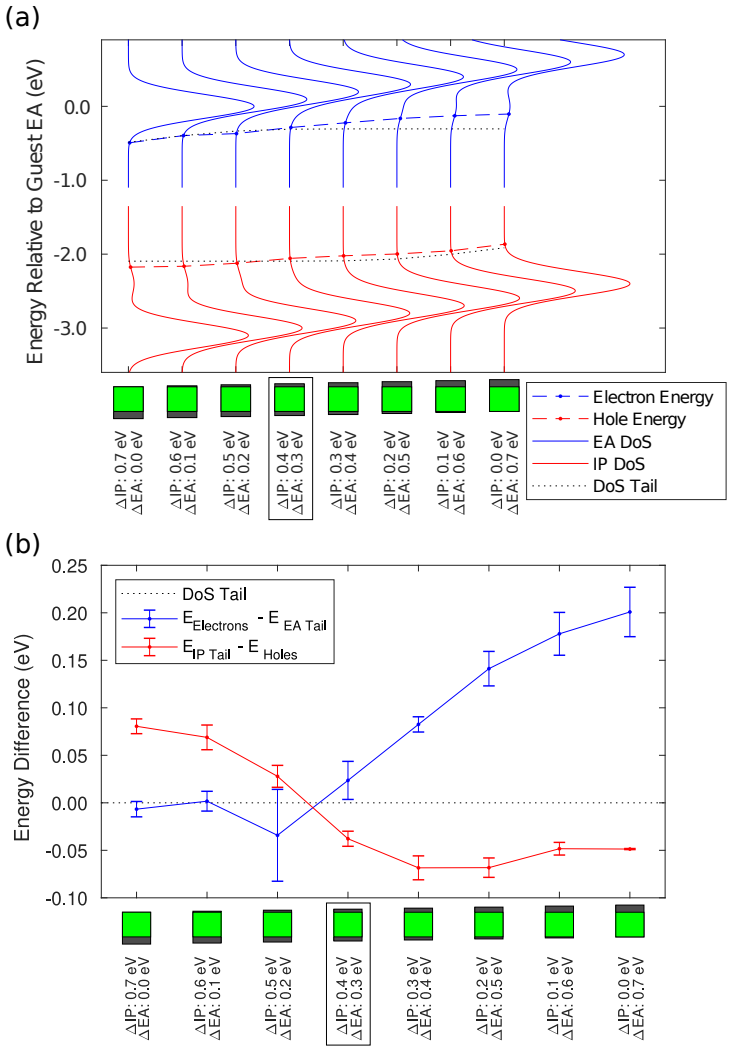

Figure 5.5: (a) Mean charge energy relative to the system density of states. Dotted lines indicate the tail of the DoS, defined as the point where the cumulative distribution function reaches 0.13% (equivalent to the -3σ point of a standard normal distribution). (b) Difference between mean charge energy and the DoS tail, clearly showing that electrons are less thermalised than holes under comparable energy level alignment configurations.

balanced electron and hole mobilities, the current density in such a device would be limited by the mobility of the slower carrier.

It was also observed that the mobility of the slower carrier was relatively insensitive to the depth of trapping on the guest, particularly in the cases of highly asymmetrical energy level alignment. The mobility balance sensitivity is therefore primarily due to the sensitivity to the trapping depth of the faster carrier. It is hence apparent that when designing the light-emitting blend layer of a phosphorescent OLED, attention should be paid to choosing a host with higher triplet energy than the guest, a guest:host ratio to maximize the film PLQY and charge transport, and from this work, the IPs and EAs of the guest and host to balance the charge mobility.

6

Exciton Dynamics in Guest-Host OLEDs

This chapter contains material that was published in the following journal article, but is not yet published at the time of writing:

[4] Stephen Sanderson, George Vamvounis, Alan E. Mark, Paul L. Burn, Ronald D. White, and Bronson Philippa. Unraveling Exciton Processes in Ir(ppy)3:CBP OLED Films Upon Photoexcitation. *The Journal of Chemical Physics*, 164101 (2021). doi:10.1063/5.0044177

I performed the molecular dynamics simulations described in this chapter using a model developed by the group of Alan Mark, and assistance in configuring and debugging initial test runs with that model was provided by Dr. Thomas Lee, Dr. Martin Stroet, and Audrey Sanzogni. All other work described in this chapter is my own.

6.1 Introduction

An archetypal phosphorescent OLED blend that has a reported high efficiency is composed of *fac*-tris(2-phenylpyridine)iridium(III) [Ir(ppy)$_3$] as the guest and 4,4'-bis(*N*-carbazolyl)biphenyl (CBP) as the host. This blend has been studied extensively to determine properties such as the optimal guest concentration [159], exciton lifetimes and diffusion mechanisms [51, 54, 142, 148, 169, 170], and loss processes such as triplet-triplet annihilation and non-radiative triplet decay [141, 171–173]. Ir(ppy)$_3$:CBP blends have also been subject to detailed computational analysis, with molecular dynamics (MD) simulations showing that guest molecules tend to form clusters within the blend,

rather than being randomly distributed [118], and kinetic Monte-Carlo (KMC) simulations (shown in Chapter 4) revealing that charge diffusion is primarily guest-based, with guest clusters acting as multi-molecule traps. However, questions remain regarding details of the exciton diffusion process, particularly concerning the degree of triplet guest-confinement.

Here, we investigate exciton diffusion and exciton-exciton interactions in $Ir(ppy)_3$:CBP blend films using KMC techniques to simulate photoexcitation experiments. The efficiency of these simulations has enabled a wide parameter space to be sampled while maintaining good statistics. The sensitivity of the calculations to the details of the film morphology generation method were also investigated by comparing results of films at 6 wt% [159] guest concentration obtained using a randomized cubic lattice structure, with those obtained using morphologies generated with MD simulations in which the process of vacuum deposition has been modelled explicitly in atomic detail.

6.2 Methodology

Exciton-only KMC simulations were performed with 12 different initial densities of randomly generated singlets between 3×10^{16} cm^{-3} and 3×10^{19} cm^{-3} to emulate short laser pulses of varying intensity and give realistic initial excitation densities [174]. Singlet generation was treated as instantaneous at the beginning of the simulation. A uniform generation profile was used, meaning all molecules in the system had an equal probability of singlet generation. If a chosen generation site was already occupied, that singlet was discarded and replaced. We note that only excitons and exciton-exciton (and not exciton-polaron) interactions were considered in this model to enable efficient simulations that do not require computationally expensive evaluation of electrostatic interactions, thereby allowing a wide parameter space to be sampled.

An overview of the modelled processes is provided in Figure 6.1. Upon photoexcitation of the blend, singlets were allowed to diffuse via host-host and host-guest Förster transfer events [148]. Once a singlet was on a guest molecule, it could cross into the triplet state via ISC, and it was assumed based on the fast ISC rate of $Ir(ppy)_3$ [171] that the singlet did not diffuse any further. That is, guest-guest and guest-host singlet transfers were not considered in the model. Competing with this singlet to triplet conversion process were radiative and non-radiative singlet decay events on the host. These decay processes were treated as having a fixed rate, and were only considered for singlets on host molecules (again due to the fast ISC rate once on the guest).

Once a triplet formed on a guest, it was allowed to diffuse via both Dexter and Förster transfer events. Triplet Förster transfer events were considered for guest-guest transfers only, as Förster transfer from the guest to the host is unlikely given the relative triplet energies. In addition, the weak spin-orbit coupling of CBP [175] means that triplet formation on the host by ISC has a low probability. Triplet Dexter transfer events were allowed for guest-guest, guest-host, host-host and host-guest transfers. The

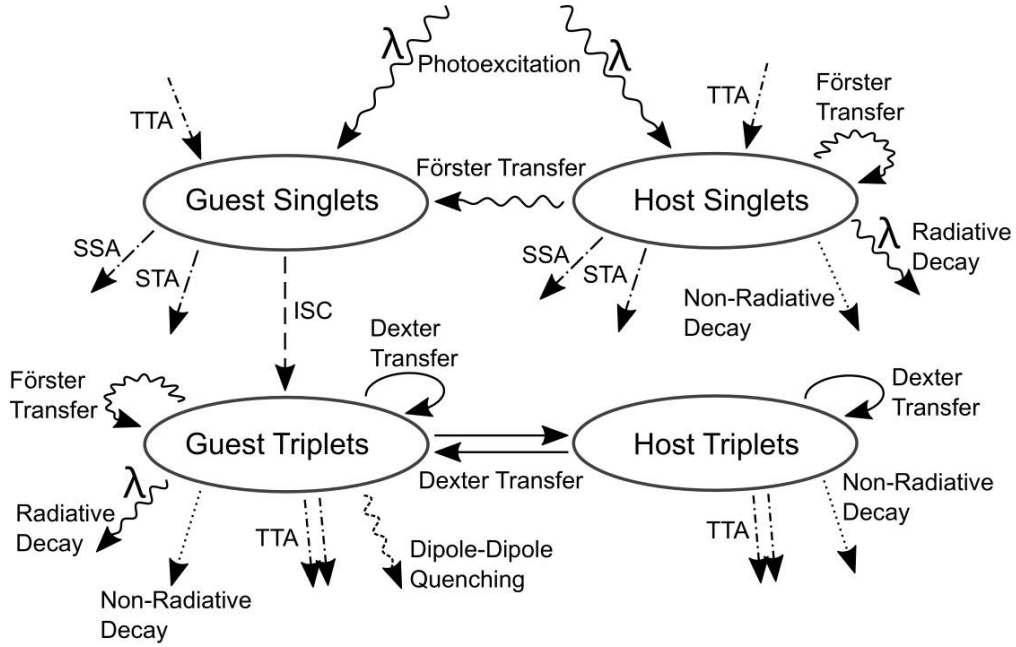

Figure 6.1: Flowchart of the modelled processes, and how they relate to the populations of singlets and triplets on guest and host molecules, where TTA is triplet-triplet annihilation, STA is singlet-triplet annihilation, SSA is singlet-singlet annihilation, and ISC is intersystem crossing.

radiative and non-radiative triplet decay rates were fixed, with values dependent on the molecule type.

In addition, a triplet loss process with r^{-6} distance dependence that is independent on the triplet density has been observed when $Ir(ppy)_3$ molecules are in close proximity [141, 171, 173, 176]. While the exact physical description of this process is unclear, it has previously been attributed to the formation of a weakly emissive excimer state [171], repeated intermolecular energy transfer (emission and absorption between chromophore pairs) leading to deactivation of the excited state [173, 176], and to excitation transfer to a quencher [141]. In this work, we model this triplet loss process as a dipole-dipole interaction [49] with a thermal activation energy of 170 meV. This value was chosen to fit the concentration dependent photoluminescence efficiency of $Ir(ppy)_3$:CBP blends as presented by Kawamura *et al.* [177] (see Figure 6.2), and is reasonably close to the value of 121 meV reported elsewhere [172, 173]. The event rates for this process were parameterized in the same manner as guest-guest Förster transfer events (see Eqn. 3.22), and were calculated for all neighbouring guest molecules within a 5 nm radius. Triplets which undergo this transfer were removed from the system immediately for simplicity.

To differentiate from other concentration quenching processes, we will refer to this process as dipole-dipole quenching. Note that while we calculated this dipole-dipole quenching rate in terms of an activation energy, it could instead, without any significant change to the rate calculation, be interpreted as a probability that a given Förster transfer event results in deactivation (loss) of that triplet. Note also that although the

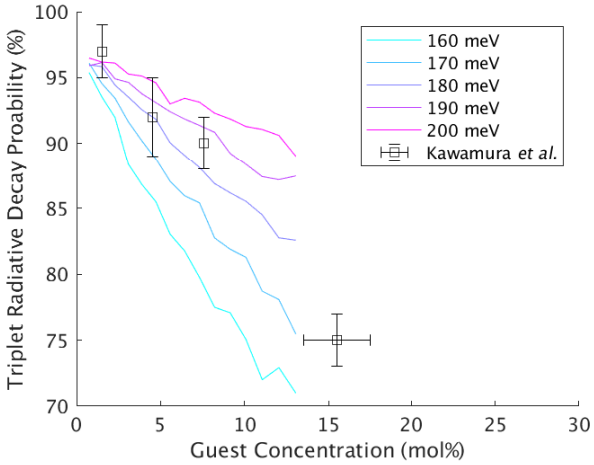

Figure 6.2: Comparison of the triplet radiative decay probability for various dipole-dipole quenching activation energies against the data presented by Kawamura *et al.* [177]. The KMC data presented in this plot was averaged over 5 different morphologies, with 1000 randomly generated singlets in each case. Excitons were treated as non-interacting to simulate an infinitely low excitation density. Note that we assume no dipole-dipole quenching occurred in the measurement of the radiative decay to non-radiative decay ratio, and this assumption could result in an underestimation of the relative fraction of radiative decay. Hence, an activation energy of 170 meV was used in this work.

occupation state of the neighbouring guest molecule was not considered in these rates for simplicity, this has no meaningful effect on the overall probability of radiative triplet decay, as both dipole-dipole quenching and triplet-triplet annihilation were assumed to result in the loss of one triplet.

To explore the effect of guest concentration, the simulations were repeated for all integer guest concentrations between 1 wt% and 15 wt%. The morphologies used for these simulations were based on a cubic lattice with randomly distributed emitter molecules. To validate the use of this cubic lattice approximation, the KMC simulations were also performed using the morphology of a blend containing 6 wt% guest, generated by simulating the process of vacuum deposition using molecular dynamics techniques [69, 118, 120].

To ensure sufficient statistical accuracy, the results for each concentration were averaged over five cubic lattice morphology realizations, with at least 20 repeats per realization per data point, and up to 200 repeats at low initial excitation density. To obtain converged results at extremely low exciton densities where less than one singlet would be present in the periodic volume on average, simulations were performed in which excitons were treated as non-interacting. In this case, 1000 singlets were generated, and 20 repeat simulations were used per morphology realization. Note that in the results, the lowest initial excitation density plotted corresponds to this non-interacting case. For the MD-generated morphologies, three realizations were used with at least 100 repeats per realization. For a clearer comparison between results from the MD-generated morphology and those from cubic lattice morphology, up to 2000 repeats per realization were used at low exciton densities in the 6 wt% guest

blends.

6.2.1 Kinetic Monte-Carlo Simulations

The basic details of the KMC model used for these simulations have been described in Chapter 3. To ensure that all exciton transfers with a reasonable probability were captured, Dexter transfer events were allowed for all neighbours with a center of mass (CoM) distance less than 3 nm, and Förster transfers were allowed within a radius of 5 nm. A Dexter or Förster transfer of a singlet or triplet to a destination site that was already occupied (regardless of whether that site was a guest or a host) resulted in an exciton-exciton interaction as described by Equation 2.1. All triplet-triplet interactions were treated as resulting in a singlet for simplicity [54, 180], noting that this singlet will quickly cross back to the triplet state if it is on a guest molecule. To simplify the tracking of diffusion lengths and lifetimes, the quenched exciton was assumed to be the one undergoing the transfer, except in the case of singlet-triplet annihilation (STA) where the singlet was always quenched.

Dexter transfers were considered for triplet excitons only [141, 148]. The rates were calculated using the Miller-Abrahams equation as described in Section 3.2.4. Note that the Miller-Abrahams prefactor for transfers between different molecular species was taken as the geometric mean, $\sqrt{\nu_0^{(i)}\nu_0^{(j)}}$, to allow potential guest-host and host-guest triplet Dexter transfers [7, 131]. However, guest to host Dexter transfers are significantly less likely due to the 0.2 eV barrier presented by the difference in triplet energies. Förster transfer event rates were calculated as described in Section 3.2.4. The energetic disorder of the singlet and triplet states was assumed to be Gaussian in nature [54, 131, 181].

A summary of the constants used in the KMC simulations is provided in Table 6.1.

6.2.2 Morphology Generation

Cubic Lattice

Simulation boxes of $56 \times 56 \times 53$ molecular sites on a cubic lattice were generated with a lattice spacing of 0.89 nm (see Chapter 4) so as to represent a ~47 nm thick active layer with 50 nm periodic directions. Guest molecules were assigned randomly, with a probability based on the desired molecular concentration. The system was periodic in the x-y plane, with open boundaries in the z direction.

Vacuum Deposition

To generate a more physically realistic morphology for a 6 wt% guest concentration, MD simulations of the vacuum deposition process were performed using the method described previously [69, 118, 120]. Briefly, beginning with a graphene substrate, guest and host molecules were randomly chosen with random orientations, and inserted approximately 3 nm above the top of the film at random positions, ensuring that simultaneously inserted molecules were separated by at least 2 nm. Each atom of

Parameter	Symbol	Value	Ref.
Lattice Spacing	a	0.89 nm	note 1
Temperature	T	300 K	
Inverse Localization Radius	γ	1.65 nm^{-1}	[141], note 2
Förster Radius	$R_0^{(\text{S,host-host})}$	2.2 nm	[148]
	$R_0^{(\text{S,host-guest})}$	2.8 nm	[142]
	$R_0^{(\text{T,guest-guest})}$	2.1 nm	[51]
Dexter Transfer Prefactor	$\nu_0^{(\text{T,host})}$	5.5×10^6 s^{-1}	note 3
	$\nu_0^{(\text{T,guest})}$	1.08×10^{11} s^{-1}	[141]
Triplet Decay Rate	$\nu_{\text{radiative}}^{(\text{T,guest})}$	7.5×10^5 s^{-1}	[69, 170]
	$\nu_{\text{non-radiative}}^{(\text{T,guest})}$	2.3×10^4 s^{-1}	[170]
	$\nu_{\text{non-radiative}}^{(\text{T,host})}$	71.43 s^{-1}	[54]
Singlet Decay Rate	$\nu_{\text{radiative}}^{(\text{S,host})}$	1.2×10^9 s^{-1}	[142, 169]
	$\nu_{\text{non-radiative}}^{(\text{S,host})}$	8×10^8 s^{-1}	[142, 169]
Inter-System Crossing Rate	$\nu_{\text{ISC}}^{(\text{guest})}$	1×10^{13} s^{-1}	[171]
Triplet Energy	$E_{\text{T}}^{(\text{host})}$	2.6 eV	[145, 167, 178]
	$E_{\text{T}}^{(\text{guest})}$	2.4 eV	[145]
Singlet Energy	$E_{\text{S}}^{(\text{host})}$	3.1 eV	note 4
	$E_{\text{S}}^{(\text{guest})}$	2.6 eV	note 5
Energetic Disorder of Exciton States	σ	30 meV	[54], note 6

Table 6.1: Summary of simulation constants.
[1)]See Chapter 4.
[2)]For simplicity, the inverse localization radius for triplet excitons in CBP was assumed to be equal to that of $Ir(ppy)_3$.
[3)]Triplet Dexter transfer rates in CBP were chosen such that the average triplet diffusion length was 140 nm [54] in a neat, fully periodic, cubic lattice system.
[4)]The singlet energy of CBP was approximated as the HOMO-LUMO gap.
[5)]The S_1 energy of $Ir(ppy)_3$ has been calculated to be 0.2 eV above the T_1 energy [179].
[6)]Energetic disorder was assumed to be the same throughout the system for both singlets and triplets.

these molecules was assigned a random velocity sampled from a Boltzmann distribution so that the overall molecule would have a random angular momentum. The sign of the vertical component of each initial velocity was set such that the molecule would move towards the substrate. The system was then allowed to evolve in time until the molecules reached the surface of the film, at which point the insertion process was repeated until the desired film size was reached. The films were then allowed to equilibrate for 10 ns, and were analysed without a further annealing step.

The dimensions of the periodic simulation box in the x and y dimensions were 17.04 nm and 16.72 nm, respectively. CBP and $Ir(ppy)_3$ molecules were selected randomly in the appropriate ratio, and were deposited 8 at a time at 16 ps intervals onto a graphene substrate. The atoms in the substrate were assigned atom type "C" in the GROMOS 54A7 forcefield [182] and were harmonically restrained ($k_H = 2 \times 10^4$ kJ mol^{-1} nm^{-2}). The interaction parameters for $Ir(ppy)_3$ were identical to those used by Tonnelé *et al.* [118] and Gao *et al.* [69]. The interactions for CBP were assigned using the Automated Topology Builder (ATB) version 1.0 [183].

The simulations were performed using GROMACS 2018.3 with GPU acceleration [129], with a time step of 2 fs. Temperature was controlled at 300 K using a Berendsen thermostat with a 0.1 ps coupling time [118, 184]. The pair list for non-bonded interactions was updated every 20 fs, with a cut-off radius of 1.4 nm. Electrostatic interactions were truncated beyond a cut-off of 1.4 nm using a reaction field correction with a relative permittivity of 10 [118, 185]. Bond lengths were constrained to their equilibrium values using the LINCS algorithm [186]. To reduce high frequency oscillations and improve integration, the mass of the hydrogen atoms was increased by 3 amu, which was correspondingly subtracted from their bonded neighbours to maintain the correct molecular mass. Despite this, using an order parameter of 4 and 1 iteration for LINCS resulted in the development of a velocity gradient beyond 1,500 deposition steps (12,000 molecules). This was suppressed by increasing the number of iterations in LINCS to 2 after that point. A total of 20,000 molecules were deposited for a layer height of approximately 48 nm. The final layer was then replicated in the periodic directions for a total size of approximately $51 \times 51 \times 48$ nm^3 (180,000 molecules).

6.3 Results

6.3.1 Cubic Lattice

To gain a full picture of exciton behaviour upon photoexcitation, we begin by analysing the fate of singlet excitons that formed on the host molecules. Figure 6.3 shows the percentage of singlets that are able to transfer to a guest molecule and undergo intersystem crossing, as a function of the initial density of singlets and the wt% concentration of the guest. This indicates that at low exciton densities, the proportion of singlets generated in the host that are able to transfer to a guest molecule and cross into the triplet state is relatively insensitive to the guest concentration above

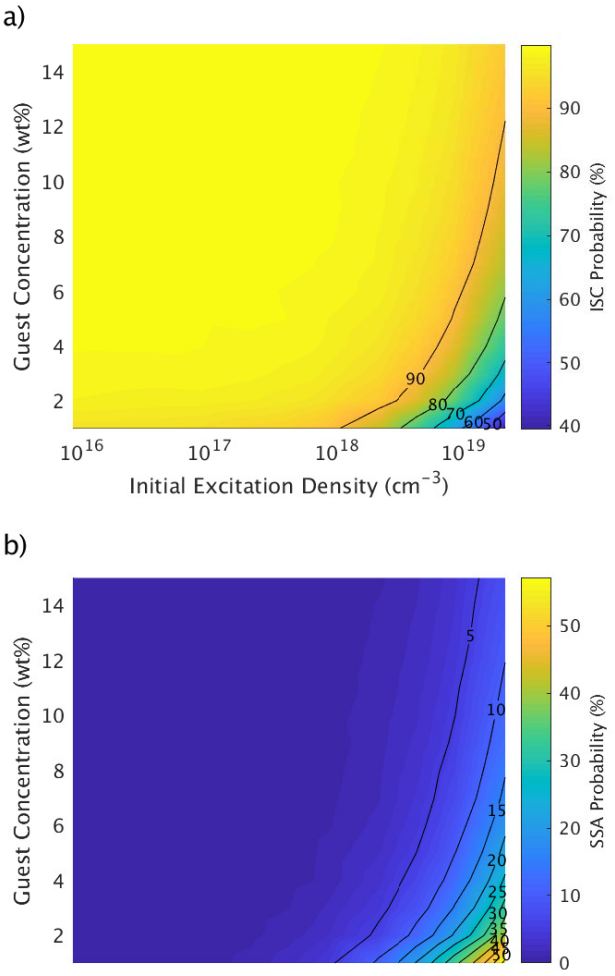

Figure 6.3: Probability that a singlet formed on a host molecule (a) reaches a guest molecule and undergoes inter-system crossing, or (b) is quenched by singlet-singlet annihilation (SSA).

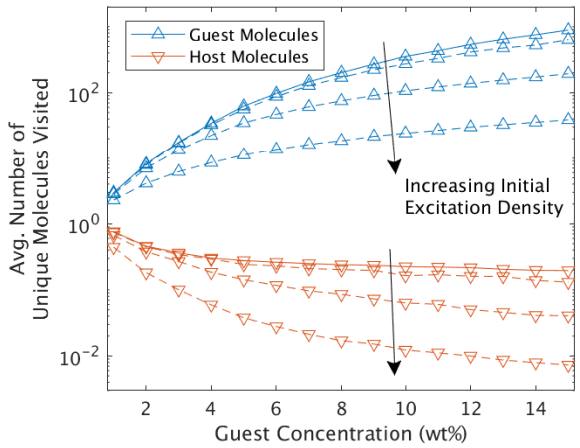

Figure 6.4: Average number of unique guest and host molecules visited per triplet. Solid lines represent the non-interacting case, and dashed lines represent initial excitation densities of 1.1×10^{17} cm^{-3}, 1.1×10^{18} cm^{-3}, and 1.1×10^{19} cm^{-3}. Note the logarithmic scale on the y axis, as guest to host triplet transfer is an unlikely process.

approximately 3 wt%. Note the reduction in triplet formation on the guest at higher initial excitation densities is almost entirely due to singlet-singlet annihilation on the host, which quenches as much as 55% of singlets at low guest concentration. Singlet decay accounts for the remainder of the loss, and is relatively insensitive to the initial excitation density below 1×10^{18} cm^{-3}. A maximum value of approximately 5% singlet loss due to singlet decay was observed at a guest concentration of 1 wt%, and the singlet decay probability was less sensitive to excitation density at higher guest concentrations where the process of a singlet transferring to the guest and crossing to the triplet state is faster (see Figure 6.5). Singlet-triplet quenching was extremely rare in these systems, and did not result in significant singlet loss.

It is also evident from Figure 6.3 that the onset of singlet-singlet annihilation on the host is dependent on the guest concentration. Higher guest concentrations allowed shorter diffusion distances to guest molecules, thereby reducing the likelihood of singlet-singlet interactions or singlet decay. Considering that results from Chapter 4 showed charge transport has occurs predominantly on or near the guest, with $> 75\%$ of excitons forming within 2 nm of a guest molecule even at 2 wt% guest concentration, the singlet diffusion length would be shorter than observed in these simulations where singlets were randomly generated, thus further reducing the probability that a singlet is lost through either singlet-singlet annihilation or radiative/non-radiative decay. Note that we define the diffusion length as the length of the displacement vector of the exciton undertaking a random walk, equal to the vector sum of its hops.

Once a triplet exciton is formed on the guest, it is able to diffuse via Dexter exchange, as well as guest-guest Förster transfer. As expected, due to the long triplet lifetime and low emission/absorption overlap of $Ir(ppy)_3$, it was found that triplet diffusion occurs predominantly via Dexter transfer, typically making up $> 97\%$ of triplet transfer events. In addition, as can be seen in Figure 6.4, which shows the average number of unique molecules visited by a triplet as a function of guest concentration for various initial excitation densities, triplet diffusion occurs almost exclusively on the guest even at low guest concentration, with the average guest-guest transfer distance increasing from approximately 1.3 nm at 15 wt% to approximately 2 nm at 1 wt%. This is an expected outcome given that the triplet energy of the host is 0.2 eV higher than that of the guest. Note, the reduction in the number of molecules visited as the exciton density increases is primarily due to increased triplet-triplet annihilation (TTA).

The observed guest-based triplet diffusion leads to TTA being the primary loss process for triplets in these exciton-only systems at higher exciton densities. This is illustrated in Figure 6.6, which shows the probabilities of radiative triplet decay and triplet loss due to TTA as a function of the initial excitation density and the concentration of the guest. Note, since TTA always results in the loss of one triplet and the conversion of the other into a singlet in this model, it accounts for almost all triplet loss at high exciton density. The resultant singlets formed on the guest are able to quickly cross back into the triplet state and again be subject to similar loss

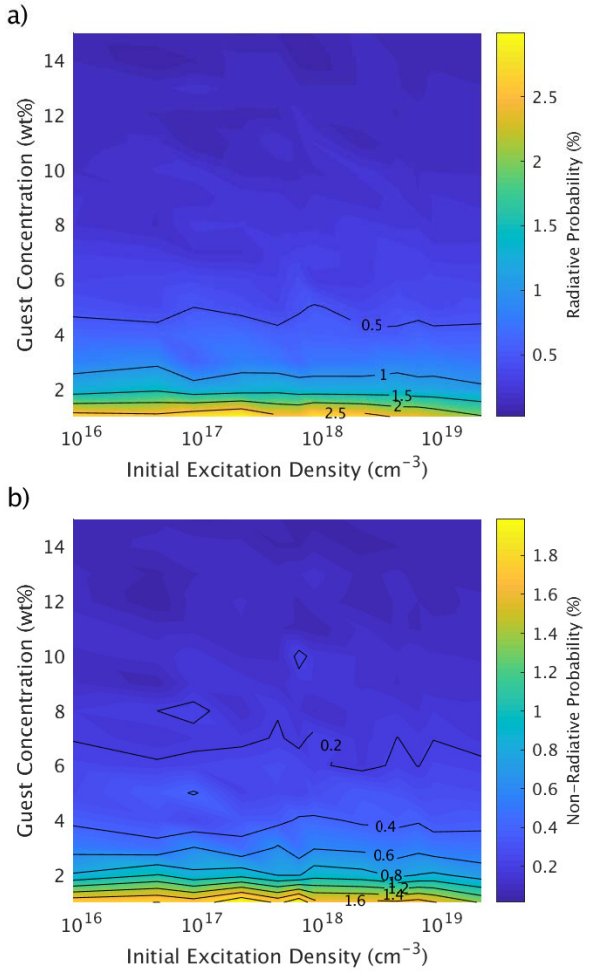

Figure 6.5: Probability of (a) radiative and (b) non-radiative singlet decay.

process statistics. Given the 10^2 difference in the average number of guest versus host molecules visited by a triplet evident in Figure 6.4, the probability of TTA occurring on the host is highly unlikely.

The other main triplet loss processes considered were non-radiative decay, and dipole-dipole quenching. The relative dependence of non-radiative decay on guest concentration and exciton density was identical to that of radiative decay (shown in Figure 6.6a). The probability of a triplet being lost to dipole-dipole quenching is shown in Figure 6.7, where it can be seen that while triplet loss via this process has a significant dependence on guest concentration at low exciton densities, it is largely independent on the guest concentration at higher exciton densities. This is because under high exciton density, the increase in TTA leads to a significant portion of triplets being lost on a time scale shorter than their natural decay time, thus suppressing the dipole-dipole quenching process. That is, at higher excitation densities, TTA is the dominant process for loss of the triplets.

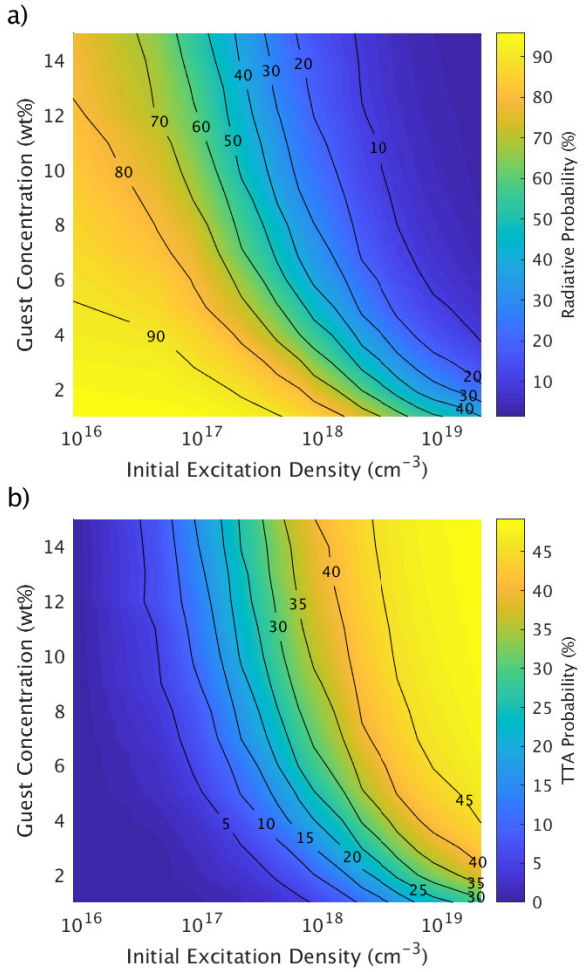

Figure 6.6: a) Probability that a triplet on a guest molecule decays radiatively. b) Probability that a triplet is quenched via triplet-triplet annihilation. Note, for every triplet quenched by TTA, another is converted to a singlet, which is able to quickly cross back to the triplet state and be subject to similar fate statistics.

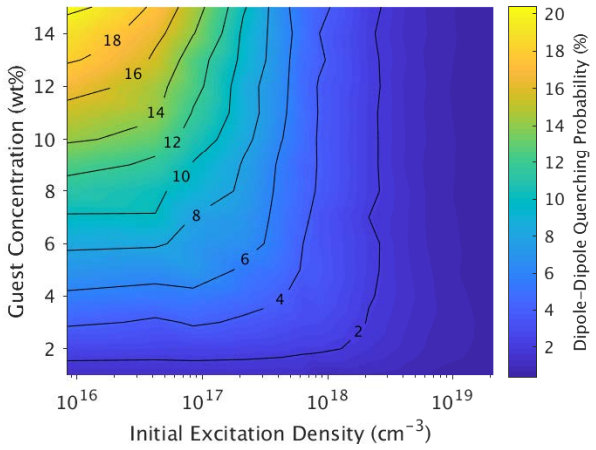

Figure 6.7: Probability that a triplet is lost to dipole-dipole quenching.

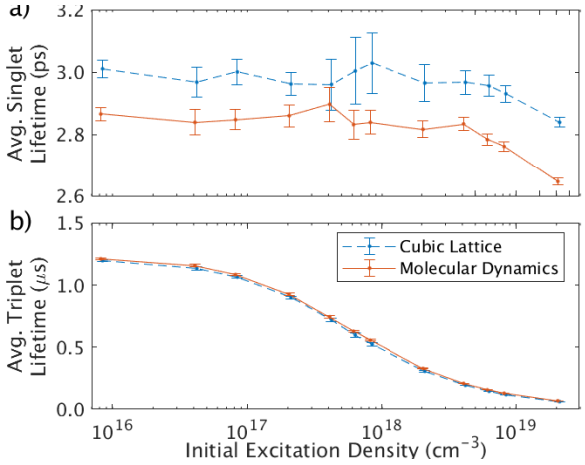

Figure 6.8: Comparison of the mean (a) singlet and (b) triplet lifetimes between cubic lattice and MD-based systems at a 6 wt% guest concentration. Error bars represent the standard deviation of the mean.

6.3.2 Effect of Morphology

A key question also addressed in this work was the extent to which differences in morphology might affect the outcome of the KMC exciton simulations. Specifically, whether the results obtained based on the commonly used practice of generating morphologies based on randomly assigning guest and host molecules to nodes on a cubic grid differ from those obtained using morphologies generated by simulating the process of vacuum deposition in atomic detail. The latter morphologies in which the guest is not randomly distributed have been extensively validated for the system in question, having been used to successfully predict a range of guest concentration dependent properties [118, 120]. In this work, we only considered a guest concentration of 6 wt% as this is the concentration that gives rise to the most efficient devices [159]. The main difference between the results obtained from the KMC simulations using the MD-based morphologies and those using morphologies based on a cubic lattice was that singlet excitons in the MD morphology were able to reach a guest molecule faster than in the cubic lattice morphology, as illustrated in Figure 6.8. This difference is explained by the molecular packing in the MD system.

Increased guest clustering in the MD morphology results in a slightly larger mean CoM to CoM distance from a CBP molecule to the nearest $Ir(ppy)_3$ molecule (1.42 nm compared to 1.24 nm in the cubic lattice systems). However the minimum value of this measurement was 0.45 nm in the MD system, since CBP molecules are able to pack closely with the emitter, which is approximately half the minimum distance possible with a cubic lattice spacing of 0.89 nm (as is required to give the correct molecular density). Thus, a singlet on a CBP molecule neighbouring an $Ir(ppy)_3$ molecule is more likely to transfer to that guest molecule in the MD system than in the cubic lattice system. This leads to fewer instances of singlets hopping away from a neighbouring guest, therefore slightly reducing the average time taken for a singlet to reach the guest, as well as the average singlet diffusion length.

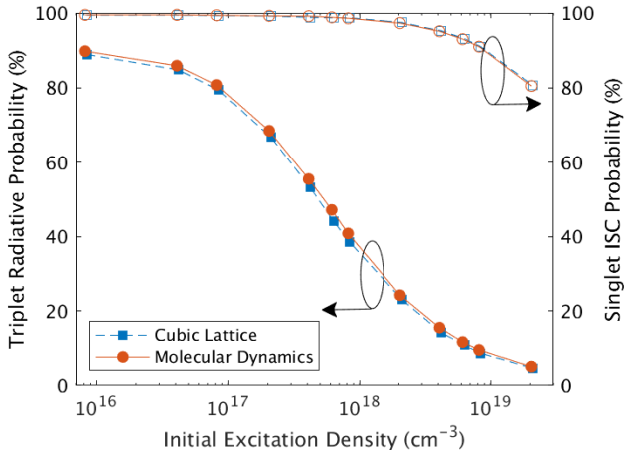

Figure 6.9: Probability that a singlet formed in the host crosses to the triplet state on a guest (open symbols), and that the resultant triplet is able to radiatively decay (filled symbols), compared between cubic lattice and MD-based systems at 6 wt% guest concentration. Error bars representing the standard deviation of the mean were smaller than the marker size, and were therefore omitted here. Plots comparing all triplet loss processes are provided in Figure 6.11. Arrows indicate the relevant y axis.

In addition, spatial disorder within the host present in the MD-based morphology means there are, in effect, clusters of closely-packed CBP molecules. Förster transfer of singlets between these closely packed CBP molecules is relatively fast, meaning a singlet may visit more unique CBP molecules before decaying, even though the diffusion length is slightly reduced. A comparison between the MD-based and cubic lattice morphologies of the singlet diffusion length and the number of unique host molecules visited in a 6 wt% blend is provided in Figure 6.10. It is important to note that the singlet diffusion length in either system is still significantly shorter than that of neat CBP, and that for both of the morphologies examined, plots of the singlet diffusion length and the number of unique host molecules visited as a function of initial excitation density have the same qualitative shape.

Interestingly, despite the observed differences and the potential limitations of the cubic lattice model, the proportion of singlet and triplet loss processes as a function of initial excitation density was essentially identical (within uncertainty) when the guest was at a concentration of 6 wt%, regardless of whether the cubic lattice or MD-based morphology was used. This is illustrated in Figure 6.9, which shows the probabilities of singlet ISC and radiative triplet decay. The exception to this was triplets at low initial excitation densities, where dipole-dipole quenching was slightly more prevalent in the cubic lattice system than the MD-based system (see Figure 6.11).

Importantly, triplet lifetimes were also nearly identical (Figure 6.8), and only minor differences were observed in the triplet diffusion length and the number of unique guest and host molecules visited per triplet (see Figures 6.12-6.14). This suggests that within the limits of the theoretical approximations commonly employed in KMC transport modelling, results using a cubic lattice model can capture the key features of triplet dynamics in real systems, at least at low guest concentrations where the extent of guest

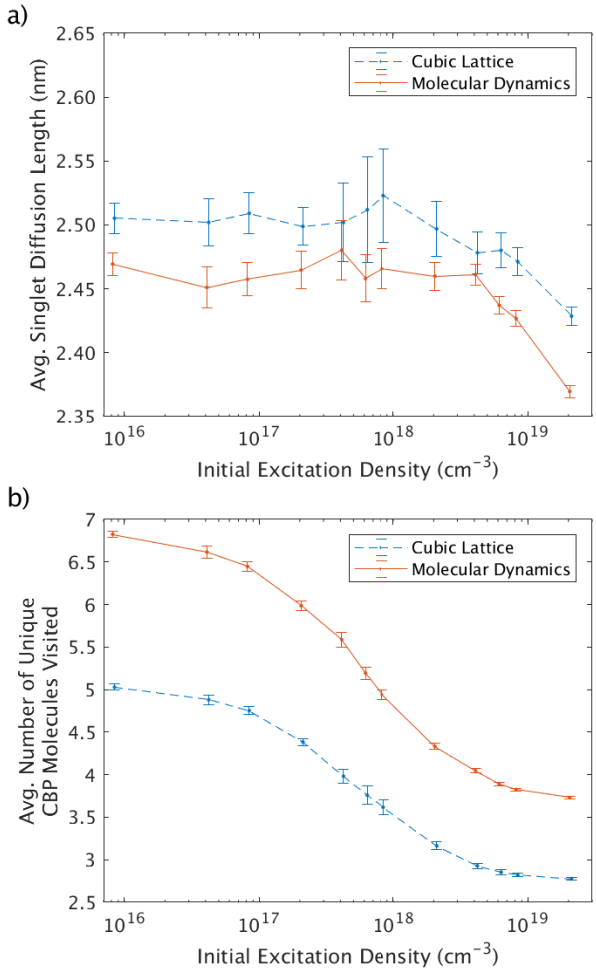

Figure 6.10: Comparison between cubic lattice and molecular dynamics-based morphologies at 6 wt% guest concentration for (a) diffusion length of singlets that formed in the host, and (b) the number of unique CBP molecules visited per singlet.

aggregation is limited.

This result is further supported by an analysis of the guest-guest radial distribution function. Figure 6.15b shows the integral of the guest-guest (CoM to CoM) radial distribution function for the 6 wt% cubic lattice and MD-based morphologies, where it can be seen that the average concentration of guest molecules within a given radius around a chosen guest molecule is similar in both morphology cases. While the shape of the radial distribution function integral at approximately $r = 1$ nm for the MD-based morphology indicates some clustering of the guest, it is apparent that the step-wise nature of the cubic lattice approximates the underlying form. Figure 6.15 also offers an explanation towards why slightly more triplet loss due to dipole-dipole quenching was observed in the cubic lattice system compared to the MD-based system. It shows that despite the presence of guest clustering in the MD-based system, the lattice spacing results in a higher fraction of adjacent guest molecules < 1 nm apart, thus increasing the probability of dipole-dipole quenching.

To confirm that this result was not simply a coincidence of the guest concentration tested, further MD morphologies were generated at 10 wt% and 15 wt% guest

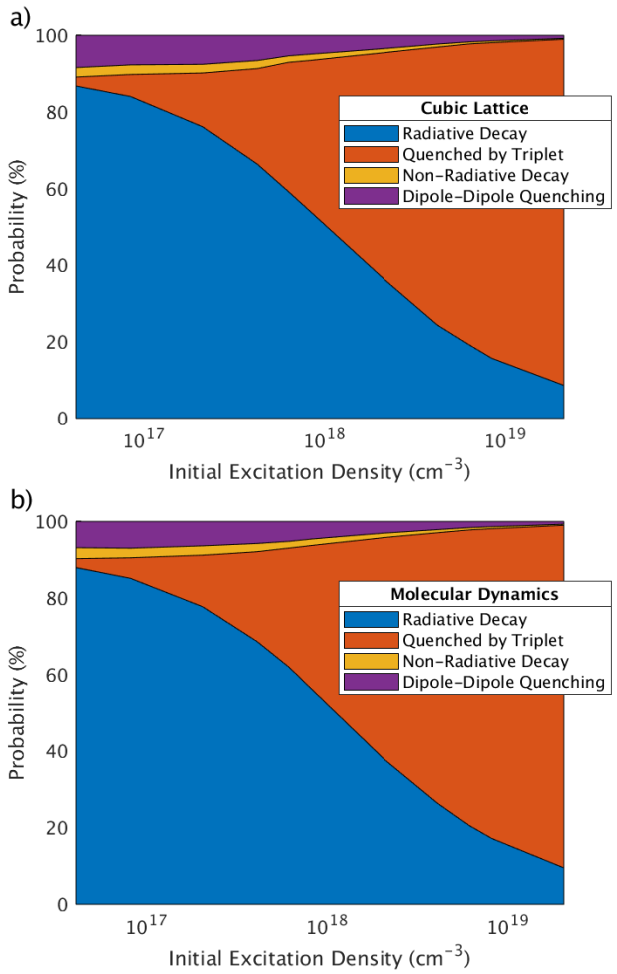

Figure 6.11: Comparison of triplet loss processes in (a) cubic lattice and (b) molecular dynamics-based morphologies at 6 wt% guest concentration. Note that since the observed guest-based triplet diffusion makes triplet-triplet annihilation in the host extremely unlikely, it was assumed that all triplets converted to singlets through that process were able to cross back to the triplet state, where they were subject to similar statistics. The fate of being converted to a singlet was therefore excluded from this graph, and the remaining fates re-normalised, to show only processes that reduce the number of triplet excitons in the system.

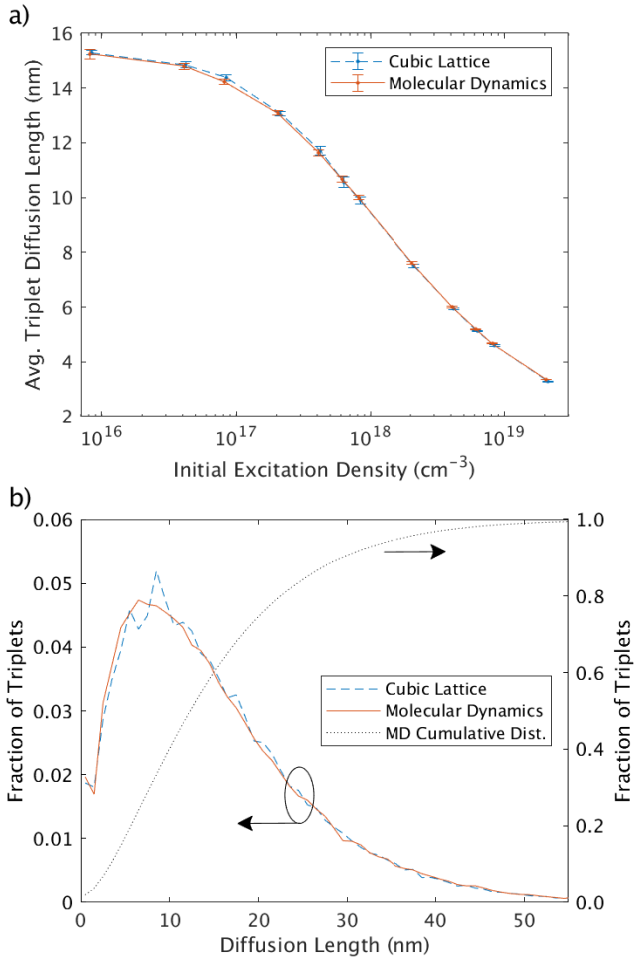

Figure 6.12: a) Comparison of triplet diffusion length in cubic lattice and molecular dynamics-based morphologies with a 6 wt% guest concentration. b) Comparison of the distribution of triplet diffusion lengths in the case of non-interacting excitons. Note that diffusion lengths longer than the film thickness are possible due to triplets diffusing parallel to the substrate.

concentrations with a film thickness of approximately 20 nm using the same vacuum deposition protocol as the 6 wt% systems. The guest-guest radial distribution functions of these films were compared to cubic lattice films with the same guest concentration and film thickness, and the results were found to be almost identical to the 6 wt% case. These results are provided as supporting information (Figures 6.16 & 6.17). The observed comparable distributions of guest molecules at these higher guest concentrations indicates that those distributions determined from the MD simulations are also well-approximated by a cubic lattice. As such, it would not be unreasonable to expect similar agreement between guest-based processes at other guest concentrations, at least under the approximations used in the current model in which molecular orientation is not considered. Similar differences in host-based processes are also expected, although the magnitude of these differences may be less meaningful at higher guest concentrations where singlet diffusion lengths are shorter, and fewer host molecules are visited by a given singlet.

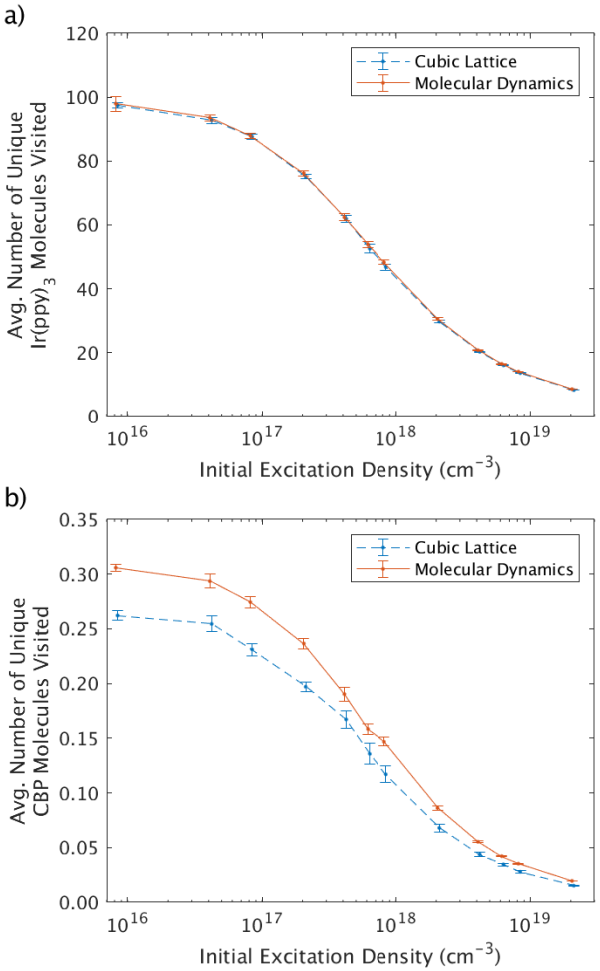

Figure 6.13: Comparison of the number of unique (a) guest and (b) host molecules visited per triplet in cubic lattice and molecular dynamics-based morphologies with a 6 wt% guest concentration. Note the difference in the scale of the y axes, as triplet transport occurs almost exclusively on the guest.

That comparable results for guest-based processes are found for this system where some limited clustering of the guest is present means that the lattice approach should also be applicable to similar systems where transport is dominated by hops between low-concentration trapping sites. The results could likely be further improved by introducing a random perturbation to the lattice sites in order to smooth out the step-wise character seen in Figure 6.15. We note that the exciton transport model presented here does not currently consider molecular orientation. However, this is a reasonable assumption as it has previously been shown that for $Ir(ppy)_3$:CBP blends, the $Ir(ppy)_3$ molecules tend to be randomly oriented in the bulk [118]. In that report it was also found that the CBP molecules did not show a preferred orientation apart from molecules near the substrate (1-2 nm), which tended to preferentially align with the substrate. In our current work we did not include a thermal anneal of the as-deposited films and whilst we also observed random orientation of the $Ir(ppy)_3$ molecules, we observed a small bias for the CBP molecules to have their long axis align with the substrate in the bulk (see Figure 6.18). That being said, in cases where there is strong

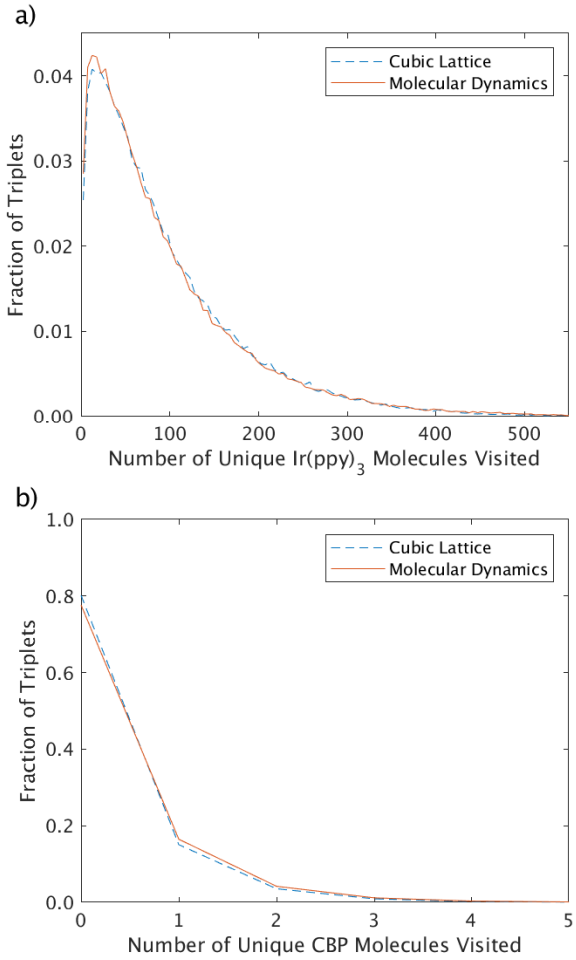

Figure 6.14: Comparison of the distribution of the number of unique guest (a) and host (b) molecules visited per triplet in cubic lattice and molecular dynamics-based morphologies with a 6 wt% guest concentration in the case of non-interacting excitons. Note that (b) additionally shows that almost 80% of triplets visit only guest molecules within their lifetime.

orientational order of components in the bulk and/or non-isotropic emission, it would be important for the orientation of the molecules within the film to be considered.

6.4 Summary

Kinetic Monte-Carlo modelling was used to simulate exciton dynamics in $Ir(ppy)_3$:CBP OLED films under photoexcitation at a range of guest concentrations and exciton densities. It was found that even at low guest concentrations, triplet diffusion occurs almost exclusively via guest-guest Dexter transfers, thereby increasing the likelihood of triplet-triplet annihilation. This would imply that under normal device operation, triplet-polaron quenching will have a similarly large contribution to efficiency roll-off, as we have previously shown in Chapter 4 that charge transport is also predominantly guest-based.

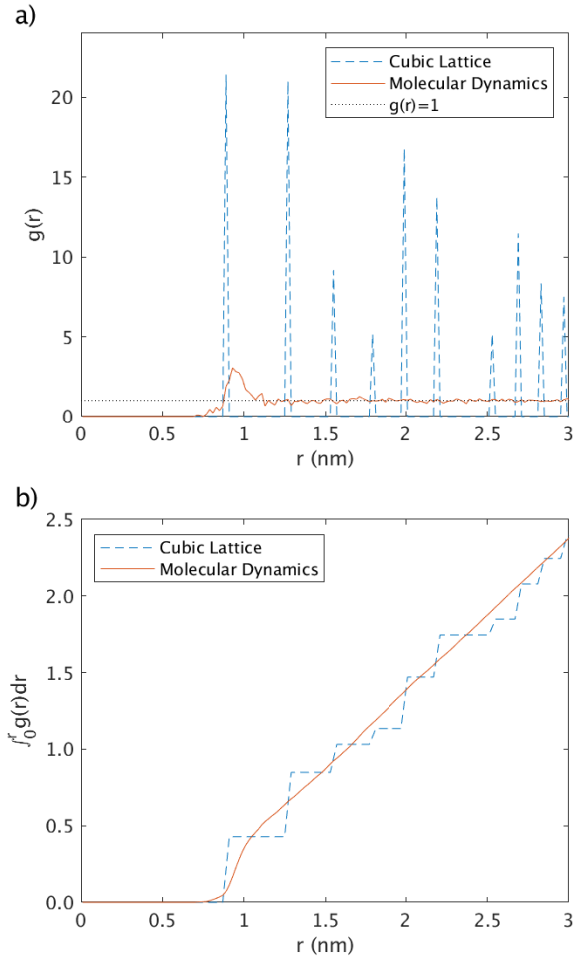

Figure 6.15: Guest-guest (CoM to CoM) radial distribution function (a) and its integral (b) for cubic lattice and MD-based morphologies with a 6 wt% guest concentration. The integral was used for clearer comparison due to the step-wise nature of the cubic lattice radial distribution function.

In addition, results from morphologies generated using molecular dynamics to simulate the process of vacuum deposition in atomic detail suggest that to a first approximation, KMC simulations based on a simple lattice model are representative of real systems in the case of processes that occur primarily on low concentration trapping sites. Thus, this method offers a relatively computationally efficient approach for modelling guest-dominated processes in guest-host phosphorescent OLEDs where the guest molecules are at low concentration and function as traps. However, while the fate of singlets in the modelled 6 wt% guest blends were comparable between the cubic lattice and molecular dynamics morphologies, some differences were observed in their diffusion dynamics, indicating that processes involving the host molecules are not as well-captured in the cubic lattice model. We also note that further differences in both host- and guest-based processes may be observable under a more detailed transport model that explicitly accounts for factors such as molecular orientation.

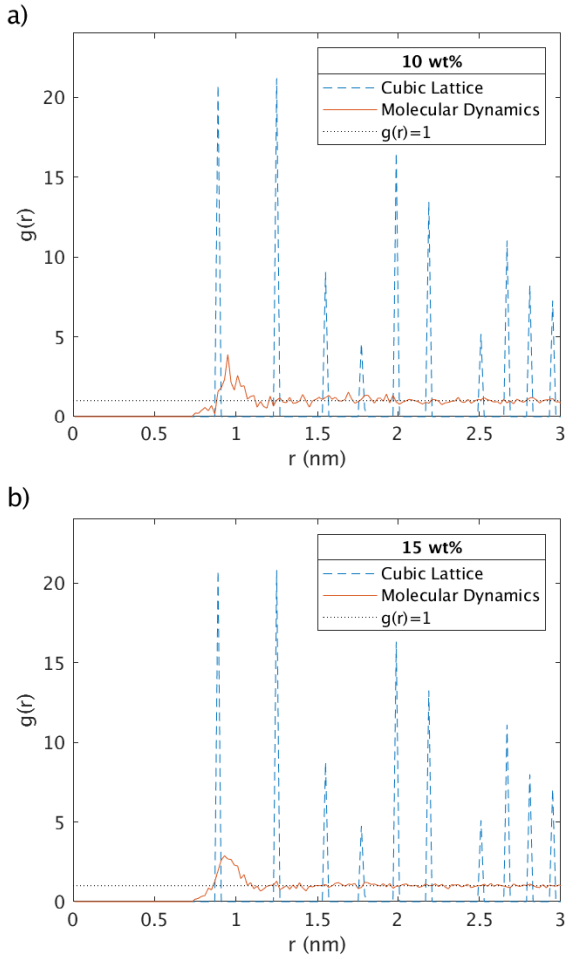

Figure 6.16: Guest-guest radial distribution functions for cubic lattice and molecular dynamics-based morphologies with (a) 10 wt% guest concentration and (b) 15 wt% guest concentration.

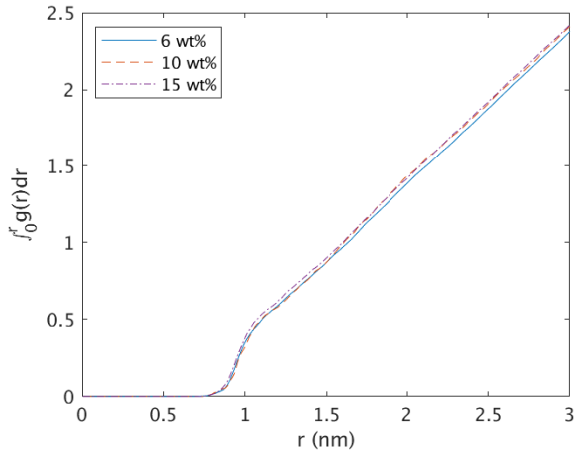

Figure 6.17: Comparison of the integral of the guest-guest radial distribution functions for molecular dynamics-based morphologies with guest concentrations of 6, 10 and 15 wt%. Note, the 6 wt% curve is averaged over three morphology realizations with a film thickness of 48 nm, while the 10 and 15 wt% curves are from single realizations with 20 nm film thicknesses.

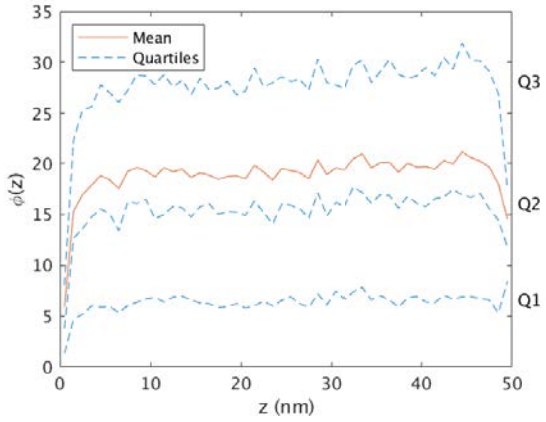

Figure 6.18: Distribution of the angle of the CBP long axis relative to the substrate as a function of the distance from the substrate, where 0° indicates parallel alignment, and 90° (the maximum possible) indicates perpendicular alignment. Note, the Q3 value indicates that 75% of CBP molecules in the bulk have a long axis angle of less than 30° relative to the substrate.

7

Effects of Deposition Technique on Charge and Exciton Dynamics

The following chapter presents work that is yet to be submitted for publication, but is intended for submission with George Vamvounis, Alan E. Mark, Paul L. Burn, Ronald D. White, and Bronson Philippa as co-authors. Molecular dynamics simulations were again performed using code developed by the group of Prof. Alan Mark, and the described modifications were initially proposed by him and developed and implemented by me. Assistance in debugging initial tests of the molecular dynamics scheme was provided by Dr. Martin Stroet and Audrey Sanzogni. All other work described in this chapter is my own.

7.1 Introduction

Solution processed OLEDs have a number of advantages over their vacuum-deposited counterparts, including cost and energy efficiency, scalability, simplicity, and less wasted material [187–191]. However, high performing small molecule OLEDs fabricated using solution deposition techniques tend to have poor stability and device lifetimes when compared to their equivalent vacuum-deposited counterparts [17, 192, 193]. Additionally, differences have also been observed between different solution deposition processes; for example, blade-coating has been shown to yield higher-performing films than spin-coating [17]. This has been attributed to differences in molecular packing structure leading to increased degradation rates [17, 192, 193]. However, some differences in charge transport have also been observed, which were similarly attributed to

different packing structure, despite minimal difference in the surface structure of the film [16].

The morphology of solution-deposited blends has also been analysed in the past using molecular dynamics techniques. Past work under the assumption of a 3-dimentionally periodic system from which solvent molecules are randomly removed showed film growth that is characteristic of spinoidal decomposition (spontaneous phase separation) [127, 128]. However, it was recently shown by Lee *et al.* that observing spinoidal decomposition in such a model is an inevitability, as no solvent concentration gradient is present [121]. While spinoidal decomposition is known to occur in some organic semiconductors, Lee *et al.* showed that inclusion of interfaces with a substrate and vacuum layer can instead result in nucleation and growth at the vacuum interface. In addition, they showed that this potentially leads to trapping of solvent molecules on long timescales, with some solvent likely to remain in the film for hours or even days [121]. This raises the question of whether charge and exciton dynamics in such a film differ from those in vacuum-deposited blends, and answering this question could offer a more detailed explanation towards the differences observed in device performance and degradation. For example, it has been suggested that faster degradation in solution-deposited small molecule phosphorescent OLEDs is due to molecular aggregation induced by exciton-polaron interactions [192, 194], but some questions remain about whether such interactions are less likely in vacuum-deposited films, or whether the aggregation process is slower due to differences in morphology.

In this chapter, a computational approach is used to investigate the molecular structures of solution- and vacuum-deposited blends in order to illuminate the effects of structural differences on charge transport and exciton dynamics. In particular, the archetypal emissive layer blend of 5 wt% *bis*(2-phenylpyridine)(acetylacetonate)iridium(III) [$Ir(ppy)_2(acac)$] in 4,4'-bis(*N*-carbazolyl)biphenyl (CBP) is investigated, building upon solution deposition MD techniques developed by Lee *et al.* [121]. Solution- and vacuum-deposited morphologies were generated using molecular dynamics simulations in atomic detail, and kinetic Monte-Carlo simulations were then utilised to investigate charge transport and exciton dynamics in the films under typical operating conditions. Details of the models are provided in Section 7.2, and an analysis of results is presented in Section 7.3 followed by concluding statements in Section 7.4.

7.2 Methodology

Solution- and vacuum-deposited morphologies were generated with periodic boundaries of 17.04 nm and 16.73 nm in the lateral directions, and the final films were replicated in those directions for a total periodic length of approximately 51 nm in order to avoid finite size effects in the KMC transport simulations. In both morphology cases, the temperature was controlled using a Berendsen thermostat as described in the previous chapter, with a temperature of 310 K. Upon reaching the final desired configuration, the temperature was reduced to 300 K, and the system was allowed to relax for a

further 10 ns. This is the temperature at which the KMC simulations were performed. Interaction parameters for CBP and the graphene substrate were identical to those of the previous chapter, and the interaction parameters for $Ir(ppy)_2(acac)$ were taken to be the same as those used by Lee *et al.* [121]. Further details of the solution and vacuum deposition schemes are provided in the following sections, along with details of the KMC transport simulations.

7.2.1 Solution Deposition

Molecular dynamics simulations of the solution deposition process were performed in which solvent molecules were allowed to boil off at the vacuum interface, and all molecules above a short distance form the top of the film were periodically removed from the system. The parameters used were those of Lee *et al.* [121], and we began the simulations using a snapshot from the 0.4 µs mark of the morphology produced by their simulations. However, two modifications were made to the simulation scheme in order to produce a thicker final film, and to speed up the drying process. These modifications are detailed in the following sections. Despite this, simulating solution deposition remains very computationally expensive, and only a single film with a total height of approximately 13 nm was achieved. However, we note that this is approximately 30% thicker than the 10 nm film generated by Lee *et al.*, while not requiring any additional atoms in the initial (slow) phase. Due to the different computing resources used to perform the simulations, we are unable to compare execution times.

The results of Lee *et al.* suggested that on experimental time scales, as much as 5 wt% solvent could remain trapped in the system [121]. To investigate this, two further films were generated in addition to the fully dried film by simply taking a morphology step with the desired solvent:solute molar ratio. Those systems were then allowed to relax for 5 ns at 300 K. The first of these films had a 1:4 solvent:solute molar ratio, which is equivalent to 5 wt% solvent and likely reflective of the upper limit of trapped solvent in real solution-deposited films. The other film had a 1:1 solvent:solute molar ratio (~17 wt%) in order to aid in disambiguating trends in the data related to the amount of trapped solvent from noise related to the small size and limited number of morphology realisations. We note that although $Ir(ppy)_2(acac)$:CBP OLEDs would not normally be manufactured by solution processing, this blend was chosen due to the availability of past data in order to reduce computational cost, and because it is reasonably comparable to other blends that have been studied experimentally under both deposition techniques [17, 192, 193].

Layer Expansion

To increase the thickness of the dried layer while maintaining a manageable number of atoms, a layer insertion scheme was developed that takes advantage of the drying process previously observed in this system. Lee *et al.* showed that in the presence of an interface, the solution deposited film of $Ir(ppy)_2(acac)$:CBP (and likely other similar blends) tends to develop a solute density gradient at the top of the film, while the

solute density in the lower section of the film remains close to the initial density with short correlation times between molecular trajectories [121]. Our layer insertion scheme monitors the solute density gradient, and triggered an insertion event when the lowest part of the gradient crossed a height threshold of 30 nm above the substrate (identified based on four consecutive 2.5 Å thick layers with a number density of solute atoms above 0.01 $Å^{-3}$). When an insertion event was triggered, potential splitting points were chosen from the lower section of the film (between 5 and 15 nm) where the fraction of atoms from solute molecules within a 2.5 Å thick layer was below 15%. A random splitting point was then chosen, and all molecules with at least one atom above this point were moved up to make space for an inserted layer of additional molecules with a solute density equal to that of the initial density. The inserted layer itself was chosen randomly from an auxiliary system. Each layer had a thickness of 6 ± 1.2 nm, and any molecules that crossed the upper or lower boundaries of the layer were discarded. Molecules crossing the splitting point in the main system were also removed to avoid any potential overlaps, and a gap of 1.7 Å was included between the bottom (top) atom of the layer and the lower (upper) section of the split system. This process is illustrated in Figure 7.1. The auxiliary system used as a source of new molecules was the $t = 0.1$ µs system of Lee *et al.* [121], and layers were taken from heights between 5 nm and 60 nm in that system. This system was used in favour of the $t = 0$ µs system to ensure random distribution of the solute in the solvent at the required density, since the $t = 0$ µs system (which was created by expanding and periodically repeating an 8.52 nm × 8.36 nm × 10.0 nm vacuum deposited film and filling the space with chloroform [121]) tended to yield layers that altered the guest:host ratio and typically had a solute density that was either too high or too low.

An analysis of the density profile of the system showed that the voids left by the insertion process collapsed very quickly, and the density profile in the region of insertion was indistinguishable from the surrounding system within 1 ns of relaxation (see Figure 7.2).

Solvent Deletion

To speed up drying of the film, solvent molecules were deleted randomly every 40 ps. To avoid influencing the film morphology, a maximum of 15 molecules were deleted at a time, with a minimum separation of 5 nm between deleted molecules. Deletion candidates were initially considered as those in a 12.5 nm section below the point at which the atomic density of the solute first exceeded 0.04 $Å^{-3}$. This scheme was chosen to avoid closing potential percolation pathways through the top of the film, while choosing those solvent molecules that are relatively likely to escape in the future.

Once the bottom of the removal section reached a height of 2 nm, the number of deleted solvent molecules per 40 ps was reduced to 10, and the atomic density cut-off was increased to 0.08 $Å^{-3}$. From this point, once the bottom of the removal section again reached 2 nm, its height was scaled to maintain that lower point, and the number of removals per step was adjusted such that the density of removed solvent molecules

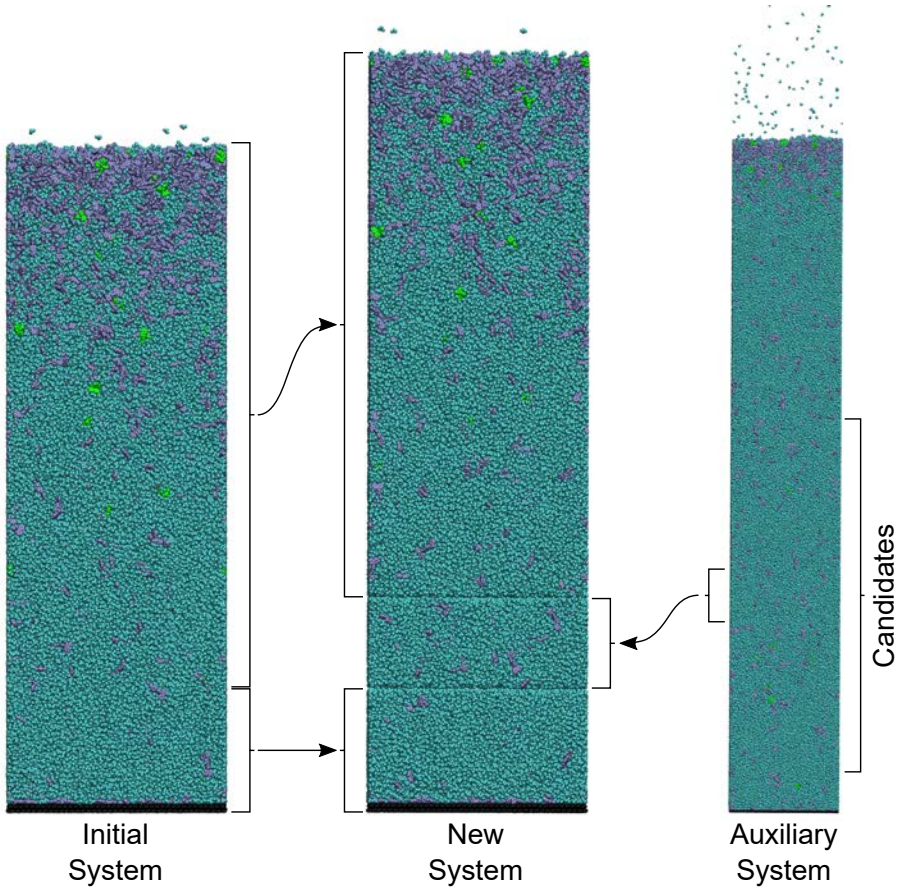

Figure 7.1: Illustration of the layer insertion process. Black, cyan, green and purple represent the substrate, solvent, guest and host atoms respectively, using a space filling model in the VMD visualisation software [195].

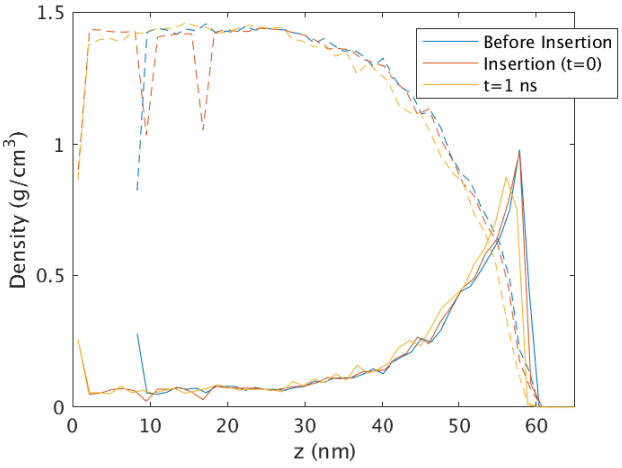

Figure 7.2: Density of solute (solid lines) and solvent (dashed lines) 40 ps before insertion, immediately after insertion, and 1 ns after insertion. Note, the density data before insertion was shifted on the z axis so that the tops of the layers were aligned.

remained constant. Finally, once the molar ratio of solvent to solute reached 2:1, the deletion scheme was modified to simply remove up to 10 solvent molecules per step from within the entire system until it was entirely dry (less solvent was removed if the minimum 5 nm separation condition could not be met).

7.2.2 Vacuum Deposition

Vacuum deposition simulations were performed using a scheme identical to that described in the previous chapter (see Section 6.2.2). Molecules were deposited 8 at a time at 16 ps intervals, until the total number of molecules matched that of the solution deposited morphology. Two separate realisations were generated, and results were averaged over these unless otherwise stated.

7.2.3 Transport Layers

To isolate the active layer from the electrodes, and to avoid potential artifacts caused by injection 'hot spots' related to the roughness of the top surface of the film, electron and hole transport layers were used. These transport layers were assumed to be "ideal", having energetically favourable injection to the active layer and relatively high mobility. They were also assumed to be perfectly blocking of excitons, and of the opposing charge, thus serving as a mechanism to efficiently supply charges to the active layer, while insulating the active layer from the electrodes. Both the upper and lower transport layers were generated as a cubic lattice with a lattice spacing (a) of approximately 0.89 nm (adjusted slightly in the x and y directions to maintain even spacing across the periodic boundaries). The charge hopping prefactor, $\nu_0^{(\mathrm{tx})}$, was set to 1×10^{13} s^{-1} for both transport layers to give reasonably realistic charge and exciton densities under typical applied fields, and site energies were randomly assigned from a Gaussian distribution of width 50 meV.

To fit the contours of the rough interface at the top of the active layer, the top transport layer was initially generated such that it overlapped with the active layer to approximately one lattice unit below the lowest "valley". The spatial offset of the top layer was then adjusted to explore all possible alignments at $0.1a$ intervals in all 3 directions; a total of 1000 trial alignments. For each alignment, a set of 3 criteria were evaluated with decreasing priority, and the alignment that best met that criteria was chosen. The first criteria was to minimize the number of conflicting molecules in the transport layer that would have to be removed. Conflicting molecules were considered as any transport layer molecule closer than one lattice unit to a molecule in the active layer. Secondly, for alignments with equally low numbers of conflicting molecules, the distance between each remaining transport layer molecule and its nearest neighbour in the active layer was calculated. Those distances less than $1.5a$ were then added to a list, R, and a figure of merit (FoM) was calculated as

$$\mathrm{FoM} = \mathrm{mean}\left(|R - a|\right). \tag{7.1}$$

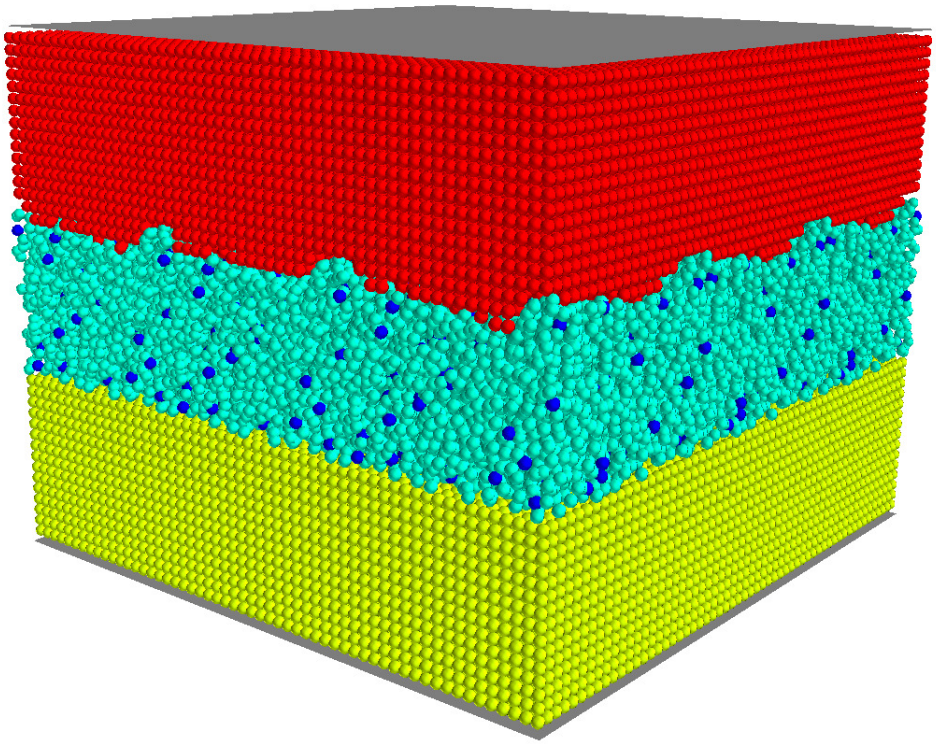

Figure 7.3: Example morphology showing a cubic lattice transport layer fitted to the rough top surface of the active layer. Red, lime, cyan, and dark blue spheres represent the hopping sites of the electron transport layer, hole transport layer, host, and guest respectively, and the grey planes represent the electrodes.

Lower FoM values were prioritised to select a configuration that minimized the average transport layer to active layer hopping distance while not making it unphysically short. Finally, in the unlikely case that more than one alignment had the same number of conflicting sites, and the same FoM, a secondary FoM was calculated using the standard deviation

$$\mathrm{FoM}_{\mathrm{std}} = \mathrm{std}\left(|R - a|\right), \tag{7.2}$$

and the configuration with the lowest value was chosen. This procedure was found to give a good interfacial fit, and an example of the resultant morphology is shown in Figure 7.3.

To ensure that this roughness fitting scheme did not introduce noticeable artifacts, KMC simulations (as described in Section 7.2.4) were performed in both forward and reverse bias configurations with equal electron and hole hopping rates, and with no distinction between guest and host molecules (to avoid any potential influence from height-dependent morphology). From these simulations, no appreciable difference was observed in the active layer mobility, and the distribution of charges and excitons in the z direction was similarly unaffected (see Figure 7.4). Note that the lowest considered electric field value of 3×10^5 V/cm is shown as it is the case that is most likely to

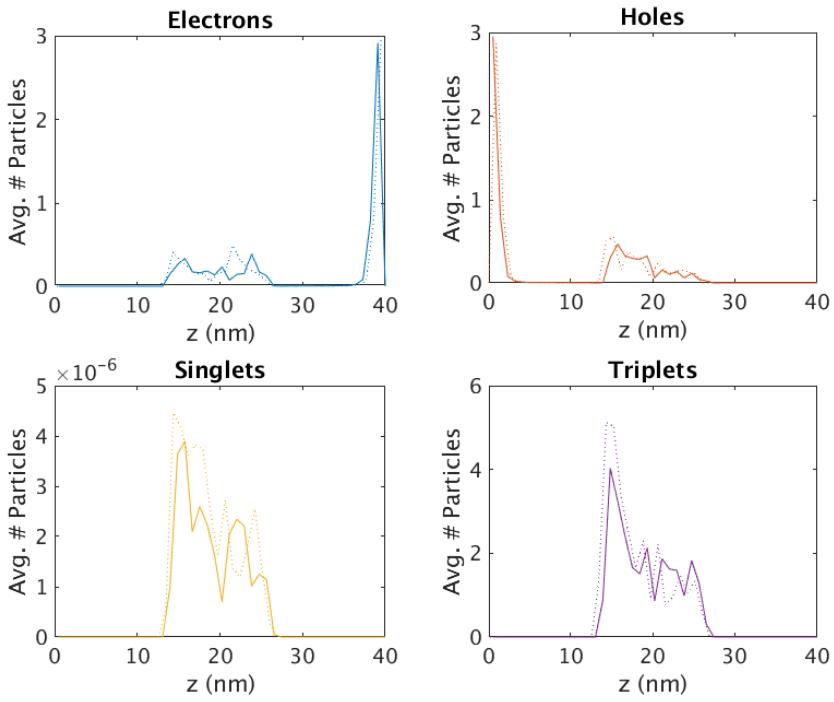

Figure 7.4: Number of charges and excitons in each 0.89 nm thick layer of the device for an applied field of 3×10^5 V/cm in forward bias (solid lines) and reverse bias (dotted lines), with no distinction made between guest and host molecules. Note the z coordinates of the reverse bias systems were reversed for easy comparison. Also note that this data represents only a single run, and is therefore subject to some noise.

reveal differences between forward and reverse bias, since there is less driving potential across the transport layer-active layer interface.

7.2.4 Kinetic Monte-Carlo

The basic details of the KMC scheme have been described in Chapter 3. Hopping sites were taken as the molecular centers of mass, and assigned energy values sampled from a Gaussian distribution. For each solution-deposited morphology, three energetic disorder realisations were used (and averaged over), and two energetic disorder realisations were used for each vacuum deposited layer. Four repeat simulations were performed for each energetic disorder realisation, giving a total of 12 simulations to average over per data point for the solution deposited systems, and 16 for the vacuum deposited system. Error bars in all cases were taken as the standard deviation of the mean, although it should be noted that some further variation is possible considering that only one molecular configuration was available for each solution-deposited system.

Charge injection and transport, as well as exciton diffusion and interactions, were simulated using the methods described in Chapter 3. Coulomb interactions were handled using the damped interaction scheme described in Section 3.2.3, with a decay parameter for the complementary error function of $\alpha = 0.03$ nm^{-1}, and with one periodic image in each direction. Site exclusion was enforced, such that electron (hole)

hops to the site of another electron (hole) were prohibited. Electron (hole) hops to the site of a hole (electron) were assumed to always be energetically favourable ($\Delta\mathcal{E}_{ij} \leq 0$), and to result in the formation of an exciton, randomly yielding a singlet or triplet in a 1:3 ratio. A summary of charge transport parameters is supplied in Table 7.1.

Exciton diffusion and interactions were handled as described in the previous chapter. Note that dipole-dipole quenching (as discussed in the previous chapter) was also included here given the similarities between $Ir(ppy)_2(acac)$ and $Ir(ppy)_3$, and it was assumed based on those similarities to have the same activation energy. Both radiative and non-radiative exciton decay events were considered with a fixed rate, with values outlined in Table 7.2. Note that singlet decay on guest molecules was excluded, since the intersystem crossing rate of $Ir(ppy)_2(acac)$ is much higher than the singlet decay rate [142,169,200]. Upon transfer to an occupied molecular site, exciton-exciton and exciton-polaron interactions were handled as described in Equation 2.1, noting that, as in the previous chapter, triplet-triplet annihilation was assumed to always result in the loss of one triplet, and the conversion of the other to a singlet. In addition to quenching caused by exciton transfer events, exciton-polaron interactions were also considered upon an electron or hole hopping to the site of an exciton, in which case that exciton was quenched. Table 7.2 provides a summary of the constants used to calculate exciton event rates.

7.3 Results

KMC simulations were performed under various applied biases equivalent to realistic electric field values. These values are provided in Table 7.3, along with the corresponding length of time that the simulation was allowed to run. Steady state was identified based on constancy in the number density of particles, and hence charge mobility results were averaged over the final 80% of the simulation, while exciton results were averaged over the final 50%.

7.3.1 Charge Transport

Mobility in the active layer was measured as

$$\mu = \frac{v_d}{E}, \tag{7.3}$$

where E is the applied electric field, and v_d is the average drift velocity in the active layer in the direction of the applied field. Drift velocity in the active layer was determined from charge hops in which both the source and destination site were active layer sites. Hops to and from sites in the transport layers were excluded to focus on the active layer only.

As can be seen in Figure 7.5, we observe minimal difference in hole mobility between the vacuum-deposited film and the dry solution-deposited film, but as the applied electric field increases there is some evidence of slower electron mobility in the solution-

Parameter	Symbol	Value	Ref.
Temperature	T	300 K	
Relative Permittivity	ε_r	2	note 1
Inverse Localization Radius	γ	2.9 nm^{-1}	note 2
LUMO	$E_{\text{LUMO}}^{(\text{guest})}$	-3.0 eV	[61, 196, 197]
	$E_{\text{LUMO}}^{(\text{host})}$	-2.9 eV	[58, 198]
HOMO	$E_{\text{HOMO}}^{(\text{guest})}$	-5.6 eV	[61, 196, 197]
	$E_{\text{HOMO}}^{(\text{host})}$	-6.0 eV	[58, 198]
Energetic Disorder	$\sigma_{\text{polarons}}^{(\text{guest,host})}$	162 meV	note 3
Electron Hopping Prefactor	$\nu_{\mathbf{e}}^{\mathbf{(guest)}}$	8.5×10^{12} s^{-1}	note 4
	$\nu_{\mathbf{e}}^{\mathbf{(host)}}$	1×10^{14} s^{-1}	[157], note 5
Hole Hopping Prefactor	$\nu_{\mathbf{h}}^{\mathbf{(guest)}}$	8.5×10^{12} s^{-1}	[199], note 5
	$\nu_{\mathbf{h}}^{\mathbf{(host)}}$	6.5×10^{14} s^{-1}	[157], note 5
Transport Layers	$\nu_0^{(\text{tx})}$	1×10^{13} s^{-1}	note 6
	$\sigma^{(\text{tx})}$	50 meV	note 6

Table 7.1: Summary of charge transport simulation constants.
[1)]See Chapter 4.
[2)]For simplicity, the inverse localization radius for triplet excitons in CBP was assumed to be equal to that of $Ir(ppy)_2(acac)$. The same simplifying assumption was also used for electrons and holes on both molecules as the value of 2.9 nm^{-1} is comparable with the value of 3.3 nm^{-1} assumed in other recent KMC studies [7, 108].
[3)]Energetic disorder of polaron states was assumed to be the same as that of a 6 wt% $Ir(ppy)_3$:CBP blend [155].
[4)]With a lack of experimental data, and considering the similarity in hole mobility between $Ir(ppy)_2(acac)$ and $Ir(ppy)_3$ [69, 199], the electron:hole mobility ratio of $Ir(ppy)_2(acac)$ was assumed to be 1:1 – the same as that of $Ir(ppy)_3$ (as measured by Mile Gao using the metal-insulator-semiconductor charge extraction via linearly increasing voltage (MIS-CELIV) technique in work that is yet to be published at the time of writing).
[5)]Miller-Abrahams hopping prefactors were chosen to give mobility values of 3×10^{-4} cm^2/Vs [157], 2×10^{-3} cm^2/Vs [157], and 2.4×10^{-5} cm^2/Vs [199] for $\nu_{\text{e}}^{(\text{host})}$, $\nu_{\text{h}}^{(\text{host})}$, and $\nu_{\text{e,h}}^{(\text{guest})}$ respectively under single carrier transport in a neat, 46 nm thick cubic lattice film with an applied voltage such that the average electric field was 4.9×10^5 V/cm.
[6)]Transport layer parameters were chosen such that exciton densities in the emissive layer under typical electric field strengths were within the typical range of experimentally observed values.

Parameter	Symbol	Value	Ref.
Förster Radius	$R_0^{(\text{S,host-host})}$	2.7 nm	[148]
	$R_0^{(\text{S,host-guest})}$	2.8 nm	note 1
	$R_0^{(\text{T,guest-guest})}$	2.1 nm	[51, 201]
Dexter Transfer Prefactor	$\nu_0^{(\text{T,host})}$	5.5×10^6 s^{-1}	note 2
	$\nu_0^{(\text{T,guest})}$	4.6×10^{11} s^{-1}	[202]
Triplet Decay Rate	$\nu_{\text{radiative}}^{(\text{T,guest})}$	5.875×10^5 s^{-1}	note 3
	$\nu_{\text{non-radiative}}^{(\text{T,guest})}$	3.75×10^4 s^{-1}	note 3
	$\nu_{\text{non-radiative}}^{(\text{T,host})}$	71.43 s^{-1}	[54]
Singlet Decay Rate	$\nu_{\text{radiative}}^{(\text{S,host})}$	1.2×10^9 s^{-1}	[142, 169]
	$\nu_{\text{non-radiative}}^{(\text{S,host})}$	8×10^8 s^{-1}	[142, 169]
Inter-System Crossing Rate	$\nu_{\text{ISC}}^{(\text{guest})}$	8.3×10^{11} s^{-1}	[200], note 4
Triplet Energy	$E_{\text{T}}^{(\text{host})}$	2.6 eV	[145, 167, 178]
	$E_{\text{T}}^{(\text{guest})}$	2.3 eV	[174, 196, 199]
Singlet Energy	$E_{\text{S}}^{(\text{host})}$	3.1 eV	note 5
	$E_{\text{S}}^{(\text{guest})}$	2.99 eV	[174]
Energetic Disorder	$\sigma_{\text{S,T}}^{(\text{guest})}$	50 meV	[201, 202], note 6
Dipole-Dipole Quenching Activation Energy	E_{quench}	170 meV	note 7

Table 7.2: Summary of exciton-related simulation constants.
[1)]The Förster radius for host to guest singlet transfer was assumed to be equal to the value measured by Ruseckas *et al.* for transfers from CBP to Ir(ppy)$_3$-cored dendrimers [142].
[2)]Triplet Dexter transfer rates in CBP were chosen such that the average triplet diffusion length was 140 nm [54] in a neat, fully periodic, cubic lattice system with a lattice spacing of 0.89 nm (see Chapter 4).
[3)]Radiative and non-radiative triplet decay rates in Ir(ppy)$_2$(acac) were calculated from a lifetime of 1.6 µs [203, 204] and an internal quantum efficiency of 0.94 [59].
[4)]The ISC rate was taken as the mean rate of the *cis-* and *trans-* isomers as calculated by Heil *et al.* [200].
[5)]The singlet energy of CBP was assumed to be equal to the HOMO-LUMO gap.
[6)]Energetic disorder of polaron states was assumed to be the same as that of a 6 wt% Ir(ppy)$_3$:CBP blend [155].
[7)]See Chapter 6 for a discussion of dipole-dipole quenching, and the calculation of this value. Note that due to the similar molecular structure of Ir(ppy)$_3$ and Ir(ppy)$_2$(acac), it was assumed in the absence of available data that the dipole-dipole quenching rate was also similar.

Applied Field (V/cm)	Simulation Time (µs)
3×10^5	40
4×10^5	25
5×10^5	10
6×10^5	6

Table 7.3: Applied electric fields and their corresponding run times.

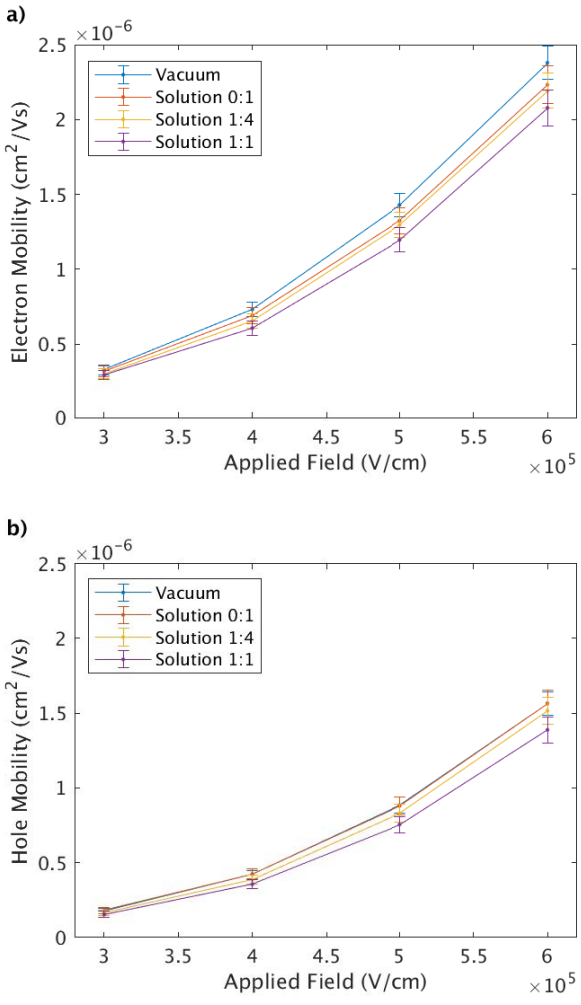

Figure 7.5: Comparison of (a) electron and (b) hole mobility as a function of the applied electric field for various solvent:solute molar ratios. Note in (b), the hole mobilities in the vacuum-deposited blend are almost identical to those in the 0:1 solvent:solute blend.

deposited film. As trapping of electrons on the guest is relatively shallow in these systems (0.1 eV), electron transport is significantly more host-based than hole transport, with the average electron visiting approximately twice as many host molecules as the average hole (see Figure 7.6). With this in mind, an analysis of the host packing structure is prudent.

Figure 7.7 shows that while CBP molecules in the vacuum-deposited film tend to preferentially be aligned with a relatively small angle between the long axis and the substrate, in the solution-deposited film this alignment is less prevalent. That is, the molecular orientation of CBP in the solution deposited film tends to be more broadly distributed when comparing as-deposited films that have not been thermally annealed. Hence, the shape of the CBP molecule means that the spacing between molecular centers of mass (CoMs) in the direction of the applied field is longer in the solution-deposited film, and therefore hopping rates in that direction are slower in this model. Note that a more precise method of calculating hopping rates that properly includes the effects of molecular orientation rather than only considering the CoM to CoM distance (density functional theory, for example), along with explicit calculation of site energies that accounts for local polarisation effects (and therefore the difference in orientational disorder) would likely reveal further differences, but the methods used here provide a good first approximation. Note also that results on the distribution of CBP orientations in the solution-deposited film are in good agreement with those presented by Lee *et al.*, despite the modifications to the deposition scheme [121].

Reduced electron mobility was also observed in the solution-deposited films with some trapped solvent remaining, and in this case hole mobility was also reduced. This was an expected result, as trapped solvent essentially reduces the density of available hopping sites. Kim *et al.* have previously reported some difference in current density between solution and vacuum-deposited blends of similar small molecule OLED films [16], which was ascribed to a lower packing density in the bulk of the film, despite similar surface structure. As molecular dynamics simulations have shown that pin holes in these systems tend to collapse on short time scales [121], our results suggest that this difference is likely due to the presence of trapped solvent. In particular, as shown in Figure 7.8, the trapped solvent tends to be concentrated towards the bottom of the film, and therefore thicker films may have a higher peak density of trapped solvent at the same solvent:solute ratio. Hence, the small differences observed in the thin layers modelled here are likely amplified in systems with more realistic active layer thicknesses, due to both the increase in peak trapped solvent density, and the likely increased thickness of the high solvent density region. In addition, Friederich *et al.* showed that solvent trapped in the system may also influence the energetic landscape [205], and could therefore further reduce mobility.

7.3.2 Exciton Dynamics

We begin an analysis of exciton dynamics under device operation by considering the fate of singlet excitons, particularly those that form on host molecules since once on

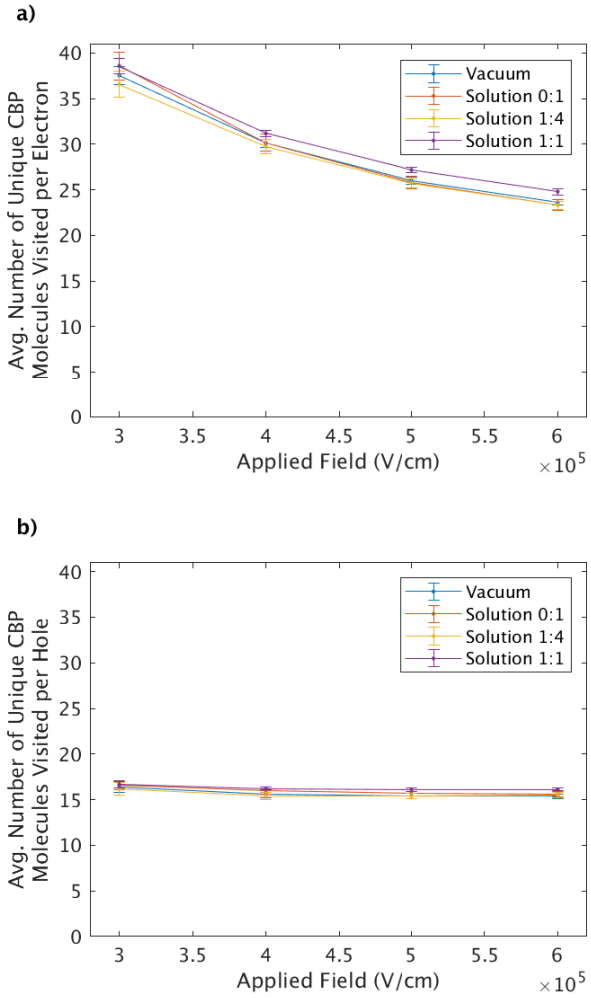

Figure 7.6: Comparison of the average number of host molecules visited per charge.

the guest it is overwhelmingly likely that intersystem crossing occurs. Figure 7.9 shows the probability that a singlet which formed on the host is either able to reach a guest molecule and cross to the triplet state, or is quenched by singlet-singlet annihilation (the dominant loss process). It is evident that results for the vacuum and solution deposited films are essentially identical within the limits of the transport model. As singlet diffusion occurs via Förster transfers (and is therefore sensitive to the transition dipole alignment of the donor and acceptor molecules), it is possible that the broader distribution of CBP orientations seen in the solution-deposited film (Figure 7.7) would lead to slightly slower average transfer rates compared to the vacuum-deposited morphology if orientation was included explicitly in the KMC model. However, considering that singlet diffusion is relatively fast compared to triplet and charge processes, and that singlets do not need to diffuse far to reach a guest molecule, significant differences in overall performance metrics are not expected. We also highlight that singlet-polaron quenching did not make a significant contribution to singlet loss, in agreement with the theory that degradation in these films is predominantly caused by triplet-polaron

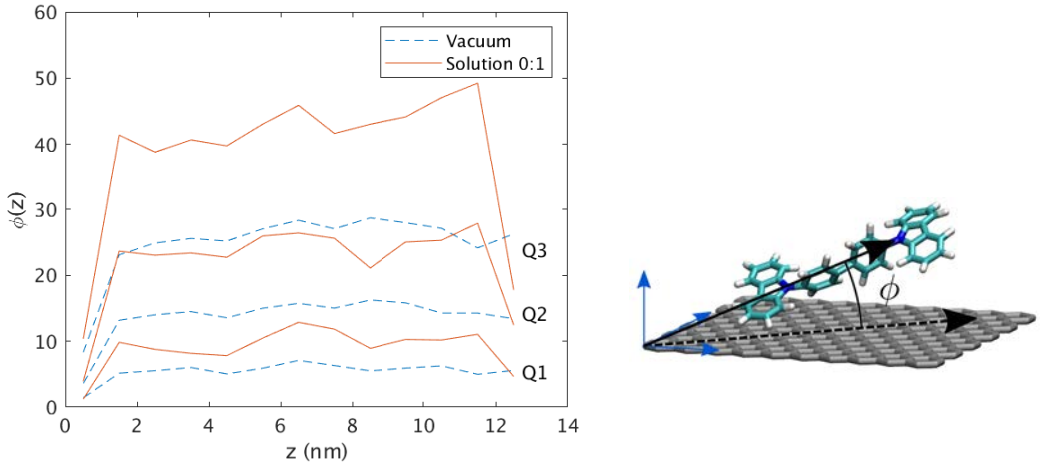

Figure 7.7: Comparison of the distribution of CBP orientations showing the first, second (median) and third quartile as a function of height. $\phi(z)$ was taken as the angle between the nitrogen to nitrogen vector and the substrate, as illustrated. Note that these results are for films that were deposited near room temperature, and have not undergone thermal annealing.

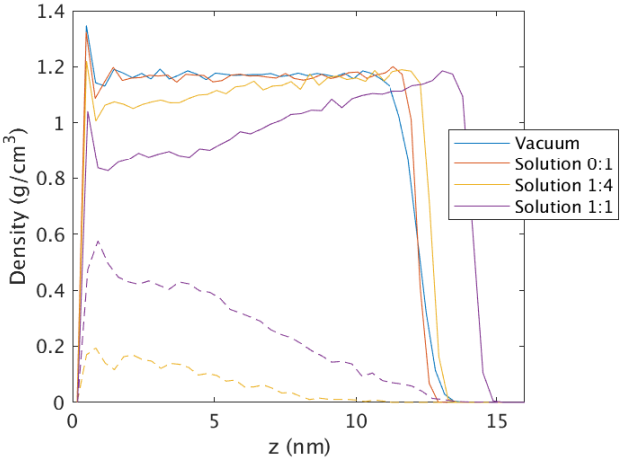

Figure 7.8: Comparison of density profiles of the solute (solid lines) and solvent (dashed lines).

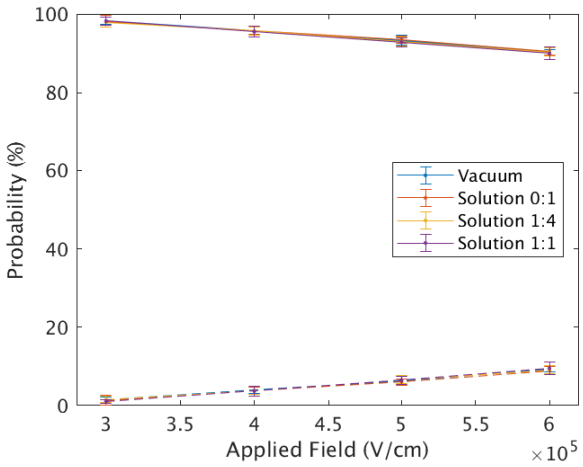

Figure 7.9: Comparison between vacuum- and solution-deposited films on the probability that a singlet which formed on a host molecule undergoes ISC by reaching a guest molecule (solid lines) or is lost to SSA (dashed lines) as a function of the applied electric field.

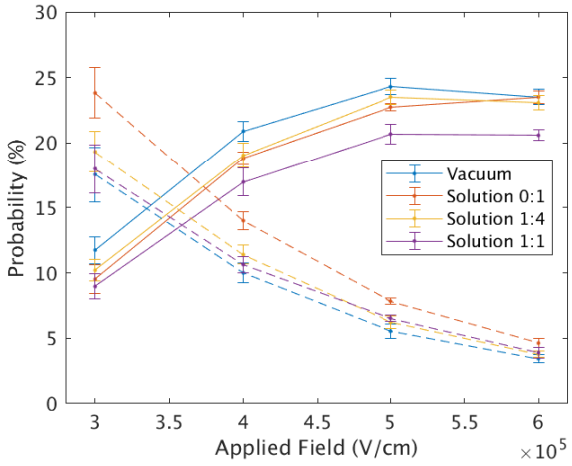

Figure 7.10: Comparison between vacuum and solution deposited layers of the probability that a triplet is quenched via TTA (solid lines) or via dipole-dipole quenching (dashed lines) as a function of the applied electric field. Note that for every triplet quenched via TTA, another was converted to a singlet.

quenching (TPQ) [206].

Once formed, triplet excitons were subject to a number of loss processes, and major contributions were observed from triplet-triplet annihilation, triplet-polaron quenching, and dipole-dipole quenching. Figures 7.10 and 7.11 show a comparison of these processes between the solution- and vacuum-deposited morphologies as a function of the applied electric field (and therefore density of triplets). While differences in the probability of TTA and TPQ were relatively small for realistic fractions of trapped solvent, Figure 7.10 shows that dipole-dipole quenching is approximately 5 percentage points more likely in the solution-deposited morphology with no trapped solvent, compared to the vacuum-deposited morphology. Given the r^{-6} distance dependence of

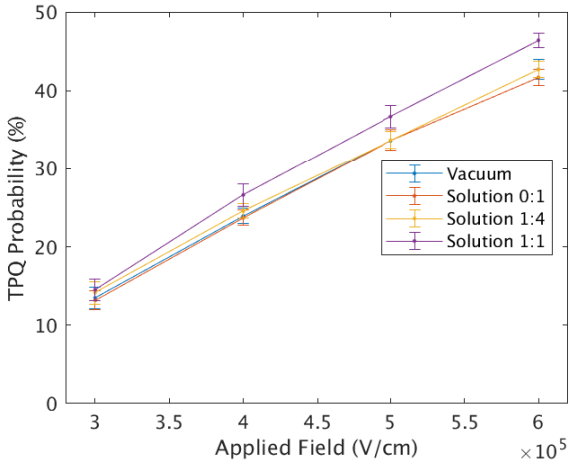

Figure 7.11: Comparison between solution- and vacuum-deposited films of the probability that a triplet is quenched by a polaron as a function of the applied electric field.

dipole-dipole quenching, this result is indicative of closer clustering of guest molecules. However, the lack of a clear trend for different fractions of trapped solvent suggests that the observed differences could simply be a peculiarity of the particular morphology realisations. To investigate this further, the average guest cluster size in each layer was analysed, where a cluster is defined as a group of molecules connected by at most r nm, where r is varied in this analysis. Figure 7.12 shows evidence of closer clustering in the 0:1 solvent:solute film compared to the other films, which corresponds well to the difference in dipole-dipole quenching probability observed in Figure 7.10. However, the apparent variance between morphology realisations suggests that this is indeed a chance occurrence, and further morphology realisations, ideally of thicker layers, would be required to establish any conclusive differences. We note, however, that in the case of a 1:1 solvent:solute ratio the probability of TTA is significantly reduced, while an increase is observed in the probability of TPQ. These differences are both explained by (and expected due to) the reduced density of guest and host molecules, and are therefore likely to be indicative of true device characteristics. As was observed in the previous chapter, triplet transport is almost entirely dominated by guest to guest Dexter transfers, and so increasing the average distance between guest clusters is expected to decrease triplet diffusion, and therefore reduce the likelihood of TTA. Similarly, with a lower chance of TTA, it stands to reason that triplet lifetimes would be longer (and this was indeed observed), leading to a higher probability of encountering a charge and being quenched via TPQ. Despite the observed difference at a 1:1 solvent:solute ratio, however, we reiterate that significant differences are not expected in real systems with plausible fractions of trapped solvent. Hence, it is apparent from Figure 7.13 that in realistic $Ir(ppy)_2(acac)$:CBP systems where degradation has not occurred, the probability that a triplet decays radiatively is relatively insensitive to the deposition technique, as is the probability of (potentially degradation-inducing) TPQ.

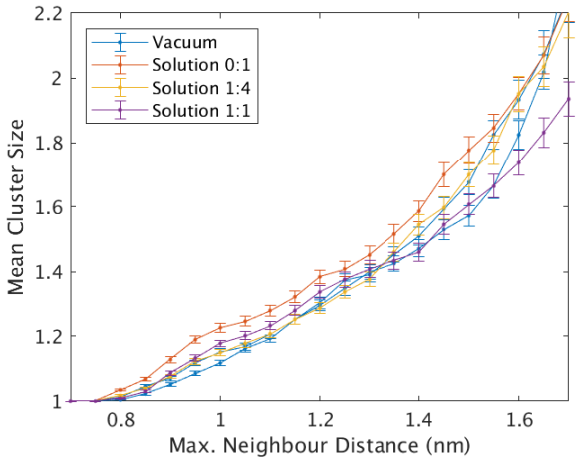

Figure 7.12: Comparison of the average number of guest molecules in a cluster for vacuum- and solution-deposited morphologies as a function of the CoM to CoM cut-off radius between neighbouring molecules considered to be in the same cluster. Note, the error bars represent the standard deviation of the mean within a single morphology, and the two vacuum deposited morphologies are plotted separately as an indication of the expected variance between morphology realisations.

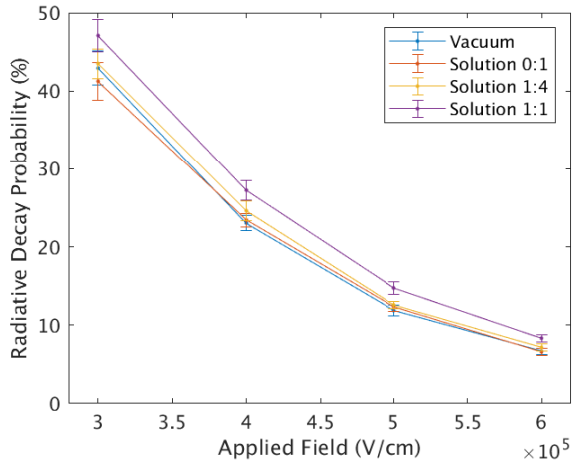

Figure 7.13: Comparison between vacuum- and solution-deposited films of the probability that a triplet decays radiatively as a function of the applied electric field.

7.4 Summary

Kinetic Monte-Carlo simulations were used to analyse charge and exciton dynamics in solution- and vacuum-deposited OLED films of 5 wt% $Ir(ppy)_2(acac)$:CBP that were generated by simulating the deposition process in atomic detail. It was found that for as-deposited films at room temperature, the solution-deposited films had a broader distribution of CBP orientations relative to the substrate when compared with those of the vacuum-deposited film. This indicates a more disordered packing structure, and lead to minor differences in the observed electron mobility. The presence of trapped solvent was also shown to reduce charge mobility, although the effects are likely minimal for experimentally plausible solvent concentrations. Furthermore, no significant differences were observed in exciton dynamics. In particular exciton-polaron interactions have been highlighted as a key mechanism for degradation in phosphorescent OLEDs [192, 194], and we observe no differences in these processes between solution- and vacuum-deposited films. These results therefore suggest that, within the limitations of the KMC model, the deposition technique has relatively little influence on the details of charge transport and exciton dynamics in films of $Ir(ppy)_2(acac)$:CBP that have not degraded. It is hence apparent that the faster degradation of solution-deposited films is likely a direct result of the difference in packing structure, and not due to differences in the behaviour of charges or excitons. In particular, considering that CBP orientations have been shown to be randomly distributed in the bulk in a similar blend after performing a thermal annealing simulation [118], and such annealing steps are not uncommon in device fabrication, we suggest that a plausible explanation of experimentally observed faster degradation is that trapped solvent enables faster TPQ-induced molecular aggregation, and we recommend further investigation into this. While the limitations of the KMC model mean that we cannot rule out the possibility of further differences in charge and exciton dynamics that are not captured by the approximations used here, the agreement of our results with experimentally observed phenomena [16, 193] suggests that the model provides a good first approximation.

8 Conclusion

8.1 Summary

An understanding of charge transport and exciton dynamics in OLEDs is crucial to improving their performance, and computational modelling techniques can offer insights that are difficult or impossible to achieve with current experimental methods. Kinetic Monte-Carlo modelling in particular provides the opportunity to elucidate key structure-property relationships, especially when paired with molecular dynamics morphology modelling, while also playing a crucial role in multi-scale models. In this thesis, these techniques were utilised to gain a deeper insight into the relationships between material properties and the behaviour of charges and excitons, with a particular focus on guest-host phosphorescent OLEDs. A kinetic Monte-Carlo model was developed from scratch to make use of GPU acceleration, and it was used to elucidate various structure-property relationships.

Considering the archetypal blend of an $Ir(ppy)_3$ guest in a CBP host, the effects of guest concentration on charge transport were investigated, and it was found that due to deep charge trapping on the guest, charges tend to spend the vast majority of their time on guest molecules, and this leads to the majority of excitons forming directly on or adjacent to the guest. In addition, it was shown that clustering of guest molecules leads to a transition as guest concentration increases from trapping on individual guest molecules to trapping on clusters of guest molecules, and finally to percolative transport. This results in a mobility minimum at approximately 10 wt%, where the density of traps is maximised.

After showing the significant effects of trapping on the guest, further KMC simulations were used to explore the influence of guest-host energy level alignment. While the

gap between electron affinity and ionisation potential of the guest and host were held constant, their relative alignment was adjusted from the case of no hole trapping and deep electron trapping, to that of deep hole trapping and no electron trapping. It was found that the relative alignment can have a marked effect on the mobility balance, particularly in the case where the slower charge carrier is trapped more deeply than the faster carrier, which leads to recombination on a timescale faster than that the thermalisation of the slower carrier. We highlight that proper pairing (or engineering) of guest and host energy level alignment can lead to improved mobility balance, and therefore reduce the likelihood of second order exciton quenching processes such as triplet-triplet annihilation.

On the role of exciton dynamics, simulated photoexcitation experiments were used to explore a large parameter space and investigate the effects of guest concentration and excitation density on the exciton diffusion and the relative contributions of loss processes in $Ir(ppy)_3$:CBP OLEDs. A concentration quenching process has been observed in $Ir(ppy)_3$ with a rate that is independent of the exciton density, and a method to include this process in the KMC model was introduced and benchmarked against experimental results. It was found that while this loss process can have a significant contribution at low exciton densities, triplet-triplet annihilation at higher exciton densities occurs on a faster time scale. Hence, it was shown that this process is unlikely to contribute to efficiency roll-off, and contributes to less than 4% of triplet loss above an excitation density of 5×10^{17} cm^{-3}. In addition, to validate the use of the commonly used cubic lattice morphology approximation, further photoexcitation simulations were performed at the experimentally determined optimal guest concentration of 6 wt% using morphology that was generated with molecular dynamics simulations in atomic detail. It was found that for guest-based processes such as triplet diffusion, the cubic lattice provides a surprisingly good approximation, at least at the low guest concentrations considered in this work. While some differences were observed in host-based processes, overall results were in good agreement within the approximations of the KMC model.

Finally, molecular dynamics modelling was used to compare solution- and vacuum-deposited films in order to elucidate differences observed in the degradation rate of experimental devices. This included developing techniques to reduce the computational cost of simulating the solution deposition process. Of particular interest was the effects of trapped solvent on performance characteristics of solution-deposited films, as it has been theorised that some solvent may remain trapped in the film on experimentally relevant timescales. By combining charge and exciton modelling, it was shown using KMC simulations that under typical device operation, at least within the limits of the model, experimentally probable levels of trapped solvent are unlikely to have a major effect on performance characteristics. In agreement with experimental results, it was found that overall performance characteristics were relatively insensitive to the deposition technique, with only minor differences observed in charge mobility, and no significant differences observed in the relative contribution of exciton loss processes.

However, the difference in mobility was attributed to differences in the alignment of the host relative to the substrate, with solution-deposition being shown to produce a more disordered packing structure in as-deposited films where a thermal annealing step was not performed. It was hence suggested that differences in degradation rate observed between solution- and vacuum-deposited small molecule phosphorescent OLEDs are likely directly related to the differences in packing structure, particularly in the presence of trapped solvent, and are not a product of differences in charge transport or exciton dynamics.

8.2 Recommendations for Future Work

While KMC modelling can produce detailed results that are in good agreement with experiment, they generally require a large number of approximations in the interest of reducing computational complexity, along with a substantial set of input parameters. The use of *ab initio* calculations presents a way of reducing both the number of approximations required, as well as the number of input parameters. For example, site energies are typically assigned by sampling from a Gaussian distribution, with a standard deviation determined either from experimental results, or by sampling a sub-section of the morphology using expensive quantum chemical calculations. However, we suggest that an alternative approach could make use of a classical polarizable forcefield in order to properly link site energy to morphology in a computationally efficient way. Additionally, transfer rates can have a significant dependence on molecular orientation, but explicit inclusion of this on a rate by rate basis is generally too expensive to be feasible in large systems. However, development of an efficient method for calculating transfer rates on a per-pair basis that properly considers molecular orientation (perhaps one based on machine learning) could pave the way to accurate *ab initio* simulations of systems with realistic film thicknesses. Such simulations could then be used to inform detailed drift-diffusion models on larger scales, thereby completing the multi-scale modelling pipeline and allowing for efficient prediction of device performance.

Another aspect of OLEDs that is not commonly considered in KMC models is the interface between the transport layers and the emissive layer. In particular, intermixing of the layers at the interface is known to occur, yet it is typically assumed in transport simulations that the interfaces are perfectly planar. With detailed modelling of the deposition process, along with accurate rate calculations, KMC simulations could reveal the effects of imperfect interfacial structures on device performance, and potentially reveal further design rules for more efficient devices.

Finally, modelling of electrode interfaces warrants further investigation. In particular, injection and removal rates often make a number of assumptions for convenience, for example assuming that injection is either Ohmic in nature, or directly from the Fermi level of the electrode (and not sampled from the Fermi distribution). Additionally, the physical geometry of the electrode is seldom considered, and it is

instead assumed to be perfectly planar. This assumption has the benefit of simplifying the electrostatics problem, as well as calculation of injection rates, but commonly used electrode materials such as indium tin oxide (ITO) can display significant degrees of roughness, and this is known to effect device performance. We suggest that with sophisticated, computationally efficient handling of electrostatics interactions, the electrode-organic interface could be simulated in greater detail to gain further insight into transport processes in that region. One potential solution to the electrostatics problem is to include direct computation of electrode surface charges rather than relying on the method of images, as has been recently employed in molecular dynamics simulations of supercapacitors [207].

References

[1] Stephen Sanderson, Bronson Philippa, George Vamvounis, Paul L. Burn, and Ronald D. White. Understanding charge transport in Ir(ppy)3:CBP OLED films. *The Journal of Chemical Physics*, **150**, 094110 (2019). doi:10.1063/1.5083639.

[2] Stephen Sanderson, Bronson Philippa, George Vamvounis, Paul L. Burn, and Ronald D. White. Elucidating the effects of guest-host energy level alignment on charge transport in phosphorescent OLEDs. *Applied Physics Letters*, **115**, 263301 (2019). doi:10.1063/1.5131680.

[3] Siddhartha Saggar, Stephen Sanderson, Desta Gedefaw, Xun Pan, Bronson Philippa, Mats R. Andersson, Shih-Chun Lo, and Ebinazar B. Namdas. Toward Faster Organic Photodiodes: Tuning of Blend Composition Ratio. *Advanced Functional Materials*, 2010661 (2021). doi:10.1002/adfm.202010661.

[4] Stephen Sanderson, George Vamvounis, Alan E. Mark, Paul L. Burn, Ronald D. White, and Bronson Philippa. Unraveling Exciton Processes in Ir(ppy)3:CBP OLED Films Upon Photoexcitation. *The Journal of Chemical Physics*, 164101 (2021). doi:10.1063/5.0044177.

[5] Seungjun Chung, Kyungjune Cho, and Takhee Lee. Recent Progress in Inkjet-Printed Thin-Film Transistors. *Advanced Science*, **6** (2019). doi:10.1002/advs.201801445.

[6] Hagen Klauk. *Organic Electronics: Materials, Manufacturing, and Applications*. Wiley-VCH, Weinheim (2006). ISBN 9783527312641.

[7] Reinder Coehoorn, Harm van Eersel, Peter A. Bobbert, and René A.J. Janssen. Kinetic Monte Carlo Study of the Sensitivity of OLED Efficiency and Lifetime to Materials Parameters. *Advanced Functional Materials*, **25**, 2024 (2015). doi:10.1002/adfm.201402532.

[8] Tyler Fleetham, Guijie Li, and Jian Li. Phosphorescent Pt(II) and Pd(II) Complexes for Efficient, High-Color-Quality, and Stable OLEDs. *Advanced Materials*, **29**, 1 (2017). doi:10.1002/adma.201601861.

[9] Stephen R. Forrest. The Path to Ubiquitous and Low-Cost Organic Electronic Appliances on Plastic. *Nature*, **428**, 911 (2004). doi:10.1038/nature02498.

[10] Yirang Im, Seong Yong Byun, Ji Han Kim, Dong Ryun Lee, Chan Seok Oh, Kyoung Soo Yook, and Jun Yeob Lee. Recent Progress in High-Efficiency Blue-Light-Emitting Materials for Organic Light-Emitting Diodes. *Advanced Functional Materials*, **27** (2017). doi:10.1002/adfm.201603007.

[11] Yawen Chen, Juanhong Wang, Zhiming Zhong, Zhixiong Jiang, Chen Song, Zhanhao Hu, Junbiao Peng, Jian Wang, and Yong Cao. Fabricating large-area white OLED lighting panels via dip-coating. *Organic Electronics*, **37**, 458 (2016). doi:10.1016/j.orgel.2016.07.025.

[12] Shi Jie Zou, Yang Shen, Feng Ming Xie, Jing De Chen, Yan Qing Li, and Jian Xin Tang. Recent advances in organic light-emitting diodes: Toward smart lighting and displays. *Materials Chemistry Frontiers*, **4**, 788 (2020). doi:10.1039/c9qm00716d.

[13] Qiang Wei, Nannan Fei, Amjad Islam, Tao Lei, Ling Hong, Ruixiang Peng, Xi Fan, Liang Chen, Pingqi Gao, and Ziyi Ge. Small-Molecule Emitters with High Quantum Efficiency: Mechanisms, Structures, and Applications in OLED Devices. *Advanced Optical Materials*, **6**, 1 (2018). doi:10.1002/adom.201800512.

[14] David L. Cheung and Alessandro Troisi. Modelling charge transport in organic semiconductors: From quantum dynamics to soft matter. *Physical Chemistry Chemical Physics*, **10**, 5941 (2008). doi:10.1039/b807750a.

[15] Lian Duan, Liudong Hou, Tae Woo Lee, Juan Qiao, Deqiang Zhang, Guifang Dong, Liduo Wang, and Yong Qiu. Solution processable small molecules for organic light-emitting diodes. *Journal of Materials Chemistry*, **20**, 6392 (2010). doi:10.1039/b926348a.

[16] Heekyung Kim, Younghun Byun, Rupasree Ragini Das, Byoung Ki Choi, and Pil Soo Ahn. Small molecule based and solution processed highly efficient red electrophosphorescent organic light emitting devices. *Applied Physics Letters*, **91**, 1 (2007). doi:10.1063/1.2776016.

[17] Viviane Nogueira Hamanaka, Elizabeth Salsberg, Fernando Josepetti Fonseca, and Hany Aziz. Investigating the influence of the solution-processing method on the morphological properties of organic semiconductor films and their impact on OLED performance and lifetime. *Organic Electronics*, **78**, 105509 (2020). doi:10.1016/j.orgel.2019.105509.

[18] C. W. Tang and S. A. Vanslyke. Organic electroluminescent diodes. *Applied Physics Letters*, **51**, 913 (1987). doi:10.1063/1.98799.

[19] Rico Meerheim, Björn Lüssem, and Karl Leo. Efficiency and stability of p-i-n type organic light emitting diodes for display and lighting applications. *Proceedings of the IEEE*, **97**, 1606 (2009). doi:10.1109/JPROC.2009.2022418.

[20] Mohan Jacob. Organic Semiconductors: Past, Present and Future. *Electronics*, **3**, 594 (2014). doi:10.3390/electronics3040594.

[21] Qisheng Zhang, Bo Li, Shuping Huang, Hiroko Nomura, Hiroyuki Tanaka, and Chihaya Adachi. Efficient blue organic light-emitting diodes employing thermally activated delayed fluorescence. *Nature Photonics*, **8**, 326 (2014). doi:10.1038/nphoton.2014.12.

[22] Sandip Tiwari. *Semiconductor physics: Principles, theory and nanoscale*. Oxford University Press (2020). ISBN 9780198759867. doi:10.1093/oso/9780198759867.001.0001.

[23] H Bässler. Charge Transport in Disordered Organic Photoconductors a Monte Carlo Simulation Study. *Physica Status Solidi B*, **175**, 15 (1993). doi:10.1002/pssb.2221750102.

[24] Pascal Kordt, Jeroen J M Van Der Holst, Mustapha Al Helwi, Wolfgang Kowalsky, Falk May, Alexander Badinski, Christian Lennartz, and Denis Andrienko. Modeling of Organic Light Emitting Diodes: From Molecular to Device Properties. *Advanced Functional Materials*, **25**, 1955 (2015). doi:10.1002/adfm.201403004.

[25] Abhishek P. Kulkarni, Christopher J. Tonzola, Amit Babel, and Samson A. Jenekhe. Electron transport materials for organic light-emitting diodes. *Chemistry of Materials*, **16**, 4556 (2004). doi:10.1021/cm049473l.

[26] Rudolph A. Marcus. Electron Transfer Reactions in Chemistry: Theory and Experiment (Nobel Lecture). *Angewandte Chemie International Edition in English*, **32**, 1111 (1993). doi:10.1002/anie.199311113.

[27] Natasha B. Taylor and Ivan Kassal. Generalised Marcus Theory for Multi-Molecular Delocalised Charge Transfer. *Chemical Science*, **9**, 2942 (2018). doi:10.1039/C8SC00053K.

[28] J. Spencer, F. Gajdos, and J. Blumberger. FOB-SH: Fragment orbital-based surface hopping for charge carrier transport in organic and biological molecules and materials. *Journal of Chemical Physics*, **145** (2016). doi:10.1063/1.4960144.

[29] Veaceslav Coropceanu, J. Cornil, D. A. da Silva Filho, Y. Olivier, R. Silbey, and J.-L. Brédas. Charge transport in organic semiconductors. *Chem. Rev.*, **107**, 926 (2007). doi:10.1007/128_2011_218.

[30] Victor Rühle, Alexander Lukyanov, Falk May, Manuel Schrader, Thorsten Vehoff, James Kirkpatrick, Björn Baumeier, and Denis Andrienko. Microscopic simulations of charge transport in disordered organic semiconductors. *Journal of Chemical Theory and Computation*, **7**, 3335 (2011). doi:10.1021/ct200388s.

[31] Harald Oberhofer, Karsten Reuter, and Jochen Blumberger. Charge Transport in Molecular Materials: An Assessment of Computational Methods. *Chemical Reviews*, **117**, 10319 (2017). doi:10.1021/acs.chemrev.7b00086.

[32] C Groves. Simulating charge transport in organic semiconductors and devices: a review. *Reports on Progress in Physics*, **80**, 026502 (2017). doi:10.1088/1361-6633/80/2/026502.

[33] Isao Tanaka and Shizuo Tokito. Temperature-dependent carrier-transport and light-emission processes in a phosphorescent organic light-emitting device. *Applied Physics Letters*, **87**, 1 (2005). doi:10.1063/1.2117609.

[34] Oleksandr V. Mikhnenko, Paul W. M. Blom, and Thuc Quyen Nguyen. Exciton diffusion in organic semiconductors. *Energy and Environmental Science*, **8**, 1867 (2015). doi:10.1039/c5ee00925a.

[35] S. Blumstengel, S. Sadofev, C. Xu, J. Puls, and F. Henneberger. Converting Wannier into Frenkel excitons in an inorganic/organic hybrid semiconductor nanostructure. *Physical Review Letters*, **97**, 8 (2006). doi:10.1103/PhysRevLett.97.237401.

[36] Miriam Engel, Frederik Kunze, Doru C. Lupascu, Niels Benson, and Roland Schmechel. Reduced exciton binding energy in organic semiconductors: Tailoring the Coulomb interaction. *Physica Status Solidi - Rapid Research Letters*, **6**, 68 (2012). doi:10.1002/pssr.201105488.

[37] Tim Albes and Alessio Gagliardi. Charge Pair Separation Dynamics in Organic Bulk-Heterojunction Solar Cells. *Advanced Theory and Simulations*, **1**, 1 (2018). doi:10.1002/adts.201800032.

[38] N Sariciftci, L Smilowitz, A. J Heeger, and F Wudl. Photoinduced Electron Transfer from a Conducting Polymer to Buckminsterfullerene. *Science*, **258**, 1474 (1992). doi:10.1126/science.258.5087.1474.

[39] Jeroen Brebels, Evgenia Douvogianni, Dries Devisscher, Raghavendran Thiruvallur Eachambadi, Jean Manca, Laurence Lutsen, Dirk Vanderzande, Jan C. Hummelen, and Wouter Maes. An effective strategy to enhance the dielectric constant of organic semiconductors – CPDTTPD-based low bandgap polymers bearing oligo(ethylene glycol) side chains. *Journal of Materials Chemistry C* (2018). doi:10.1039/C7TC05264B.

[40] Jianpu Wang, Alexei Chepelianskii, Feng Gao, and Neil C. Greenham. Control of exciton spin statistics through spin polarization in organic optoelectronic devices. *Nature Communications*, **3**, 1 (2012). doi:10.1038/ncomms2194.

[41] Joseph Shinar and Ruth Shinar. Organic light-emitting devices (OLEDs) and OLED-based chemical and biological sensors: An overview. *Journal of Physics D: Applied Physics*, **41**, 133001 (2008). doi:10.1088/0022-3727/41/13/133001.

[42] Y. Olivier, J. C. Sancho-Garcia, L. Muccioli, G. D'Avino, and D. Beljonne. Computational Design of Thermally Activated Delayed Fluorescence Materials: The Challenges Ahead. *Journal of Physical Chemistry Letters*, **9**, 6149 (2018). doi:10.1021/acs.jpclett.8b02327.

[43] Wei Li, Jiuyan Li, Fang Wang, Zhuo Gao, and Shufen Zhang. Universal Host Materials for High-Efficiency Phosphorescent and Delayed-Fluorescence OLEDs. *ACS Applied Materials and Interfaces*, **7**, 26206 (2015). doi:10.1021/acsami.5b08291.

[44] Kensuke Masui, Hajime Nakanotani, and Chihaya Adachi. Analysis of exciton annihilation in high-efficiency sky-blue organic light-emitting diodes with thermally activated delayed fluorescence. *Organic Electronics: physics, materials, applications*, **14**, 2721 (2013). doi:10.1016/j.orgel.2013.07.010.

[45] Yuchao Liu, Chensen Li, Zhongjie Ren, Shouke Yan, and Martin R. Bryce. All-organic thermally activated delayed fluorescence materials for organic light-emitting diodes. *Nature Reviews Materials*, **3**, 18020 (2018). doi:10.1038/natrevmats.2018.20.

[46] Xiaoqing Zhang, Canek Fuentes-Hernandez, Yadong Zhang, Matthew W. Cooper, Stephen Barlow, Seth R. Marder, and Bernard Kippelen. High performance blue-emitting organic light-emitting diodes from thermally activated delayed fluorescence: A guest/host ratio study. *Journal of Applied Physics*, **124**, 055501 (2018). doi:10.1063/1.5041447.

[47] D. L. Dexter. A theory of sensitized luminescence in solids. *The Journal of Chemical Physics*, **21**, 836 (1953). doi:10.1063/1.1699044.

[48] Theodor Förster. Zwischenmolekulare Energiewanderung und Fluoreszenz. *Annalen der Physik*, **437**, 55 (1948). doi:10.1002/andp.19484370105.

[49] Hans Kuhn. Classical aspects of energy transfer in molecular systems. *The Journal of Chemical Physics*, **53**, 101 (1970). doi:10.1063/1.1673749.

[50] D. F. O'Brien, M. A. Baldo, M. E. Thompson, and S. R. Forrest. Improved energy transfer in electrophosphorescent devices. *Applied Physics Letters*, **74**, 442 (1999). doi:10.1063/1.123055.

[51] Ebinazar B. Namdas, Arvydas Ruseckas, Ifor D.W. Samuel, Shih Chun Lo, and Paul L. Burn. Triplet exciton diffusion in fac-tris(2-phenylpyridine) iridium(III)-cored electroluminescent dendrimers. *Applied Physics Letters*, **86**, 091104 (2005). doi:10.1063/1.1867571.

[52] E. J. W. List, Ullrich Scherf, K. Müllen, W. Graupner, C.-H. Kim, and J. Shinar. Direct evidence for singlet-triplet exciton annihilation in π-conjugated polymers. *Physical Review B*, **66**, 235203 (2002). doi:10.1103/PhysRevB.66.235203.

[53] S. M. King, D. Dai, C. Rothe, and A. P. Monkman. Exciton annihilation in a polyfluorene: Low threshold for singlet-singlet annihilation and the absence of singlet-triplet annihilation. *Physical Review B - Condensed Matter and Materials Physics*, **76**, 085204 (2007). doi:10.1103/PhysRevB.76.085204.

[54] N. C. Giebink, Y. Sun, and S. R. Forrest. Transient analysis of triplet exciton dynamics in amorphous organic semiconductor thin films. *Organic Electronics: physics, materials, applications*, **7**, 375 (2006). doi:10.1016/j.orgel.2006.04.007.

[55] R. Coehoorn, L. Zhang, P. A. Bobbert, and H. van Eersel. Effect of polaron diffusion on exciton-polaron quenching in disordered organic semiconductors. *Physical Review B*, **95**, 1 (2017). doi:10.1103/PhysRevB.95.134202.

[56] Jean Luc Brédas, David Beljonne, Veaceslav Coropceanu, and Jérŏme Cornil. Charge-transfer and energy-transfer processes in π-conjugated oligomers and polymers: A molecular picture. *Chemical Reviews*, **104**, 4971 (2004). doi:10.1021/cr040084k.

[57] Bernard Geffroy, Philippe le Roy, and Christophe Prat. Organic light-emitting diode (OLED) technology: Materials, devices and display technologies. *Polymer International*, **55**, 572 (2006). doi:10.1002/pi.1974.

[58] Noriyuki Matsusue, Yuichiro Suzuki, and Hiroyoshi Naito. Charge carrier transport in neat thin films of phosphorescent iridium complexes. *Japanese Journal of Applied Physics, Part 1: Regular Papers and Short Notes and Review Papers*, **44**, 3691 (2005). doi:10.1143/JJAP.44.3691.

[59] Markus Schmid, Thomas Morgenstern, and Wolfgang Brütting. Enabling electron conduction in anisotropic hole transport materials for superior optical properties in organic light emitting diodes. *Organic Electronics*, **62**, 216 (2018). doi:10.1016/j.orgel.2018.08.010.

[60] Daisaku Tanaka, Hisahiro Sasabe, Yan Jun Li, Shi Jian Su, Takashi Takeda, and Junji Kido. Ultra high efficiency green organic light-emitting devices. *Japanese Journal of Applied Physics, Part 2: Letters*, **46**, 1 (2007). doi:10.1143/JJAP.46.L10.

[61] Chihaya Adachi, Marc A. Baldo, Mark E. Thompson, and Stephen R. Forrest. Nearly 100% internal phosphorescence efficiency in an organic light emitting device. *Journal of Applied Physics*, **90**, 5048 (2001). doi:10.1063/1.1409582.

[62] Jwo Huei Jou, Sudhir Kumar, Abhishek Agrawal, Tsung Han Li, and Snehashis Sahoo. Approaches for fabricating high efficiency organic light emitting diodes. *Journal of Materials Chemistry C*, **3**, 2974 (2015). doi:10.1039/c4tc02495h.

[63] Youtian Tao, Chuluo Yang, and Jingui Qin. Organic host materials for phosphorescent organic light-emitting diodes. *Chemical Society Reviews*, **40**, 2943 (2011). doi:10.1039/c0cs00160k.

[64] Hiroki Uoyama, Kenichi Goushi, Katsuyuki Shizu, Hiroko Nomura, and Chihaya Adachi. Highly efficient organic light-emitting diodes from delayed fluorescence. *Nature*, **492**, 234 (2012). doi:10.1038/nature11687.

[65] Wei Jiang, Lian Duan, Juan Qiao, Guifang Dong, Liduo Wang, and Yong Qiu. Tuning of charge balance in bipolar host materials for highly efficient solution-processed phosphorescent devices. *Organic Letters*, **13**, 3146 (2011). doi:10.1021/ol201039n.

[66] Kuo Gao, Kunkun Liu, Xiang Long Li, Xinyi Cai, Dongjun Chen, Zhida Xu, Zuozheng He, Binbin Li, Zhenyang Qiao, Dongcheng Chen, Yong Cao, and Shi Jian Su. An ideal universal host for highly efficient full-color, white phosphorescent and TADF OLEDs with a simple and unified structure. *Journal of Materials Chemistry C*, **5**, 10406 (2017). doi:10.1039/c7tc04149g.

[67] Yi Yeol Lyu, Jeonghun Kwak, Woo Sung Jeon, Younghun Byun, Hyo Sug Lee, Doseok Kim, Changhee Lee, and Kookheon Char. Highly efficient red phosphorescent OLEDs based on non-conjugated silicon-cored spirobifluorene derivative doped with ir-complexes. *Advanced Functional Materials*, **19**, 420 (2009). doi:10.1002/adfm.200801319.

[68] Runda Guo, Wenzhi Zhang, Qing Zhang, Xialei Lv, and Lei Wang. Efficient deep red phosphorescent OLEDs using 1,2,4-thiadiazole core-based novel bipolar host with low efficiency roll-off. *Frontiers of Optoelectronics*, **11**, 375 (2018). doi:10.1007/s12200-018-0855-4.

[69] Mile Gao, Thomas Lee, Paul L. Burn, Alan E. Mark, Almantas Pivrikas, and Paul E. Shaw. Revealing the Interplay between Charge Transport, Luminescence Efficiency, and Morphology in Organic Light-Emitting Diode Blends. *Advanced Functional Materials*, **30**, 1 (2019). doi:10.1002/adfm.201907942.

[70] Guangchao Han, Yuanping Yi, and Zhigang Shuai. From Molecular Packing Structures to Electronic Processes: Theoretical Simulations for Organic Solar Cells. *Advanced Energy Materials*, **8**, 1702743 (2018). doi:10.1002/aenm.201702743.

[71] Bijan Movaghar, Leighton O. Jones, Mark A. Ratner, George C. Schatz, and Kevin L. Kohlstedt. Are Transport Models Able to Predict Charge Carrier Mobilities in Organic Semiconductors? *Journal of Physical Chemistry C*, **123**, 29499 (2019). doi:10.1021/acs.jpcc.9b06250.

[72] Alexander Heck, Julian J. Kranz, Tomás Kubar, and Marcus Elstner. Multi-scale approach to non-adiabatic charge transport in high-mobility organic semiconductors. *Journal of Chemical Theory and Computation*, **11**, 5068 (2015). doi:10.1021/acs.jctc.5b00719.

[73] Shosei Kubo and Hironori Kaji. Parameter-Free Multiscale Simulation Realising Quantitative Prediction of Hole and Electron Mobilities in Organic Amorphous System with Multiple Frontier Orbitals. *Scientific Reports*, **8**, 1 (2018). doi:10.1038/s41598-018-31722-w.

[74] Haoyuan Li, Yong Qiu, and Lian Duan. Multi-scale calculation of the electric properties of organic-based devices from the molecular structure. *Organic Electronics: physics, materials, applications*, **33**, 164 (2016). doi:10.1016/j.orgel.2016.03.016.

[75] Andrea Massé, Pascal Friederich, Franz Symalla, Feilong Liu, Robert Nitsche, Reinder Coehoorn, Wolfgang Wenzel, and Peter A. Bobbert. Ab initio charge-carrier mobility model for amorphous molecular semiconductors. *Physical Review B*, **93**, 1 (2016). doi:10.1103/PhysRevB.93.195209.

[76] L. J. A. Koster, E. C P Smits, V. D. Mihailetchi, and P. W. M. Blom. Device model for the operation of polymer/fullerene bulk heterojunction solar cells. *Physical Review B - Condensed Matter and Materials Physics*, **72**, 1 (2005). doi:10.1103/PhysRevB.72.085205.

[77] Denis Andrienko. Multiscale Concepts in Simulations of Organic Semiconductors. *Handbook of Materials Modeling*, 1–12 (2018). doi:10.1007/978-3-319-42913-7_39-1.

[78] Waldemar Kaiser, Tim Albes, and Alessio Gagliardi. Charge carrier mobility of disordered organic semiconductors with correlated energetic and spatial disorder. *Physical Chemistry Chemical Physics*, **20**, 8897 (2018). doi:10.1039/c8cp00544c.

[79] Frank Ortmann, K. Sebastian Radke, Alrun Günther, Daniel Kasemann, Karl Leo, and Gianaurelio Cuniberti. Materials Meets Concepts in Molecule-Based Electronics. *Advanced Functional Materials*, **25**, 1933 (2015). doi:10.1002/adfm.201402334.

[80] Björn Baumeier, Falk May, Christian Lennartz, and Denis Andrienko. Challenges for in silico design of organic semiconductors. *Journal of Materials Chemistry*, **22**, 10971 (2012). doi:10.1039/c2jm30182b.

[81] J. J. M. van der Holst, F. W. A. van Oost, R Coehoorn, and P A Bobbert. Monte Carlo study of charge transport in organic sandwich-type single-carrier devices: Effects of Coulomb interactions. *Physical Review B*, **83**, 085206 (2011). doi:10.1103/PhysRevB.83.085206.

[82] Daniel T. Gillespie. A general method for numerically simulating the stochastic time evolution of coupled chemical reactions. *Journal of Computational Physics*, **22**, 403 (1976). doi:10.1016/0021-9991(76)90041-3.

[83] Daniel Balzer, Thijs J. A. M. Smolders, David Blyth, Samantha N. Hood, and Ivan Kassal. Delocalised kinetic Monte Carlo for simulating delocalisation-enhanced charge and exciton transport in disordered materials. *Chemical Science*, 1–9 (2021). doi:10.1039/d0sc04116e.

[84] Waldemar Kaiser, Johannes Popp, Michael Rinderle, Tim Albes, and Alessio Gagliardi. Generalized kinetic Monte Carlo framework for organic electronics. *Algorithms*, **11** (2018). doi:10.3390/a11040037.

[85] Björn Baumeier, Ole Stenzel, Carl Poelking, Denis Andrienko, and Volker Schmidt. Stochastic modeling of molecular charge transport networks. *Physical Review B*, **86**, 184202 (2012). doi:10.1103/PhysRevB.86.184202.

[86] Xander De Vries, Pascal Friederich, Wolfgang Wenzel, Reinder Coehoorn, and Peter A. Bobbert. Full quantum treatment of charge dynamics in amorphous molecular semiconductors. *Physical Review B*, **97**, 1 (2018). doi:10.1103/PhysRevB.97.075203.

[87] Franz Symalla, Shahriar Heidrich, Maximilian Kubillus, Timo Strunk, Tobias Neumann, and Wolfgang Wenzel. Boosting OLED performance with ab-initio modeling of roll-off and quenching processes. *Digest of Technical Papers - SID International Symposium*, **50**, 259 (2019). doi:10.1002/sdtp.12905.

[88] Franz Symalla, Shahriar Heidrich, Pascal Friederich, Timo Strunk, Tobias Neumann, Daiki Minami, Daun Jeong, and Wolfgang Wenzel. Multiscale Simulation of Photoluminescence Quenching in Phosphorescent OLED Materials. *Advanced Theory and Simulations*, **3**, 1 (2020). doi:10.1002/adts.201900222.

[89] Michael C. Heiber, Andrew A. Herzing, Lee J. Richter, and Dean M. DeLongchamp. Charge transport and mobility relaxation in organic bulk heterojunction morphologies derived from electron tomography measurements. *Journal of Materials Chemistry C*, 11–13 (2020). doi:10.1039/d0tc03087b.

[90] S. V. Novikov, D. H. Dunlap, V. M. Kenkre, P. E. Parris, and A. V. Vannikov. Essential Role of Correlations in Governing Charge Transport in Disordered Organic Materials. *Physical Review Letters*, **81**, 4472 (1998). doi:10.1103/PhysRevLett.81.4472.

[91] J. Frenkel. On pre-breakdown phenomena in insulators and electronic semiconductors [3]. *Physical Review*, **54**, 647 (1938). doi:10.1103/PhysRev.54.647.

[92] S. L. M. van Mensfoort, V. Shabro, R. J. De Vries, R. A. J. Janssen, and R. Coehoorn. Hole transport in the organic small molecule material α-NPD: Evidence for the presence of correlated disorder. *Journal of Applied Physics*, **107** (2010). doi:10.1063/1.3407561.

[93] Pascal Friederich, Franz Symalla, Velimir Meded, Tobias Neumann, and Wolfgang Wenzel. Ab initio treatment of disorder effects in amorphous organic

materials: Toward parameter free materials simulation. *Journal of Chemical Theory and Computation*, **10**, 3720 (2014). doi:10.1021/ct500418f.

[94] W. F. Pasveer, J. Cottaar, C. Tanase, R. Coehoorn, P. A. Bobbert, P. W. M. Blom, M. De Leeuw, and M. A. J. Michels. Unified description of charge-carrier mobilities in disordered semiconducting polymers. *Physical Review Letters*, **94** (2005). doi:10.1103/PhysRevLett.94.206601.

[95] Upendra Neupane, Behzad Bahrami, Matt Biesecker, Mahdi Farrokh Baroughi, and Qiquan Qiao. Kinetic Monte Carlo modeling on organic solar cells: Domain size, donor-acceptor ratio and thickness. *Nano Energy*, **35**, 128 (2017). doi:10.1016/j.nanoen.2017.03.041.

[96] Robin G. E. Kimber, Alison B. Walker, Gerd E. Schröder-Turk, and Douglas J. Cleaver. Bicontinuous minimal surface nanostructures for polymer blend solar cells. *Physical Chemistry Chemical Physics*, **12**, 844 (2010). doi:10.1039/b916340a.

[97] Lingyi Meng, Yuan Shang, Qikai Li, Yongfang Li, Xiaowei Zhan, Zhigang Shuai, Robin G E Kimber, and Alison B Walker. Dynamic Monte Carlo Simulation for Highly Efficient Polymer Blend Photovoltaics. *The Journal of Physical Chemistry B*, **114**, 36 (2010). doi:10.1021/jp907167u.

[98] J. Zhou, Y C Zhou, J M Zhao, C Q Wu, X M Ding, and X Y Hou. Carrier density dependence of mobility in organic solids: A Monte Carlo simulation. *Physical Review B - Condensed Matter and Materials Physics*, **75**, 1 (2007). doi:10.1103/PhysRevB.75.153201.

[99] H. Van Eersel, P. A. Bobbert, and R. Coehoorn. Kinetic Monte Carlo study of triplet-triplet annihilation in organic phosphorescent emitters. *Journal of Applied Physics*, **117** (2015). doi:10.1063/1.4914460.

[100] Samantha N. Hood and Ivan Kassal. Entropy and Disorder Enable Charge Separation in Organic Solar Cells. *Journal of Physical Chemistry Letters*, **7**, 4495 (2016). doi:10.1021/acs.jpclett.6b02178.

[101] J. Eduard Hoogenboom. Is Monte Carlo embarrassingly parallel? *International Conference on the Physics of Reactors 2012, PHYSOR 2012: Advances in Reactor Physics*, **2**, 936 (2012).

[102] Anthony Lee, Christopher Yau, Michael B. Giles, Arnaud Doucet, and Christopher C. Holmes. On the Utility of Graphics Cards to Perform Massively Parallel Simulation of Advanced Monte Carlo Methods. *Journal of Computational and Graphical Statistics*, **19**, 769 (2010). doi:10.1198/jcgs.2010.10039.

[103] N. J. van der Kaap and L. J. A. Koster. Massively parallel kinetic Monte Carlo simulations of charge carrier transport in organic semiconductors. *Journal of Computational Physics*, **307**, 321 (2016). doi:10.1016/j.jcp.2015.12.001.

[104] William Robert Saunders, James Grant, Eike Hermann Müller, and Ian Thompson. Fast electrostatic solvers for kinetic Monte Carlo simulations. *Journal of Computational Physics*, **410**, 109379 (2020). doi:10.1016/j.jcp.2020.109379.

[105] Michael Pippig and Francesco Mercuri. Efficient evaluation of Coulomb interactions in kinetic Monte Carlo simulations of charge transport. *The Journal of Chemical Physics*, **152**, 164102 (2020). doi:10.1063/5.0003258.

[106] Haoyuan Li and Jean-Luc Brédas. Kinetic Monte Carlo Modeling of Charge Carriers in Organic Electronic Devices: Suppression of the Self-Interaction Error. *The Journal of Physical Chemistry Letters*, **8**, 2507 (2017). doi:10.1021/acs.jpclett.7b01161.

[107] W. F. Pasveer, J. Cottaar, C. Tanase, R. Coehoorn, P. A. Bobbert, P. W. M. Blom, M. De Leeuw, and M. A. J. Michels. Unified description of charge-carrier mobilities in disordered semiconducting polymers. *Physical Review Letters*, **94**, 1 (2005). doi:10.1103/PhysRevLett.94.206601.

[108] H. Van Eersel, P. A. Bobbert, R. A.J. Janssen, and R. Coehoorn. Monte Carlo study of efficiency roll-off of phosphorescent organic light-emitting diodes: Evidence for dominant role of triplet-polaron quenching. *Applied Physics Letters*, **105** (2014). doi:10.1063/1.4897534.

[109] M. Mesta, H. van Eersel, R. Coehoorn, and P. A. Bobbert. Kinetic Monte Carlo modeling of the efficiency roll-off in a multilayer white organic light-emitting device. *Applied Physics Letters*, **108** (2016). doi:10.1063/1.4945087.

[110] David A. Case, Thomas E. Cheatham, Tom Darden, Holger Gohlke, Ray Luo, Kenneth M. Merz, Alexey Onufriev, Carlos Simmerling, Bing Wang, and Robert J. Woods. The Amber biomolecular simulation programs. *Journal of Computational Chemistry*, **26**, 1668 (2005). doi:10.1002/jcc.20290.

[111] Abdulnour Y. Toukmaji and John A. Board. Ewald summation techniques in perspective: A survey. *Computer Physics Communications*, **95**, 73 (1996). doi:10.1016/0010-4655(96)00016-1.

[112] P. P. Ewald. Die Berechnung optischer und elektrostatischer Gitterpotentiale. *Annalen der Physik*, **369**, 253 (1921). doi:10.1002/andp.19213690304.

[113] Anna Karin Tornberg. The Ewald sums for singly, doubly and triply periodic electrostatic systems. *Advances in Computational Mathematics*, **42**, 227 (2016). doi:10.1007/s10444-015-9422-3.

[114] Mark James Abraham, Teemu Murtola, Roland Schulz, Szilárd Páll, Jeremy C. Smith, Berk Hess, and Erik Lindah. Gromacs: High performance molecular simulations through multi-level parallelism from laptops to supercomputers. *SoftwareX*, **1-2**, 19 (2015). doi:10.1016/j.softx.2015.06.001.

[115] Sahar Sharifzadeh, Cathy Y. Wong, Hao Wu, Benjamin L. Cotts, Leeor Kronik, Naomi S. Ginsberg, and Jeffrey B. Neaton. Relating the Physical Structure and Optoelectronic Function of Crystalline TIPS-Pentacene. *Advanced Functional Materials*, **25**, 2038 (2015). doi:10.1002/adfm.201403005.

[116] Qiang Zhao, Lei Li, Fuyou Li, Mengxiao Yu, Zhipan Liu, Tao Yi, and Chunhui Huang. Aggregation-induced phosphorescent emission (AIPE) of iridium(III) complexes. *Chemical Communications*, **3**, 685 (2008). doi:10.1039/b712416c.

[117] Mattias Jakobsson, Mathieu Linares, and Sven Stafstrom. Monte Carlo simulations of charge transport in organic systems with true off-diagonal disorder. *The Journal of Chemical Physics*, **137**, 114901 (2012). doi:10.1063/1.4748796.

[118] Claire Tonnelé, Martin Stroet, Bertrand Caron, Andrew J. Clulow, Ravi C. R. Nagiri, Alpeshkumar K. Malde, Paul L. Burn, Ian R. Gentle, Alan E. Mark, and Benjamin J. Powell. Elucidating the Spatial Arrangement of Emitter Molecules in Organic Light-Emitting Diode Films. *Angewandte Chemie - International Edition*, **56**, 8402 (2017). doi:10.1002/anie.201610727.

[119] U. Wolf, V. Arkhipov, and H. Bässler. Current injection from a metal to a disordered hopping system. I. Monte Carlo simulation. *Physical Review B*, **59**, 7507 (1999). doi:10.1103/PhysRevB.59.7507.

[120] Thomas Lee, Bertrand Caron, Martin Stroet, David M. Huang, Paul L. Burn, and Alan E. Mark. The Molecular Origin of Anisotropic Emission in an Organic Light-Emitting Diode. *Nano Letters*, **17**, 6464 (2017). doi:10.1021/acs.nanolett.7b03528.

[121] Thomas Lee, Audrey V. Sanzogni, Paul L. Burn, and Alan E. Mark. Evolution and morphology of thin films formed by solvent evaporation: An organic semiconductor case study. *ACS Applied Materials and Interfaces*, **12**, 40548 (2020). doi:10.1021/acsami.0c08454.

[122] Pascal Friederich, Vadim Rodin, Florian Von Wrochem, and Wolfgang Wenzel. Built-In Potentials Induced by Molecular Order in Amorphous Organic Thin Films. *ACS Applied Materials and Interfaces*, **10**, 1881 (2018). doi:10.1021/acsami.7b11762.

[123] Michael P. Allen and Dominic J. Tildesley. Computer simulation of liquids: Second edition. *Computer Simulation of Liquids: Second Edition*, 1–626 (2017). doi:10.1093/oso/9780198803195.001.0001.

[124] Marko Mladenovic and Nenad Vukmirovic. Charge Carrier Localization and Transport in Organic Semiconductors: Insights from Atomistic Multiscale Simulations. *Advanced Functional Materials*, **25**, 1915 (2015). doi:10.1002/adfm.201402435.

[125] Yuki Nagata. Polarizable atomistic calculation of site energy disorder in amorphous Alq3. *ChemPhysChem*, **11**, 474 (2010). doi:10.1002/cphc.200900648.

[126] Guangchao Han, Xingxing Shen, Ruihong Duan, Hua Geng, and Yuanping Yi. Revealing the influence of the solvent evaporation rate and thermal annealing on the molecular packing and charge transport of DPP(TBFu)2. *Journal of Materials Chemistry C*, **4**, 4654 (2016). doi:10.1039/c6tc01201a.

[127] Cheng Kuang Lee and Chun Wei Pao. Nanomorphology evolution of p3ht/pcbm blends during solution-processing from coarse-grained molecular simulations. *Journal of Physical Chemistry C*, **118**, 11224 (2014). doi:10.1021/jp501323p.

[128] Riccardo Alessandri, Jaakko J. Uusitalo, Alex H. De Vries, Remco W.A. Havenith, and Siewert J. Marrink. Bulk Heterojunction Morphologies with Atomistic Resolution from Coarse-Grain Solvent Evaporation Simulations. *Journal of the American Chemical Society*, **139**, 3697 (2017). doi:10.1021/jacs.6b11717.

[129] Mark James Abraham, Teemu Murtola, Roland Schulz, Szilárd Páll, Jeremy C. Smith, Berk Hess, and Erik Lindahl. Gromacs: High performance molecular simulations through multi-level parallelism from laptops to supercomputers. *SoftwareX*, **1-2**, 19 (2015). doi:10.1016/j.softx.2015.06.001.

[130] Melissa E O'Neill. PCG: A Family of Simple Fast Space-Efficient Statistically Good Algorithms for Random Number Generation. Technical Report HMC-CS-2014-0905, Harvey Mudd College, Claremont, CA (2014).

[131] Weifeng Zhou, Christoph Zimmermann, and Christoph Jungemann. Master equation study of excitonic processes limiting the luminous efficacy in phosphorescent organic light-emitting diodes. *Journal of Applied Physics*, **125**, 165501 (2019). doi:10.1063/1.5082164.

[132] Dylan Kipp and Venkat Ganesan. A kinetic Monte Carlo model with improved charge injection model for the photocurrent characteristics of organic solar cells. *Journal of Applied Physics*, **113**, 234502 (2013). doi:10.1063/1.4811337.

[133] Lingyi Meng, Dong Wang, Qikai Li, Yuanping Yi, Jean-Luc Brédas, and Zhigang Shuai. An improved dynamic Monte Carlo model coupled with Poisson equation to simulate the performance of organic photovoltaic devices. *Journal of Chemical Physics*, **134**, 124102 (2011). doi:10.1063/1.3569130.

[134] M. M. Taddei, T. N. C. Mendes, and C. Farina. Subtleties in energy calculations in the image method. *European Journal of Physics*, **30**, 133001 (2009). doi:10.1088/0143-0807/30/5/005.

[135] Yulong Shen, Ahmad R. Hosseini, Man Hoi Wong, and George G. Malliaras. How to make ohmic contacts to organic semiconductors. *ChemPhysChem*, **5**, 16 (2004). doi:10.1002/cphc.200300942.

[136] J. R. Nagel. Solving the Generalized Poisson Equation Using the Finite-Difference Method (FDM). Technical report, University of Utah, Salt Lake City (2012).

[137] Florian Fahrenberger. *Dielectric Variations in Simulations of Charged Soft Matter*. Ph.D. thesis (2016). doi:10.18419/opus-5209.

[138] J. Colmenares, A. Galizia, J. Ortiz, A. Clematis, and W. Rocchia. A combined MPI-CUDA parallel solution of linear and nonlinear Poisson-Boltzmann equation. *BioMed Research International*, **2014** (2014). doi:10.1155/2014/560987.

[139] Mosè Casalegno, Guido Raos, and Riccardo Po. Methodological assessment of kinetic Monte Carlo simulations of organic photovoltaic devices: The treatment of electrostatic interactions. *The Journal of Chemical Physics*, **132**, 094705 (2010). doi:10.1063/1.3337909.

[140] D. Wolf, P. Keblinski, S. R. Phillpot, and J. Eggebrecht. Exact method for the simulation of Coulombic systems by spherically truncated, pairwise r-1 summation. *Journal of Chemical Physics*, **110**, 8254 (1999). doi:10.1063/1.478738.

[141] J. C. Ribierre, A. Ruseckas, K. Knights, S. V. Staton, N. Cumpstey, P. L. Burn, and I. D.W. Samuel. Triplet exciton diffusion and phosphorescence quenching in iridium(III)-centered dendrimers. *Physical Review Letters*, **100**, 017402 (2008). doi:10.1103/PhysRevLett.100.017402.

[142] A. Ruseckas, J. C. Ribierre, P. E. Shaw, S. V. Staton, P. L. Burn, and I. D.W. Samuel. Singlet energy transfer and singlet-singlet annihilation in light-emitting blends of organic semiconductors. *Applied Physics Letters*, **95**, 2007 (2009). doi:10.1063/1.3253422.

[143] Michael C. Heiber and Ali Dhinojwala. Dynamic Monte Carlo modeling of exciton dissociation in organic donor-acceptor solar cells. *Journal of Chemical Physics*, **137**, 014903 (2012). doi:10.1063/1.4731698.

[144] M. Scheidler, U. Lemmer, R. Kersting, S. Karg, W. Riess, B. Cleve, R. Mahrt, H. Kurz, H. Bässler, E. Göbel, and P. Thomas. Monte Carlo study of picosecond exciton relaxation and dissociation in poly(phenylenevinylene). *Physical Review B*, **54**, 5536 (1996). doi:10.1103/PhysRevB.54.5536.

[145] Ayataka Endo and Chihaya Adachi. Photoluminescence characteristics of tris(2-phenylquinoline)iridium(III) dispersed in an iridium complex host layer. *Chemical Physics Letters*, **483**, 224 (2009). doi:10.1016/j.cplett.2009.10.064.

[146] Yusuke Fujii, Takuya Azumi, Nobuhiko Nishio, Shinpei Kato, and Masato Edahiro. Data transfer matters for GPU computing. *Proceedings of the International Conference on Parallel and Distributed Systems - ICPADS*, 275–282 (2013). doi:10.1109/ICPADS.2013.47.

[147] Mark Harris, Shubhabrata Sengupta, and John D. Owens. Parallel Prefix Sum (Scan) with CUDA Mark. In *GPU Gems 3*, April, chapter 39. Addison-Wesley Professional (2007). ISBN 9780321515261.

[148] Richard R. Lunt, Noel C. Giebink, Anna A. Belak, Jay B. Benziger, and Stephen R. Forrest. Exciton diffusion lengths of organic semiconductor thin films measured by spectrally resolved photoluminescence quenching. *Journal of Applied Physics*, **105**, 053711 (2009). doi:10.1063/1.3079797.

[149] Armantas Melianas, Vytenis Pranculis, Yuxin Xia, Nikolaos Felekidis, Olle Inganäs, Vidmantas Gulbinas, and Martijn Kemerink. Photogenerated Carrier Mobility Significantly Exceeds Injected Carrier Mobility in Organic Solar Cells. *Advanced Energy Materials*, **7** (2017). doi:10.1002/aenm.201602143.

[150] Giulio Simone, Matthew J. Dyson, Stefan C.J. Meskers, René A.J. Janssen, and Gerwin H. Gelinck. Organic Photodetectors and their Application in Large Area and Flexible Image Sensors: The Role of Dark Current. *Advanced Functional Materials*, **30** (2020). doi:10.1002/adfm.201904205.

[151] M. A. Baldo, S. Lamansky, P. E. Burrows, M. E. Thompson, and S. R. Forrest. Very high-efficiency green organic light-emitting devices based on electrophosphorescence. *Applied Physics Letters*, **75**, 4 (1999). doi:10.1063/1.124258.

[152] Stefan Kappaun, Christian Slugovc, and Emil J.W. List. Phosphorescent organic light-emitting devices: Working principle and iridium based emitter materials. *International Journal of Molecular Sciences*, **9**, 1527 (2008). doi:10.3390/ijms9081527.

[153] Arthur R. G. Smith, Jeremy L. Ruggles, Hamish Cavaye, Paul E. Shaw, Tamim A. Darwish, Michael James, Ian R. Gentle, and Paul L. Burn. Investigating morphology and stability of fac-tris (2-phenylpyridyl) iridium(III) films for OLEDs. *Advanced Functional Materials*, **21**, 2225 (2011). doi:10.1002/adfm.201002365.

[154] I. I. Fishchuk, A. Kadashchuk, S. T. Hoffmann, S. Athanasopoulos, J. Genoe, H. Bässler, and A. Köhler. Analytic model of hopping transport in organic semiconductors including both energetic disorder and polaronic contributions. *Physical Review B*, **88**, 125202 (2013). doi:10.1063/1.4893509.

[155] Mikhail A. Parshin, Jeroen Ollevier, and Mark van der Auweraer. Charge carrier mobility in CBP films doped with Ir(ppy) 3. *Organic Optoelectronics and Photonics II*, **6192**, 61922A (2006). doi:10.1117/12.663553.

[156] W. F. Pasveer, P. A. Bobbert, H. P. Huinink, and M. A. J. Michels. Scaling of current distributions in variable-range hopping transport on two- and three-dimensional lattices. *Physical Review B - Condensed Matter and Materials Physics*, **72**, 174204 (2005). doi:10.1103/PhysRevB.72.174204.

[157] Jae Wook Kang, Se Hyung Lee, Hyung Dol Park, Won Ik Jeong, Kyung Mo Yoo, Young Seo Park, and Jang Joo Kim. Low roll-off of efficiency at high current density in phosphorescent organic light emitting diodes. *Applied Physics Letters*, **90**, 223508 (2007). doi:10.1063/1.2745224.

[158] Jang Hyuk Kwon and Ramchandra Pode. High Efficiency Red Phosphorescent Organic Light-Emitting Diodes with Simple Structure. In *Organic Light Emitting Diode - Material, Process and Devices*, edited by Seung Hwan Ko, June, chapter 4. In Tech d.o.o (2011). ISBN 978-953-307-273-9. doi:10.5772/18521.

[159] Shizuo Tokito and Isao Tanaka. Phosphorescent organic light-emitting devices: Triplet energy management. *Electrochemistry*, **76**, 24 (2008). doi:10.5796/electrochemistry.76.24.

[160] Changhee Lee, Heume-Il Baek, Jeonghun Kwak, Joon Youp Kim, and Byung Doo Chin. Optimization of white OLEDs based on charge carrier conduction properties of phosphorescent emitting layers. *Organic Light Emitting Materials and Devices XII*, **7051**, 70510M (2008). doi:10.1117/12.800786.

[161] Oleksandr V. Mikhnenko, Paul W. M. Blom, and Thuc-Quyen Nguyen. Exciton diffusion in organic semiconductors. *Energy Environ. Sci.*, **8**, 1867 (2015). doi:10.1039/C5EE00925A.

[162] Kazuo Udagawa, Hisahiro Sasabe, Fumiaki Igarashi, and Junji Kido. Simultaneous Realization of High EQE of 30%, Low Drive Voltage, and Low Efficiency Roll-Off at High Brightness in Blue Phosphorescent OLEDs. *Advanced Optical Materials*, **4**, 86 (2016). doi:10.1002/adom.201500462.

[163] Chaoyu Xiang, Xiangyu Fu, Wei Wei, Rui Liu, Yong Zhang, Viktor Balema, Bryce Nelson, and Franky So. Efficiency Roll-Off in Blue Emitting Phosphorescent Organic Light Emitting Diodes with Carbazole Host Materials. *Advanced Functional Materials*, **26**, 1463 (2016). doi:10.1002/adfm.201504357.

[164] Klemens Brunner, Addy Van Dijken, Herbert Börner, Jolanda J A M Bastiaansen, Nicole M M Kiggen, and Bea M W Langeveld. Carbazole Compounds as Host Materials for Triplet Emitters in Organic Light-Emitting Diodes: Tuning the HOMO Level without Influencing the Triplet Energy in Small Molecules. *Journal of the American Chemical Society*, **126**, 6035 (2004). doi:10.1021/ja049883a.

[165] Naresh B. Kotadiya, Paul W.M. Blom, and Gert Jan A.H. Wetzelaer. Efficient and stable single-layer organic light-emitting diodes based on thermally activated delayed fluorescence. *Nature Photonics*, **13**, 765 (2019). doi:10.1038/s41566-019-0488-1.

[166] Ping I. Shih, Chen Han Chien, Chu Ying Chuang, Ching Fong Shu, Cheng Han Yang, Jian Hong Chen, and Yun Chi. Novel host material for highly efficient

blue phosphorescent OLEDs. *Journal of Materials Chemistry*, **17**, 1692 (2007). doi:10.1039/b616043c.

[167] Xiaofan Ren, Jian Li, Russell J. Holmes, Peter I. Djurovich, Stephen R. Forrest, and Mark E. Thompson. Ultrahigh energy gap hosts in deep blue organic electrophosphorescent devices. *Chemistry of Materials*, **16**, 4743 (2004). doi:10.1021/cm049402m.

[168] Tianyu Zhu and Troy Van Voorhis. Charge Recombination in Phosphorescent Organic Light-Emitting Diode Host-Guest Systems through QM/MM Simulations. *Journal of Physical Chemistry C*, **120**, 19987 (2016). doi:10.1021/acs.jpcc.6b05559.

[169] Yuichiro Kawamura, Hidetoshi Yamamoto, Kenichi Goushi, Hiroyuki Sasabe, Chihaya Adachi, and Hiroki Yoshizaki. Ultraviolet amplified spontaneous emission from thin films of 4,4'-bis(9-carbazolyl)-2,2'-biphenyl and the derivatives. *Applied Physics Letters*, **84**, 2724 (2004). doi:10.1063/1.1695091.

[170] Yuichiro Kawamura, Hiroyuki Sasabe, and Chihaya Adachi. Simple accurate system for measuring absolute photoluminescence quantum efficiency in organic solid-state thin films. *Japanese Journal of Applied Physics, Part 1: Regular Papers and Short Notes and Review Papers*, **43**, 7729 (2004). doi:10.1143/JJAP.43.7729.

[171] Taiju Tsuboi and Nadeer Aljaroudi. Energy transfer between Ir(ppy)3 molecules in neat film and concentration quenching of phosphorescence. *Optical Materials*, **30**, 1375 (2008). doi:10.1016/j.optmat.2007.07.006.

[172] Takashi Kobayashi, Noritaka Ide, Noriyuki Matsusue, and Hiroyoshi Naito. Temperature dependence of photoluminescence lifetime and quantum efficiency in neat fac-Ir(ppy)3 thin films. *Japanese Journal of Applied Physics, Part 1: Regular Papers and Short Notes and Review Papers*, **44**, 1966 (2005). doi:10.1143/JJAP.44.1966.

[173] Yuichiro Kawamura, Jason Brooks, Julie J. Brown, Hiroyuki Sasabe, and Chihaya Adachi. Intermolecular interaction and a concentration-Quenching mechanism of phosphorescent Ir(III) complexes in a solid film. *Physical Review Letters*, **96**, 017404 (2006). doi:10.1103/PhysRevLett.96.017404.

[174] L. Zhang, H. van Eersel, P. A. Bobbert, and R. Coehoorn. Clarifying the mechanism of triplet-triplet annihilation in phosphorescent organic host-guest systems: A combined experimental and simulation study. *Chemical Physics Letters*, **652**, 142 (2016). doi:10.1016/j.cplett.2016.04.043.

[175] Vygintas Jankus, Chris Winscom, and Andrew P. Monkman. The photophysics of singlet, triplet, and degradation trap states in 4,4- N, N' -dicarbazolyl- 1, 1' -biphenyl. *Journal of Chemical Physics*, **130**, 074501 (2009). doi:10.1063/1.3077163.

[176] Y. Q. Zhang, G. Y. Zhong, and X. A. Cao. Concentration quenching of electroluminescence in neat Ir (ppy)3 organic light-emitting diodes. *Journal of Applied Physics*, **108**, 083107 (2010). doi:10.1063/1.3504599.

[177] Yuichiro Kawamura, Kenichi Goushi, Jason Brooks, Julie J. Brown, Hiroyuki Sasabe, and Chihaya Adachi. 100% phosphorescence quantum efficiency of Ir (III) complexes in organic semiconductor films. *Applied Physics Letters*, **86**, 071104 (2005). doi:10.1063/1.1862777.

[178] Chihaya Adachi, Raymond C. Kwong, Peter Djurovich, Vadim Adamovich, Marc A. Baldo, Mark E. Thompson, and Stephen R. Forrest. Endothermic energy transfer: A mechanism for generating very efficient high-energy phosphorescent emission in organic materials. *Applied Physics Letters*, **79**, 2082 (2001). doi:10.1063/1.1400076.

[179] Arthur R. G. Smith, Paul L. Burn, and Ben J. Powell. Spin-orbit coupling in phosphorescent iridium(III) complexes. *ChemPhysChem*, **12**, 2429 (2011). doi:10.1002/cphc.201100397.

[180] J. C. Ribierre, A. Ruseckas, I. D.W. Samuel, S. V. Staton, and P. L. Burn. Temperature dependence of the triplet diffusion and quenching rates in films of an Ir (ppy)3 -cored dendrimer. *Physical Review B - Condensed Matter and Materials Physics*, **77**, 085211 (2008). doi:10.1103/PhysRevB.77.085211.

[181] R. Richert and H. Bässler. Dispersive triplet excitation transport in organic glasses. *The Journal of Chemical Physics*, **84**, 3567 (1986). doi:10.1063/1.450243.

[182] Nathan Schmid, Andreas P. Eichenberger, Alexandra Choutko, Sereina Riniker, Moritz Winger, Alan E. Mark, and Wilfred F. van Gunsteren. Definition and testing of the GROMOS force-field versions 54A7 and 54B7. *European Biophysics Journal*, **40**, 843 (2011). doi:10.1007/s00249-011-0700-9.

[183] Alpeshkumar K. Malde, Le Zuo, Matthew Breeze, Martin Stroet, David Poger, Pramod C. Nair, Chris Oostenbrink, and Alan E. Mark. An Automated force field Topology Builder (ATB) and repository: Version 1.0. *Journal of Chemical Theory and Computation*, **7**, 4026 (2011). doi:10.1021/ct200196m.

[184] H. J. C. Berendsen, J. P. M. Postma, W. F. van Gunsteren, A. Dinola, and J. R. Haak. Molecular dynamics with coupling to an external bath. *The Journal of Chemical Physics*, **81**, 3684 (1984). doi:10.1063/1.448118.

[185] Ilario G. Tironi, René Sperb, Paul E. Smith, and Wilfred F. van Gunsteren. A generalized reaction field method for molecular dynamics simulations. *The Journal of Chemical Physics*, **102**, 5451 (1995). doi:10.1063/1.469273.

[186] Berk Hess, Henk Bekker, Herman J. C. Berendsen, and Johannes G. E. M. Fraaije. LINCS: A Linear Constraint Solver for molecular simulations.

Journal of Computational Chemistry, **18**, 1463 (1997). doi:10.1002/(SICI)1096-987X(199709)18:12<1463::AID-JCC4>3.0.CO;2-H.

[187] Kyoung Soo Yook and Jun Yeob Lee. Small molecule host materials for solution processed phosphorescent organic light-emitting diodes. *Advanced Materials*, **26**, 4218 (2014). doi:10.1002/adma.201306266.

[188] Min Cai, Teng Xiao, Emily Hellerich, Ying Chen, Ruth Shinar, and Joseph Shinar. High-efficiency solution-processed small molecule electrophosphorescent organic light-emitting diodes. *Advanced Materials*, **23**, 3590 (2011). doi:10.1002/adma.201101154.

[189] Tae Hee Han, Mi Ri Choi, Chan Woo Jeon, Yun Hi Kim, Soon Ki Kwon, and Tae Woo Lee. Ultrahigh-efficiency solution-processed simplified small-molecule organic light-emitting diodes using universal host materials. *Science Advances*, **2** (2016). doi:10.1126/sciadv.1601428.

[190] Guilin Mao, Zhaoxin Wu, Qiang He, Bo Jiao, Guojin Xu, Xun Hou, Zhijian Chen, and Qihuang Gong. Considerable improvement in the stability of solution processed small molecule OLED by annealing. *Applied Surface Science*, **257**, 7394 (2011). doi:10.1016/j.apsusc.2011.02.046.

[191] Tae Woo Lee, Taeyong Noh, Hee Won Shin, Ohyun Kwon, Jong Jin Park, Byoung Ki Choi, Myeong Suk Kim, Dong Woo Shin, and Yong Rok Kim. Characteristics of solution-processed small-molecule organic films and light-emitting diodes compared with their vacuum-deposited counterparts. *Advanced Functional Materials*, **19**, 1625 (2009). doi:10.1002/adfm.200801045.

[192] Yong Joo Cho, Scott Taylor, and Hany Aziz. Increased Electromer Formation and Charge Trapping in Solution-Processed versus Vacuum-Deposited Small Molecule Host Materials of Organic Light-Emitting Devices. *ACS Applied Materials and Interfaces*, **9**, 40564 (2017). doi:10.1021/acsami.7b15190.

[193] Yong Joo Cho and Hany Aziz. Root Causes of the Limited Electroluminescence Stability of Organic Light-Emitting Devices Made by Solution-Coating. *ACS Applied Materials and Interfaces*, **10**, 18113 (2018). doi:10.1021/acsami.8b00926.

[194] Hyeonghwa Yu, Yingjie Zhang, Yong Joo Cho, and Hany Aziz. Exciton-Induced Degradation of Carbazole-Based Host Materials and Its Role in the Electroluminescence Spectral Changes in Phosphorescent Organic Light Emitting Devices with Electrical Aging. *ACS Applied Materials and Interfaces*, **9**, 14145 (2017). doi:10.1021/acsami.7b01432.

[195] William Humphrey, Andrew Dalke, and Klaus Schulten. VMD: Visual Molecular Dynamics. *Journal of molecular graphics*, **14**, 33 (1996).

[196] Lei Zhang, Shou Cheng Dong, Chun Hong Gao, Xiao Bo Shi, Zhao Kui Wang, and Liang Sheng Liao. Origin of improved stability in green phosphorescent

organic light-emitting diodes based on a dibenzofuran/spirobifluorene hybrid host. *Applied Physics A: Materials Science and Processing*, **118**, 381 (2014). doi:10.1007/s00339-014-8746-z.

[197] Ting Xu, Jun Gui Zhou, Chen Chao Huang, Lei Zhang, Man Keung Fung, Imran Murtaza, Hong Meng, and Liang Sheng Liao. Highly Simplified Tandem Organic Light-Emitting Devices Incorporating a Green Phosphorescence Ultrathin Emitter within a Novel Interface Exciplex for High Efficiency. *ACS Applied Materials and Interfaces*, **9**, 10955 (2017). doi:10.1021/acsami.6b16094.

[198] M. A. Baldo, C. Adachi, and S. R. Forrest. Transient analysis of organic electrophosphorescence. II. Transient analysis of triplet-triplet annihilation. *Physical Review B - Condensed Matter and Materials Physics*, **62**, 10967 (2000). doi:10.1103/PhysRevB.62.10967.

[199] Toshimitsu Tsuzuki and Shizuo Tokito. Highly efficient, low-voltage phosphorescent organic light-emitting diodes using an iridium complex as the host material. *Advanced Materials*, **19**, 276 (2007). doi:10.1002/adma.200600845.

[200] Adrian Heil, Kathleen Gollnisch, Martin Kleinschmidt, and Christel M. Marian. On the photophysics of four heteroleptic iridium(III) phenylpyridyl complexes investigated by relativistic multi-configuration methods. *Molecular Physics*, **114**, 407 (2016). doi:10.1080/00268976.2015.1076902.

[201] L. Zhang, H. van Eersel, P. A. Bobbert, and R. Coehoorn. Analysis of the phosphorescent dye concentration dependence of triplet-triplet annihilation in organic host-guest systems. *Chemical Physics Letters*, **662**, 221 (2016). doi:10.1016/j.cplett.2016.07.048.

[202] Arnout Ligthart, Xander de Vries, Le Zhang, Mike C.W.M. Pols, Peter A. Bobbert, Harm van Eersel, and Reinder Coehoorn. Effect of Triplet Confinement on Triplet–Triplet Annihilation in Organic Phosphorescent Host–Guest Systems. *Advanced Functional Materials*, **28**, 1 (2018). doi:10.1002/adfm.201804618.

[203] S. Lamansky, P. Djurovich, D. Murphy, F. Abdel-Razzaq, R. Kwong, I. Tsyba, M. Bortz, B. Mui, R. Bau, and M. E. Thompson. Synthesis and characterization of phosphorescent cyclometalated iridium complexes. *Inorganic Chemistry*, **40**, 1704 (2001). doi:10.1021/ic0008969.

[204] Sebastian Reineke, Thomas C. Rosenow, Björn Lüssem, and Karl Leo. Improved high-brightness efficiency of phosphorescent organic LEDs comprising emitter molecules with small permanent dipole moments. *Advanced materials (Deerfield Beach, Fla.)*, **22**, 3189 (2010). doi:10.1002/adma.201000529.

[205] Pascal Friederich, Artem Fediai, Jing Li, Anirban Mondal, Naresh Kotadiya, Gabriele D'Avino, Franz Symalla, Gert Jan Wetzelaer, Denis Andrienko, David Beljonne, Paul Blom, Jean Luc Brédas, and Wolfgang Wenzel. The influence of

impurities on the charge carrier mobility of small molecule organic semiconductors. *arXiv* (2019).

[206] Reinder Coehoorn, Harm van Eersel, Peter A. Bobbert, and René A J Janssen. Kinetic Monte Carlo Study of the Sensitivity of OLED Efficiency and Lifetime to Materials Parameters. *Advanced Functional Materials*, **25**, 2024 (2015). doi:10.1002/adfm.201402532.

[207] Laura Scalfi, David Limmer, Alessandro Coretti, Sara Bonella, Paul A. Madden, Mathieu Salanne, and Benjamin Rotenberg. Charge fluctuations from molecular simulations in the constant-potential ensemble. *Phys. Chem. Chem. Phys.*, 10480–10489 (2020). doi:10.1039/c9cp06285h.